

ABSTRACT

Title of dissertation: THE COSMIC NEAR-INFRARED BACKGROUND:
FROM THE DARK AGES TO THE PRESENT

Kari Helgason, Doctor of Philosophy, 2014

Dissertation directed by: Professor Massimo Ricotti
University of Maryland
Department of Astronomy

Dr. Alexander Kashlinsky
NASA Goddard Space Flight Center
Observational Cosmology Laboratory, Code 665

The Cosmic Infrared Background (CIB) is made up of the collective light from galaxies and quasars built-up over the entire cosmic history. It plays an important role in characterizing the evolution of galaxies and contains information on other sources inaccessible to direct detection. In this dissertation, I seek to understand current CIB measurements in terms of all sources emitting since the era of the first stars.

First, I model the CIB arising from known galaxy populations using 233 measured UV, optical and NIR luminosity functions from a variety of surveys spanning a wide range of redshifts. Our empirical approach, in conjunction with a halo model describing the clustering of galaxies, allows us to compute the fluctuations of the unresolved CIB and compare to current measurements. I find that fluctuations from known galaxy populations are unable to account for the large scale CIB clustering

signal seen by current space observatories, and this discrepancy continues to diverge out to larger angular scales. This suggests that known galaxy populations are not responsible for the bulk of the fluctuation signal seen in the measurements and favors a new population of faint and highly clustered sources.

I also empirically reconstruct the evolving extragalactic background light from galaxies and derive the associated opacity of the universe to high energy photons out to $z \sim 4$. Covering the whole range from UV to mid-IR ($0.15\text{-}25\mu\text{m}$), I provide for the first time a robust empirical calculation of the $\gamma\gamma$ optical depth out to several TeV. In the absence of significant contributions to the cosmic diffuse background from unknown populations, such as the putative first stars and black holes, the universe appears to be largely transparent to γ -rays at all *Fermi*/LAT energies out to $z \sim 2$ whereas becoming opaque to TeV photons already at $z \sim 0.2$.

In addition, I study contributions from extragalactic populations to a recently discovered cross-correlation signal of the CIB fluctuations with the Cosmic X-ray Background (CXB). I model the X-ray emission from AGN, normal galaxies and hot gas residing in virialized structures, calculating their CXB contribution and spatial coherence with all infrared emitting counterparts. At small angular scales the coherence between the CIB and the CXB can be explained by galaxies and AGN. However, at large angular scales I find the net contribution from these populations only to account for a fraction of the measured CIB \times CXB signal. The discrepancy suggests that the signal originates from the same unknown source population producing the CIB clustering signal out to ~ 1 deg.

THE COSMIC NEAR-INFRARED BACKGROUND: FROM THE
DARK AGES TO THE PRESENT

by

Kari Helgason

Dissertation submitted to the Faculty of the Graduate School of the
University of Maryland, College Park in partial fulfillment
of the requirements for the degree of
Doctor of Philosophy
2014

Advisory Committee:
Professor Massimo Ricotti, Chair/Advisor
Doctor Alexander Kashlinsky, Advisor
Professor Sylvain Veilleux
Professor Richard Mushotzky
Professor Ted Jacobson

© Copyright by
Kari Helgason
2014

*“Mér er eintal sálarinnar óþrotlegur auður. Dögg jarðarinnar, þytur vindanna,
geislar hnúgandi kvöldsólar, stjörnuþjartur næturhiminn, mánans milda bros, lygn
vötn, fornar húsatættur, gamlir sorphaugar, blámi fjarlæggra fjalla, skuggar dimmra
dala, ljósbrot í stremdu gleri, þögn hjarta míns – í þessu finn ég lyfting hins eilífa
lífs.”*

– Þórbergur Þórðarson

Preface

The material presented in this thesis is has been published in peer-reviewed journals and presented at professional conferences. The content of Chapter 2 was previously published in the *Astrophysical Journal* as “*Reconstructing the Near-IR Background Fluctuations from known Galaxy Populations using Multiband Measurements of Luminosity Functions*” (Helgason et al. 2012) and was followed by a proceedings article “*Can the Near-IR Fluctuations Arise from Known Galaxy Populations?* “ in *AIP Conference Series* from “The First Stars IV meeting” in Kyoto, Japan (Helgason et al. 2012b). In addition, this work was presented at two meetings; “Near Infrared Background and the Epoch of Reionization” in Austin, Texas; and the “Enrico Fermi Summer School: New Horizons in Observational Cosmology” in Italy. Chapter 3 was published in the *Astrophysical Journal Letters* as “*Reconstructing the γ -ray Photon Optical Depth of the Universe to $z\sim 4$ from Multiwavelength Galaxy Survey Data*” (Helgason & Kashlinsky 2012) and presented as an invited talk at the Harvard-Smithsonian CfA. Chapter 4 is based on a paper published in the *Astrophysical Journal* as “*The Contribution of $z<6$ Sources to the Spatial Coherence in the Unresolved Cosmic near-Infrared and X-ray Backgrounds*” (Helgason et al. 2014). This work was also presented as an invited talk at Harvard-Smithsonian, MIT, Princeton University and the Max Planck Institute for Astrophysics. The collective work was appearing in Chapters 2–4 was also presented at the 2014 Winter AAS meeting in Washington D.C. as a part of an oral dissertation presentation.

To my grandmother Amma Lóa

Acknowledgments

I would like to express my gratitude to those around me who have made this dissertation possible. First and foremost, my two advisors Sasha Kashlinsky and Massimo Ricotti for all their keen scientific insights that I hope to acquire myself someday. I am eternally grateful for the opportunity they gave me to conduct research in modern cosmology. I also want to thank them both for investing so much of their time in guiding me, which over the course of five years, has shaped me into an able scientist. I also thank the members of this committee for their service and dutiful reading of this long document.

I am indebted to astronomers in my home country, Vilhelm S. Sigmundsson, whose textbook and lectures sparked my interest in astronomy, and Einar H. Guðmundsson for all the fatherly advise he gave me as an undergraduate. Also, to my colleagues at *Sjörnufraeðivefurinn*, Sævar and Sverrir, who fueled my enthusiasm for astronomy and helped me better understand the importance of connecting our science with the general public. And to all the wonderful staff at the University of Maryland for keeping the all the paperwork tidy. Special thanks to Shaye the muffin-top master and Mary and her fluffy sidekick, for their close friendship.

I want to acknowledge financial assistance from a number of funding sources. The *Fulbright Scholarship Program*, the *Leifur Eiriksson Foundation*, the *American-Scandinavian Society* and the UMD Graduate School. Without their support, this project would have been abandoned at early stages. Special thanks to the *NASA Earth and Space Sciences Program* which kept me funded for the last three years.

All the work presented in this dissertation was supported by NASA Headquarters under the NESSF Program Grant – NNX11AO05H.

Last but not least, I would like to thank my loving wife, Þórhildur, for always standing by me at my highest and lowest points. Together we have shared our burdens and kept each other going through two challenging doctoral programs. We could not have done this without our families, especially my mother Sirrý, whose unconditional support has helped us cope with years of living a long way from home.

Contents

1	Introduction	1
1.1	Theoretical Background	2
1.1.1	Cosmological Paradigm	2
1.1.2	Isotropic Background Flux	8
1.1.3	Background Anisotropies	11
1.2	CIB Measurements	14
1.3	γ -ray Opacity	18
1.4	CIB Fluctuations	19
2	CIB from Known Galaxy Population: An Empirical Model	26
2.1	Overview	26
2.2	Measurements of the Galaxy Luminosity Function	27
2.3	Populating the Lightcone with known Galaxy Populations	33
2.3.1	The Faint-End Regime	43
2.4	Number Counts and Background Light from LF Data	46
2.5	CIB Fluctuations from Unresolved Galaxies	50
2.5.1	Shot Noise	54
2.5.2	Galaxy Clustering	56
2.5.3	Comparing with Semi-Analytic Models	60
2.5.4	Results	61
2.6	Discussion	67
3	The γ -ray Opacity of the Universe	69
3.1	Overview	69
3.2	Reconstructing the Evolving EBL from Data	70
3.3	The Photon-photon Optical Depth	76
3.4	Application to High Energy Observations	77
3.5	Discussion	82
4	X-ray Emission from the CIB Sources: The Origin of the CIB \times CXB Signal	84
4.1	Overview	84
4.2	The Measured CIB \times CXB Coherence	86
4.3	Sources of the CIB	89
4.3.1	Galaxies	89
4.3.2	AGN	90
4.3.3	Diffuse emission, intrahalo light	93

4.4	Sources of the CXB	95
4.4.1	Normal X-ray Galaxies	95
4.4.1.1	Late-types	97
4.4.1.2	Early-types	101
4.4.1.3	Hot gas	102
4.4.1.4	The unresolved CXB from galaxies	103
4.4.2	X-ray AGN	107
4.4.3	Diffuse Hot Gas and WHIM	111
4.5	The Angular Auto/Cross Power Spectrum of Multiple Populations	112
4.5.1	Halo Model	115
4.5.2	Halo Occupation, Bias and Mass Selection	117
4.5.3	Comparing fluctuation models with N-body simulations	122
4.6	Results	123
4.6.1	CIB Fluctuations	123
4.6.2	CXB Fluctuations	124
4.6.3	CIB×CXB Fluctuations	125
4.7	Discussion	131
5	Summary and Conclusions	134
5.1	Future Outlook	135
A	Appendix	139
A.1	LF Binning and Interpolations	139
A.2	Consistency notes	140
A.2.0.1	K-correction	140
A.2.0.2	Photometric Systems	142
A.2.0.3	Luminosity Function Estimators	143

Chapter 1: Introduction

Observational cosmology has taken significant strides to fulfill its ultimate goal: to reconstruct the entire history of the universe. Whereas the simple conditions of the early universe are manifested in the cosmic microwave background (CMB), powerful telescopes reveal a seemingly mature population of galaxies already existing when the universe was merely ~ 500 million years old. At some earlier stage, gas had to condense into galaxies, stars and black holes, transforming the hitherto dark featureless universe into one of an increasingly complex state. These objects were able to convert mass into energy according Einstein's famous equation $E = mc^2$ and thus began filling the universe with electromagnetic radiation. This radiation, accumulated over the entire cosmic history, gives rise to the cosmic infrared background (CIB) that can be observed today. The CIB therefore probes galaxy evolution from the early universe to the present epoch and contains information about objects inaccessible to current telescopes.

Shortly after the discovery of the CMB, the fundamentals of the CIB were laid out by Partridge & Peebles 1967 who predicted¹ its level (1). It was not until much later that CIB investigations became an empirical science as measurements

¹Despite a number of assumptions, their calculation came remarkably close to the actual levels.

needed to be conducted from space in the absence of the Earth’s atmosphere. Even from space however, foregrounds from the Solar System and the Galaxy present a great challenge for uncovering the CIB. The first instrument entirely devoted to the CIB was *The Diffuse Infrared Background Experiment* (DIRBE) on board the COBE satellite, launched in 1989. It provided the first reliable measurements and marked the beginning of the observational CIB era. Since DIRBE, various observatories have provided a wealth data that has allowed us to probe the CIB using multiple techniques: direct flux measurements, galaxy counts, angular fluctuations and interactions with high energy γ -rays. In spite of these efforts, many questions remain unanswered. For example, we still do not know the absolute flux of the CIB and how much originates in the early universe; there is a long-standing tension between the CIB flux and upper limits inferred from extragalactic γ -ray studies (see Chapter 3); we see a large scale clustering signal in the CIB fluctuations that is inconsistent with any known types of sources (see Chapter 2). This dissertation aims to shed light on these issues through a better understanding of the fluctuations in the unresolved CIB and through complementary insights from high energy astrophysics.

1.1 Theoretical Background

1.1.1 Cosmological Paradigm

In the late nineteen twenties, George Lemaître discovered that the universe is expanding. He noticed that galaxies are rushing away from us with velocities (v) that are proportional to their distance (d), a relation that has historically been accredited

to Edwin Hubble and called *Hubble's law* (2; 3; 4)

$$v = H_0 d \tag{1.1}$$

where H_0 is the *Hubble constant*, measured today to be approximately $\simeq 70 \text{ km s}^{-2} \text{ Mpc}^{-1}$. Had the universe always expanded at this rate, then all matter should have been concentrated at the same point $H_0^{-1} = 1.4 \times 10^{10}$ years ago suggesting that the universe may have had a beginning. The discovery ultimately led to the Big Bang theory, a tremendously successful theory describing the beginning and evolution of the universe out of a very dense state.

Einstein's theory of general relativity provides a framework for describing the universe as a whole. In what is called *the cosmological principle*, the universe is isotropic and homogeneous on largest scales. The *metric* for homogeneous and isotropically distributed matter is the Friedmann-Lemaître-Robertson-Walker metric (FLRW), which can be written

$$ds^2 = -dt^2 + a^2(t) \left[\frac{dr^2}{1 - kr^2} + r^2(d\theta^2 + \sin^2\theta d\phi^2) \right] \tag{1.2}$$

where $a(t)$ is the *scale factor* of the universe representing the expansion with time, t , and (r, θ, ϕ) are spherical coordinates. The constant k describes the geometry of the universe, taking on a value 1 for a closed universe, 0 for a flat universe, and -1 for an open universe. Points at rest remain at fixed coordinates (r, θ, ϕ) but the physical distance between them increases with time, governed by $a(t)$. As photons

travel through an expanding universe, they are stretched such that their observed wavelengths become larger than their emitted wavelengths, shifting them towards the red part of the spectrum. The stretching factor can therefore be defined as the *redshift* (z)

$$1 + z = \frac{\lambda_{\text{obs}}}{\lambda_{\text{em}}} = \frac{1}{a} \quad (1.3)$$

where we have set the scale factor at the present day to $a_0 = 1$. For low redshifts, the standard Doppler formula applies i.e. $z \approx v/c$ and the recession velocities of galaxies can be derived from emission/absorption lines in their spectra. The redshift (and the scale factor) is therefore a direct measure of the expansion of space since the photons were emitted.

For the FLRW metric (Equation 1.2), the Einstein equations of general relativity yield the Friedmann equation (e.g. ref. 5)

$$H^2(t) = \left(\frac{\dot{a}}{a}\right)^2 = \frac{8\pi G}{3}\rho - \frac{k}{c^2 a^2} \quad (1.4)$$

relating the expansion of the universe, $H(t)$, to its energy content, ρ . The energy (and matter) density of the universe has three types of components: matter, radiation, and vacuum energy (or a cosmological constant), such that the net density is $\rho = \rho_m + \rho_r + \rho_\Lambda$. For the equation of state of each component, $p = p(\rho)$, energy conservation shows how they evolve with time

$$\Omega = \Omega_m a^{-3} + \Omega_r a^{-4} + \Omega_\Lambda \quad (1.5)$$

where we have defined the ratio of the total density to the critical density $\Omega = \rho/\rho_{\text{crit}}$ with $\rho_{\text{crit}} = 3H^2/8\pi G$. The Friedmann equation combined with Equation 1.3 then gives

$$H(z) = H_0 [(1+z)^3\Omega_m + \Omega_\Lambda + (1+z)^4\Omega_r + (1+z)^2\Omega_k]^{1/2} \quad (1.6)$$

where $\Omega_k \equiv -k/H_0^2$. Note, that Ω_m contains both dark matter and ordinary matter (baryons). In the standard hot Big Bang model, the universe is initially dominated by radiation and transitions to matter domination at $z \sim 10^4$. The standard Λ CDM cosmology refers to the state of the current universe which is dominated by cold dark matter and dark energy $\Omega_{\text{CDM}} + \Omega_\Lambda \simeq 0.95$. For all epochs of interest in this dissertation, radiation is negligible and curvature is measured to be close to zero.

For a given set of cosmological parameters the redshift can be used as a universal timekeeper. The exact relation between redshift and cosmic time follows from Equation 1.3 and 1.4

$$\frac{dt}{dz} = -\frac{a^2}{\dot{a}} = -\frac{1}{H_0(1+z)} \frac{1}{\sqrt{(1+z)^3\Omega_m + \Omega_\Lambda + (1+z)^4\Omega_r + (1+z)^2\Omega_k}} \quad (1.7)$$

The latest CMB measurements provided by the *Planck* satellite find the best-fit cosmological parameters $(h, \Omega_m, \Omega_\Lambda) = (0.678, 0.308, 0.692)$ and $(\Omega_r, \Omega_k) \simeq 0$.

The levels and structure of the CIB depend on the history of energy produced by the baryonic component of the universe. The baryonic evolution is governed by the gravitational growth of density inhomogeneities, that both depends on the nature of dark matter and the cosmological parameters. Observations of the CMB

reveal a very uniform early universe with density fluctuations of roughly one part in 10^5 . Gravitational instabilities cause these small fluctuations to grow with time, ultimately leading to the clumpy universe of galaxies and clusters we see today. Imposing perturbations to the uniform expansion, $\delta \equiv \delta\rho(\vec{x})/\bar{\rho}$, one can show that small fluctuations $\delta \ll 1$ grow according to the linear differential equation (e.g. refs. 6; 7)

$$\ddot{\delta} + 2\frac{\dot{a}}{a}\dot{\delta} - 4\pi G\bar{\rho}_m\delta = 0 \quad (1.8)$$

where $\bar{\rho}_m$ is the average matter density. In a flat, matter dominated universe, fluctuations simply grow as $\delta \propto a(t)$. The density field $\delta(\vec{x})$ is often described in terms of the power spectrum $P(k) = \langle |\delta_k|^2 \rangle$ where δ_k is the Fourier transform of $\delta(\vec{x})$ and k is the wavenumber. Figure 1.1 shows the evolving three dimensional power spectrum as a function of wavenumber. In the most general models, inflation produces a power spectrum $P(k) \propto k^n$ with $n \simeq 1$. During the radiation dominated era, fluctuations do not grow inside the horizon c/H^{-1} and the power spectrum turns over at the horizon scale at matter-radiation equality, asymptoting to $P(k) \propto k^{-3}$ towards small physical scales. On the smallest scales, the power spectrum changes as the growth of perturbations becomes non-linear.

The power spectrum is normalized by the variance observed in the density field over a sphere of $8 h^{-1}\text{Mpc}$, measured today to be $\sigma_8 = 0.86$. The variance over a sphere of radius $R = (3M/4\pi\bar{\rho})^{1/3}$ is

$$\sigma^2(M) = \frac{1}{2\pi^2} \int P(k) \left(\frac{3j_1(kR)}{kR} \right)^2 k^2 dk. \quad (1.9)$$

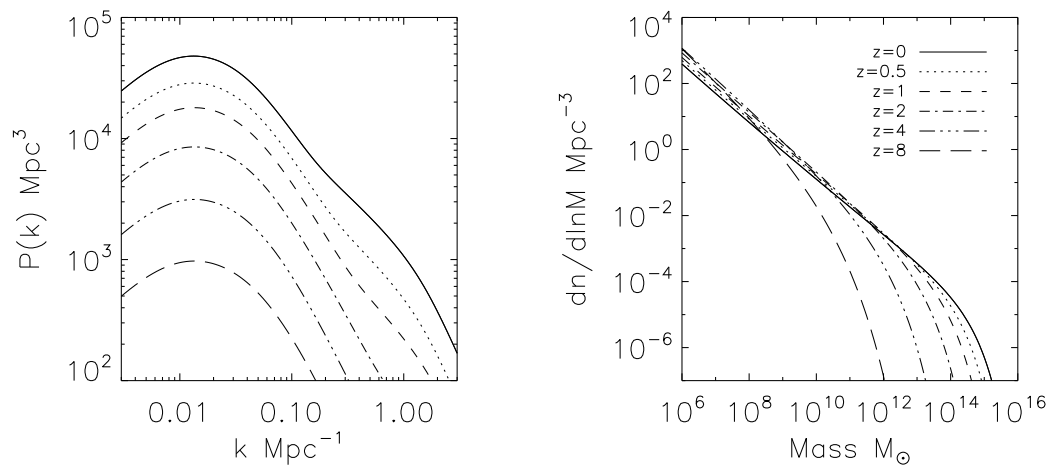


Figure 1.1 *Left:* The matter power spectrum as a function of comoving wavenumber at several redshifts. The calculation assumes the BBKS approximation i.e. ref. (8). At the largest scales $P(k) \propto k^n$ with $n = 0.96$ with a turnover at the horizon scale at matter-radiation equality asymptoting to $P(k) \propto k^{-3}$. Towards the smallest scales, the shape changes as fluctuations become non-linear (9). *Right:* The Press-Schechter mass function of dark matter halos (see Equation 1.10) that have collapsed at several redshifts (10).

where $j_1(kR)$ is the first order Bessel function. Adopting a spherical model for the evolution and collapse of density fluctuations would give that any mass that, in linear approximation, reached the density contrast of $\delta_{\text{col}} = 1.68$ could collapse. Therefore $\eta = \delta_{\text{col}}/\sigma_M$ gives the number of standard deviations a given object had to be in order to collapse at the given z . CDM and most inflation inspired models predict that the primordial density was Gaussian, so the fraction of the total mass density in collapsed halos at redshift z is given by $F(> M) = \text{erfc}(\eta/\sqrt{2})$. Differentiating the fraction of dark matter in halos above M yields the mass distribution of dark matter halos. Letting dn be the comoving number density of halos of mass between M and $M + dM$, we have (10)

$$\frac{dn}{dM} = -\sqrt{\frac{2}{\pi}} \bar{\rho}_m \eta \frac{d \ln \sigma_M}{d \ln M} \exp[-\eta^2/2]. \quad (1.10)$$

where η and σ_M are functions of mass as well as redshift.

1.1.2 Isotropic Background Flux

The energy of all light rays passing through an area dA in time dt and frequency range $d\nu$ whose direction is within a solid angle $d\Omega$ is the specific intensity (11)

$$I_\nu = \frac{dE}{dA dt d\nu d\Omega}. \quad (1.11)$$

The radiative energy density describes the energy of light rays in a cylinder of volume $dV = c dt dA$ in the frequency range $d\nu$, $u_\nu = dE/(dV d\nu d\Omega)$. The mean

(angle averaged) intensity is related to the radiative energy density

$$I_\nu = \frac{c}{4\pi} u_\nu. \quad (1.12)$$

As radiating sources build up background radiation over time, it is convenient to relate I_ν to the evolving volume emissivity $j_\nu = dE/(dV dt d\nu d\Omega)$ (sometimes called ϵ_ν), integrated over cosmic time

$$I_\nu = \frac{c}{4\pi} \int j_\nu dt \quad (1.13)$$

Because the expansion of the universe, j_ν is evaluated at the rest frame frequency, ν' , which is related to the observed frequency $\nu' = \nu(1+z)$. We express the surface brightness of the sky (which we simply call *flux*) as

$$\nu I_\nu = \frac{c}{4\pi} \int \nu' j_{\nu'}(z) \frac{dt}{dz} \frac{dz}{1+z}. \quad (1.14)$$

For extragalactic background light in the ultraviolet, optical and near-infrared regimes, the flux is most commonly expressed in units of $\text{nW m}^{-2}\text{sr}^{-1}$. Conversions to other units appearing in this dissertation are

$$1 \frac{\text{nW}}{\text{m}^2\text{sr}} = 10^{-6} \frac{\text{erg}}{\text{s cm}^2\text{sr}} = \frac{3000 \text{ MJy}}{\lambda(\mu\text{m}) \text{ sr}}. \quad (1.15)$$

Because the energy density of the universe is composed of discrete sources, a sometimes more useful expression of Equation 1.14 is one expressing the flux in

terms of the *luminosity function* $\Phi(L) = dN/dLdV$, a quantity which is commonly obtained in galaxy surveys. Defining $F \equiv \nu I_\nu$ and $L = \nu L_\nu$, the background flux is

$$F = \int \frac{\int L\Phi(L)dL}{4\pi d_L^2} k(z)dV = \frac{c}{4\pi} \int \int L\Phi(L, z)dL \frac{dt}{dz} k(z) \frac{dz}{1+z} \quad (1.16)$$

where $k(z)$ corrects rest-frame luminosity to the observed frame (k-correction) and the volume element in a FRLW universe is $dV = cd_L^2 a(t)dt$. This is equivalent to Equation 1.14 with the identification $\nu j_\nu = \int L\Phi(L)dL$. The flux distribution of discrete sources can be obtained by projecting the evolving luminosity function onto the sky and setting $dS = dL/4\pi d_L^2$. This gives the *number counts*, another diagnostic obtained in surveys

$$\frac{dn}{dS} = \int \Phi(L, z) \frac{4\pi d_L^2}{k(z)} \frac{dV}{dz} dz \quad (1.17)$$

in number per solid angle. The number counts can be integrated to directly obtain the background flux from discrete sources

$$F = \int_{S_{\text{lim}}}^{\infty} S \frac{dn}{dS} dS \quad (1.18)$$

where S_{lim} is the lowest flux source detected in the survey. This is referred to as the *resolved background* whereas integrating over undetected sources, from zero to S_{lim} , gives the *unresolved background*. Together they make up the *total background*. In optical surveys, magnitudes m are typically used rather than the physical flux, S .

Table 1.1 Conversions between the AB and Vega magnitude systems in near-IR bands

Band	λ (μm)	$(m_{\text{AB}} - m_{\text{Vega}})$
Y	1.02	0.63
J	1.25	0.94
H	1.6	1.38
K	2.2	1.90
L	3.6	2.79
M	4.5	3.26

Note. — Adopted from refs. (13) and (14). See also Chris Willmer’s page on the absolute magnitude of the sun: <http://mips.as.arizona.edu/~cnaw/sun.html>

Then Equation 1.18 simply becomes

$$F = \int_{-\infty}^{m_{\text{lim}}} S(m) \frac{dn}{dm} dm \quad (1.19)$$

where $S(m) = \nu \cdot 10^{-0.4(m-48.6)}$ $\text{erg s}^{-1}\text{cm}^{-2}$. Throughout this dissertation, we use the AB magnitude system which is directly related to the physical flux (12)

$$m_{\text{AB}} = -2.5 \log_{10} S_{\nu} - 48.6 \quad (1.20)$$

where S_{ν} is in $\text{erg s}^{-1}\text{cm}^{-2}\text{Hz}^{-1}$. Table 1.1 lists the adopted conversions between the AB and Vega magnitude systems (13; 14).

1.1.3 Background Anisotropies

Anisotropies in the CIB carry valuable information about the sources producing it. Anisotropies can be characterized in terms of *fluctuations* about the mean CIB level. At any coordinate position θ on the sky, the CIB surface brightness flux can

be written as

$$F(\theta) = \langle F \rangle + \delta F_\theta \quad (1.21)$$

where $\langle F \rangle$ is the mean isotropic flux and the fluctuation δF_θ is a function of angular coordinates. The two-dimensional Fourier transform of δF_θ is defined as $\delta_{\mathbf{q}} = \int \delta F_\theta \exp(-i\mathbf{q} \cdot \vec{\theta}) d^2\mathbf{q}$ where \mathbf{q} is the angular wavenumber vector in rad^{-1} . The fluctuation field can be analyzed via the angular power spectrum, $P(q) \equiv \langle |\delta_{\mathbf{q}}|^2 \rangle$ where the average is performed over all angles. The power spectrum can be efficiently calculated using the Fast Fourier Transform (FFT). One can also use the correlation function $w(\theta) = \langle \delta F(\mathbf{x}) \delta F(\mathbf{x} + \theta) \rangle$ which is simply the inverse Fourier transform of the power spectrum. The mean square fluctuation on angular scale $\theta = 2\pi/q$ can be conveniently approximated as (13)

$$\langle \delta F_\theta^2 \rangle \simeq \frac{q^2 P(q)}{2\pi}. \quad (1.22)$$

We will use this representation of the fluctuations throughout this dissertation.

The angular power spectrum from extragalactic populations can be decomposed into the *clustering* and *shot noise* of the underlying sources

$$P_{\text{tot}}(q) = P_{\text{cl}} + P_{\text{sn}}. \quad (1.23)$$

The clustering term describes the spatial correlation of the underlying sources and is related to their three dimensional power spectrum, $P(k, z)$, by projection onto

the sky via the Limber equation (15)

$$P_{\text{cl}}(q) = \int \frac{H(z)}{cd_c^2(z)} \left[\frac{dF}{dz} \right]^2 P(qd_c^{-1}, z) dz \quad (1.24)$$

where $d_c(z)$ is the comoving distance and $H(z)$ is defined in Eqn. 1.6. The quantity in the square brackets is the rate of flux production over the cosmic history. The shot noise is a scale independent white noise component arising from the fluctuation in the number of sources within the instrument beam (essentially counting noise). It only depends on the flux distribution of sources and can be expressed as

$$P_{\text{sn}} = \int_0^{S_{\text{lim}}} S^2 \frac{dn}{dS} dS \quad (1.25)$$

where S_{lim} is the minimum detected source brightness. Because galaxy clustering has power spectrum that increases towards large scales, the shot-noise component becomes progressively more important at smaller angular scales. In measurements with a finite beam, the intrinsic power spectrum is convolved with the window function of the instrument, suppressing power at the smallest angular scales. Conversely, if the beam window function is known, the power spectrum can be deconvolved by dividing by the beam window function. Because CIB studies encompass relatively small parts of the sky (angular scales $\lesssim 1$ sr) we adopt the Cartesian formulation of the Fourier analysis i.e. a flat sky approximation. However, the CIB fluctuations can be equivalently described using spherical harmonics, $C_l = \langle |a_{lm}|^2 \rangle$. In this description, the magnitude of the CIB fluctuation on scale π/l radian for large l is

$$\sim l^2 C_l / 2\pi.$$

1.2 CIB Measurements

Observationally, the CIB is difficult to distinguish from the generally brighter foregrounds within the solar system and the Milky Way. The primary objective of the DIRBE instrument on board COBE was to measure, or significantly constrain, the CIB in the 1.25–240 μm range. Both the foreground and background results from DIRBE were presented in a series of papers (16; 17; 18; 19) and were followed by several investigations attempting to extract the isotropic component (mean level) of the CIB (20; 21; 22; 23). The CIB levels derived are in mutual agreement despite very different methods of foreground removal. In addition, studies from subsequent Japanese infrared missions, IRTS and Akari, are consistent with the DIRBE-derived CIB (24; 25). Figure 1.3 summarizes the measurements of the CIB flux in the 1–5 μm range. They all seem to indicate CIB levels in excess of the flux from integrated galaxy counts from high resolution surveys. The excess, a factor of 2–8 growing towards shorter NIR wavelengths (26), was initially suggested to originate from massive metal-free stars in the early universe inaccessible to direct detection (27; 28). However, the energetic requirements for such a population to outshine the combined emission from galaxies of later times was shown to be astrophysically infeasible (29; 30).

Because of the large systematic uncertainties associated with modeling and subtracting foreground emissions from i) the zodiacal light arising from interplan-

etary dust, ii) Galactic cirrus arising from the interstellar medium (ISM), and iii) stars within the Milky Way, none of the detections of the isotropic CIB can be considered particularly robust. In addition, the NIR colors of the uncovered CIB do not differ much from the spectrum of the bright foreground emissions making it difficult to separate components. The very existence of the CIB excess has also been put to question as the opacity it would supply for high energy photons traveling through space is in tension with recent blazar studies (see Chapter 3). It has been suggested that the excess CIB in the NIR is in fact caused by inaccurate Zodiacal Light subtraction (see e.g. 31). While the direct CIB measurements continue to be debated, fluctuation studies are now being pursued as an alternative probe of the CIB that are much less sensitive to foreground emission (see Section 1.4).

The total flux from galaxies detected in deep surveys gives an important measure of the CIB. In principle, the combined flux from all discrete sources should be able to account for the bulk of the CIB energy budget. Galaxy counts in the NIR have now been measured to deep levels in J , H , K bands, both with observations from the ground (e.g. the Subaru telescope (32)) and from the Hubble Space Telescope (33). At slightly longer NIR wavelengths, the Spitzer Space Telescope has provided deep counts in the IRAC bands (3.6 and $4.5\mu\text{m}$) reaching ~ 26 mag (34; 35). The integrated CIB from resolved sources seems to saturate around $m_{\text{AB}} \simeq 20 - 22$ converging to a fixed value. Figure 1.3 shows the integrated CIB from resolved sources in the $1-5\mu\text{m}$ range that provide lower limits for the net CIB. As mentioned above, the resolved CIB cannot account for all of the isotropic CIB flux. This may or may not be attributable to foreground contamination.

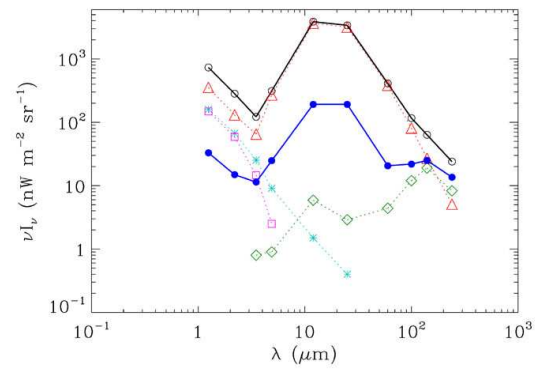
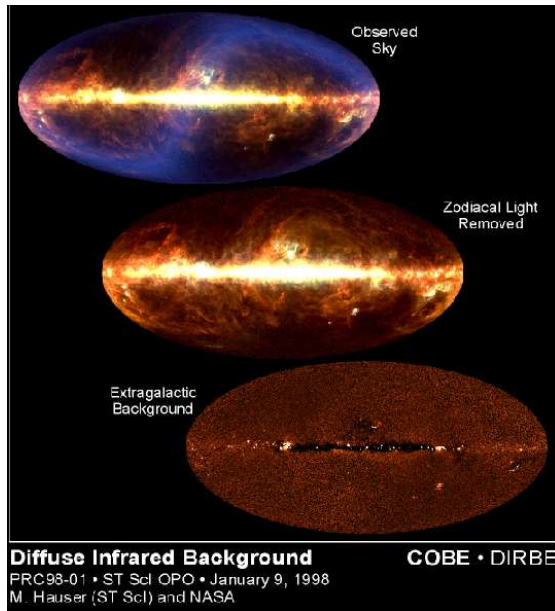


Figure 1.2 *Left:* The infrared sky seen by DIRBE (top). With Zodiacal Light removed (center). The CIB is what remains after all foregrounds have been modeled and subtracted (Credit: M. Hauser, NASA) *Right:* Foreground contributions to the DIRBE data at $1.25\text{--}240\mu\text{m}$ in the Lockman Hole: observed sky brightness (open circles), interplanetary dust (triangles), bright Galactic sources (squares), faint Galactic sources (asterisks), and the interstellar medium (diamonds). The residuals after removing all foregrounds from the observed brightness are shown in solid circles (adopted from Hauser et al. 1998 (16))

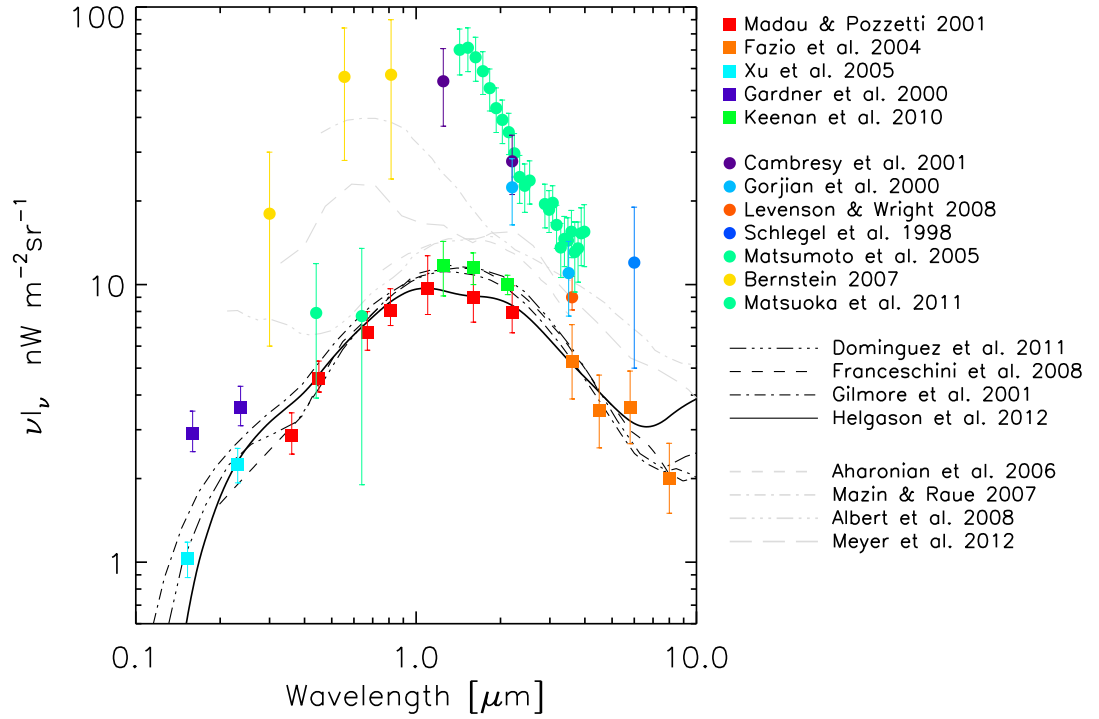


Figure 1.3 The extragalactic background light from 0.1-10 μm . Solid circles show direct measurements of the mean level. Filled squares represent integrated counts of resolved sources which give a lower limit for the background. Black lines show several background models based on galaxy evolution across cosmic history. The light grey lines show various upper limits for the total CIB based on γ -ray absorption in blazar spectra. References for measurements and models are displayed on the right.

1.3 γ -ray Opacity

The CIB supplies opacity for propagating high energy GeV-TeV photons via an electron-positron pair production ($\gamma\gamma \rightarrow e^+e^-$) (36; 37). This will show up as an absorption feature in the spectra of extragalactic TeV sources. For a head-on collision of two photons, the condition for pair production is that there is sufficient energy in the center-of-mass frame such that $E_\gamma E_{\text{CIB}} \geq (m_e c^2)^2$. This means that in order to interact with a γ -ray of energy E_γ , background photons must have wavelengths of $\lesssim 5(E_\gamma/1 \text{ TeV})\mu\text{m}$. Determining the amount of γ -ray absorption across cosmic distances is of fundamental importance for a wide variety of current observatories such as the space-borne *Fermi*/LAT instrument operating at energies $\lesssim 500$ GeV and ground-based γ -ray telescopes probing energies $\gtrsim 1$ TeV. The distance at which the optical depth due to this interaction is $\tau_{\gamma\gamma} \sim 1$ defines a horizon of the observable universe at γ -ray energies, and has been a subject of extensive efforts designed to model the build-up of EBL with time from the posited emission history of galaxy populations (e.g., 38; 39; 40; 41).

The best γ -ray constraints on the CIB come from very high energy blazars, distant AGN with an energetic jet pointing towards the line of sight. The first upper limits for the amount of intervening CIB were deduced from theoretical limits for the hardness of the intrinsic blazar spectra (29; 42). Since then, a steadily increasing database of blazars has provided more robust limits using a variety of different criteria for the intrinsic spectrum (43; 44; 45; 46). As shown in Figure 1.3 (grey lines), the derived upper limits are invariably in tension with the direct CIB measurements,

allowing for no more than $5\text{--}20 \text{ nW m}^{-2}\text{sr}^{-1}$ in the $1\text{--}5\mu\text{m}$ range. In addition, there have been several recently claimed detections of the γ -ray horizon from jointly fitting (or stacking) blazar spectra at the very highest energies (47; 48; 49). These studies also indicate low levels of the excess CIB, roughly $1\text{--}5\text{nW m}^{-2}\text{sr}^{-1}$ above the contribution from resolved galaxies. The problem of reconciling the excess CIB with γ -ray limits thus remains unsolved. Whereas the majority view assigns the discrepancy to large systematic errors in CIB foreground removal, the robustness of blazar-based γ -ray studies themselves has also been questioned (50; 51). For example, if blazar jets are efficient particle accelerators, their cosmic rays can interact with the CIB and produce secondary γ -rays traveling in the same path. The production of secondary γ -rays along the line of sight would then lead to reduced levels of inferred CIB. Whether this effect is non-negligible remains an open question.

1.4 CIB Fluctuations

In order to avoid the difficulty of exactly modeling and subtracting bright foregrounds in direct CIB measurements, Kashlinsky et al. (1996a) proposed measuring the structure or anisotropy of the CIB via its angular power spectrum (52). Whereas the Zodiacal Light is bright across most IR wavelengths, the emission appears to be remarkably smooth and does not exhibit fluctuations greater than $\simeq 0.03\%$ (53). Furthermore, any such fluctuations will be subject to variation as the Earth moves within the interplanetary dust cloud and can be isolated by observing in different locations in Earth's orbit. This has provided upper limits on Zodiacal Light

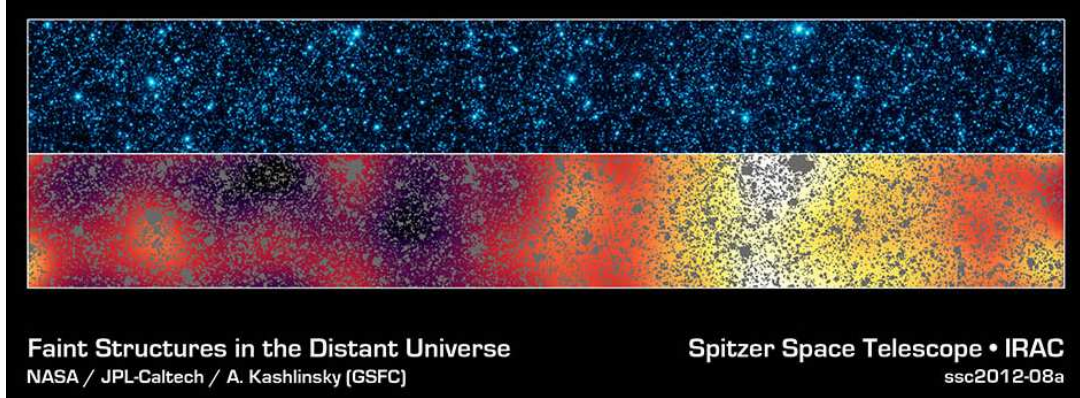


Figure 1.4 Illustrating the source subtracted CIB fluctuations. The top image shows a $\sim 1^\circ \times 0.12^\circ$ section of the sky observed by Spitzer at $3.6\mu\text{m}$. After careful modeling and masking of the resolved sources, the lower image depicts the large scale fluctuations observed (Credit: NASA/JPL, A. Kashlinsky).

fluctuations of $\simeq 10^{-3} \text{nWm}^{-2} \text{sr}^{-1}$ at $3.6\mu\text{m}$ (54). The diffuse emission from the ISM however, presents an irreducible component to any CIB fluctuation measurements. The Galactic cirrus exhibits a power-law structure that has been measured at several FIR wavelengths, $P(q) \propto q^n$ where $n \simeq -3$ (55; 56; 57). However, scaling these measurements down to $3.5\mu\text{m}$, based on the measured DIRBE spectrum of the ISM (18), the fluctuation levels tend to fall comfortably below the extragalactic signal in selected regions at high Galactic latitudes. One must be careful to use locations of low cirrus contamination such as the Lockman Hole at $(l, b) = (150^\circ, +53^\circ)$ (58). Stars within the Milky Way can be easily removed down to negligible levels in high resolution studies.

Detections of spatial structure in the CIB were initially based on datasets from *COBE*/DIRBE (59), the IRTS (24) and 2MASS (60; 61). More detailed fluctuations have been revealed after carefully masking resolved sources in deep NIR exposures and Fourier analyzing the pixels remaining in the maps (see Figure 1.4). This tech-

nique has led to successful measurements from several observatories *Spitzer*/IRAC, *HST*/NICMOS and *Akari*/IRC. Refs. (54; 62) have used deep exposures from *Spitzer*/IRAC (3.6-8.0 μ m) finding significant fluctuations after subtracting resolved sources down to faint levels, $m_{AB} \approx 25$. Small scale CIB fluctuations have also been measured at 1.1-1.6 μ m using *HST*/NICMOS observations (63; 64) and on arcminute scales in the 2.4-4.1 μ m range using the Akari satellite (65). More recently, ref. (66) have measured the *Spitzer*/IRAC out to $\lesssim 1^\circ$ using more extensive datasets from the *Spitzer Extended Deep Survey* (SEDS), confirming earlier results and extending the fluctuation measurement to much larger angular scales. These have since been confirmed independently in *Spitzer* measurements out to larger scales but somewhat less depth in the SWIRE survey (67). The present measurements, summarized in Figure 1.5, are all consistent with an extragalactic origin and necessitate an associated unresolved component in the CIB. The minimal CIB flux implied by the new sources responsible for these fluctuations is of order 0.5-2 nW m⁻²sr⁻¹ (62) and is well below the claimed direct CIB flux measurements from DIRBE (20), IRTS (24) and Akari (25), being consistent with limits placed by γ -ray attenuation from very high energy sources (42; 44; 47; 48).

The measured spatial power spectrum of the source-subtracted CIB fluctuations rises at angular scales $\gtrsim 20''$ (see Figure 1.5). The amplitude and shape of this rise is a direct measurement of the clustering properties of the underlying source populations, and thus a primary key of understanding their nature. The interpretation of these power spectra has been a subject of debate (68; 69; 70; 71; 72). It is now firmly established that the extragalactic signal is inconsistent with the emission

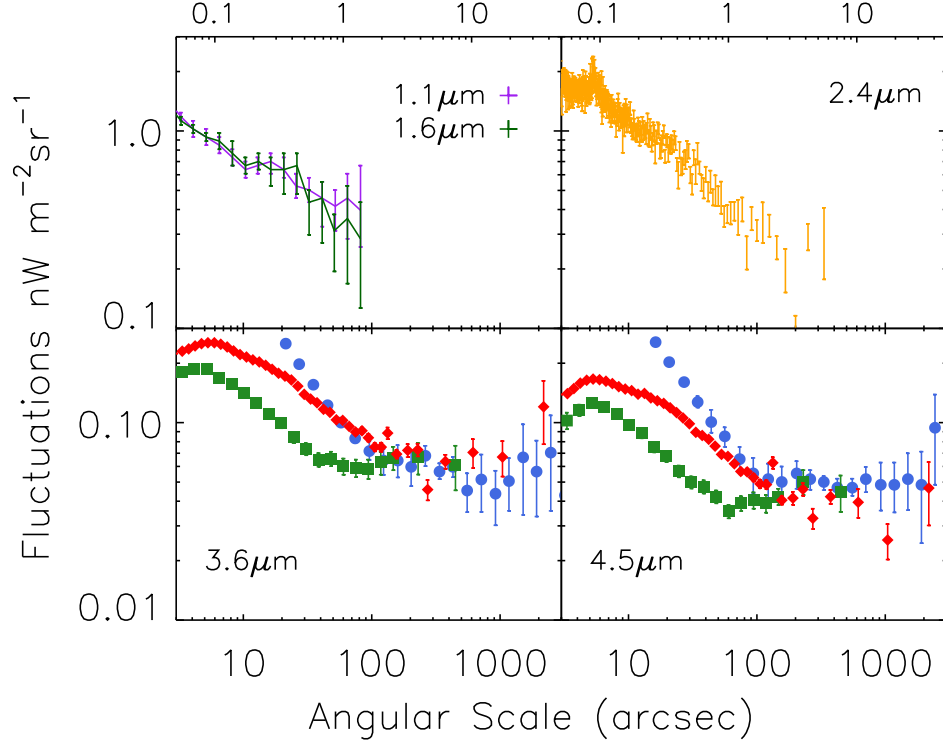


Figure 1.5 Current measurements of the source subtracted CIB fluctuations (rms) in the 1–5 μm range, shown as $q^2P(q)/2\pi$. Small scale measurements at 1.1 and 1.6 μm comes from HST/NICMOS (63; 64). Akari/IRC covers 2.4–4.1 μm but we only show the 2.4 μm data (65). The best measurements come from Spitzer/IRAC 3.6 and 4.5 μm . The green data points are from ref. (54), averaged over four deep fields. Red data points come from the SEDS survey (66) whereas the blue points are from the much shallower SWIRE field (67). All measurements show a consistent clustering signal on large scales whereas on small scales they differ significantly because unresolved galaxies, dominating at small scales, are masked/removed to very different depths.

of presently resolved galaxies ($z < 6$) with extrapolation to low luminosities (73). On the other hand, it was proposed that CIB fluctuations from the first light era could be measurable thus making the signal a critical tool for studying the high- z Universe (74; 75). All attributes of the signal are consistent with a high redshift origin but a definite redshift determination is lacking. The established properties can be broadly summarized as

1. the signal is very isotropic on the sky and local foregrounds arising from the Solar System and the Milky Way are not significant, indicating an **extra-galactic origin** (54; 65)
2. the power spectrum of the large scale CIB fluctuations is consistent with Λ CDM **clustering** out to $\sim 1^\circ$ (66; 67)
3. combining measurements from Akari and Spitzer, the fluctuations show a **blue spectrum** roughly $\propto \lambda^{-3}$ consistent with hot stellar/nebular emissions (65)
4. the strong clustering on large scales is coupled with the low shot noise levels on small scales implying **very abundant and intrinsically faint populations** (69)
5. the clustering signal is **inconsistent with faint galaxy populations** at $z \lesssim 6$ extrapolated to faint luminosities (73)
6. the large scale clustering exhibits **no spatial correlations with deep Hubble/ACS maps** $\lesssim 0.9 \mu\text{m}$ implying that the sources are extremely faint and/or

that their Lyman-break is redshifted well into the near-IR, $(1+z)0.1\mu\text{m} \gtrsim 0.9\mu\text{m}$ (76)

7. the source subtracted CIB maps show a **significant spatial correlation with the unresolved Cosmic X-ray Background (CXB)** at 0.5-2 keV implying X-ray emitters among the CIB sources (77)
8. the diffuse CIB in the final maps **do not spatially correlate with the subtracted/masked sources or outer halos** around them mimicking missing light (78)

An alternative scenario recently has been proposed to explain the signal is in the form of intrahalo light from stars stripped of their paternal halos at intermediate redshifts of $z \sim (1-4)$ (67). While this model is consistent with bullet points 1–3 above, it fails to account for all of the others (4–8). The notion that the large scale CIB fluctuations arise from known galaxies or any associated emission is currently disfavored.

Additional insights are now emerging from cross-correlations with other wavelengths. Cappelluti et al. 2013 provided observational evidence for a substantial population of accreting sources among the CIB sources raising the intriguing possibility of extensive black hole activity in the early Universe (77). The authors used deep source-subtracted *Spitzer*/IRAC and Chandra maps of a common region to reveal a highly significant cross-power $(3.8, 5.6)\sigma$ between the unresolved CIB at 3.6, 4.5 μm and the soft 0.5-2 keV CXB. An interesting and specific model for the discovered CIB \times CXB signal explained it in terms of direct collapse black holes at

$z \gtrsim 12 - 15$ by a mechanism which is capable of reproducing both the unexplained CIB and cross CIB \times CXB fluctuation signals without violating constraints imposed by the total measured soft CXB (79). However, before models of such hypothetical high- z sources can be favored as leading explanations for the measured signal, a more quantitative analysis of known source classes at $z \lesssim 6$ is needed. There are a variety of known mechanisms of X-ray production capable of producing spatial correlations with optical/IR emitting counterparts.

This dissertation is structured as follows. In Chapter 2 we present an empirical reconstruction of the CIB fluctuations from galaxy populations at $z \lesssim 6$. In Chapter 3 we reconstruct the evolving build-up of the CIB from survey data and derive the γ -ray optical depth of the universe as a function of energy and redshift. In Chapter 4 we model the sources of the CXB to investigate the origins of the spatial cross-correlation signal seen between the unresolved CIB and CXB. We conclude by summarizing and discussing future prospects in Chapter 5.

Chapter 2: CIB from Known Galaxy Population: An Empirical Model

2.1 Overview

Galaxy populations build up extragalactic background light over cosmic time. In addition to the contribution galaxies resolved in deep surveys there remains a widespread faint population escaping detection that nevertheless contributes to the unresolved CIB. It is thus important to understand the CIB in terms of galaxy evolution, both the bright component dominating the luminosity density and the faint unresolved regime dominating source-subtracted fluctuation studies. Modeling the populations of the EBL has been attempted using various mixtures of theory and observations. Backward evolution scenarios take the present galaxy populations and extrapolate them to higher redshift (e.g., 80; 39), while forward evolution follows dark matter merger trees starting from the cosmological initial conditions, using semi-analytical models of galaxy formation (81; 82). We present an alternative empirical approach by examining the best-fit Schechter parameters (83) of 233 luminosity functions covering the UV, optical and near-IR out to redshifts $z \sim 3-8$. This is made possible by the many galaxy surveys conducted in recent years that

provide a wealth of data in multiple bands and cover a wide range of redshifts. We provide empirical fitting formulae describing the smooth evolution of multi-band LFs with redshift, and construct lightcones containing all populations seen in the near-IR bands, selected at each redshift such that $\lambda_{\text{NIR}}^{\text{obs}} = (1+z)\lambda^{\text{rest}}$. By doing this we are able to reconstruct the entire history of light production produced by known galaxy populations relying exclusively on observations. Individually, LFs only probe specific rest-frame wavelengths for a limited range of redshifts, while together we can use them to infer the source distribution composing the background light in the $0.1\text{-}5.0\mu\text{m}$ range. Our only theoretical assumptions concern the clustering properties of the unresolved sources which are modeled according to the well-established concordance ΛCDM model (see Section 2.5). We refer to (84) for a good review on the properties of luminosity functions and how they are measured.

2.2 Measurements of the Galaxy Luminosity Function

The total emission seen in the near-IR bands ($JHKLM$) depends on the contribution of local near-IR galaxies as well as redshifted light radiated at shorter rest-frame wavelengths. To quantify the present day background produced by galaxies, we have utilized measurements of luminosity functions probing all rest-frame wavelengths in the interval $0.1 < \lambda < 5.0\mu\text{m}$ anywhere in the redshift cone. This results in a compilation of 233 LFs from a large variety of surveys which we list in Table 2.1. Our approach does not depend on stellar population synthesis models (e.g., 85) and we do not need to make an assumption for the IMF. Rather, in this method we

predict the levels of CIB fluctuations directly from the available data, assuming only i) standard Λ CDM model of structure formation and ii), the validity of a Schechter-type LF after fitting its parameters to the data. All the LFs we use have been characterized by a Schechter function (83),

$$\phi(M)dM = 0.4 \ln(10) \phi^* (10^{0.4(M^*-M)})^{\alpha+1} \exp(-10^{0.4(M^*-M)}) dM, \quad (2.1)$$

determined by the normalization, ϕ^* , characteristic absolute magnitude, M^* and the faint-end slope, α . By integrating Equation (2.1), the luminosity density can be shown to be $\mathcal{L} = \phi^* L^* \Gamma(\alpha+2)$ for $\alpha > -2$, where L^* is the characteristic luminosity and $\Gamma(x)$ is the Gamma function. All the Schechter LFs used are shown in Figure 2.1.

The Schechter LF is usually found to fit the data fairly accurately but deviations are seen, in particular when fitting a wide range of luminosities. At low- z for example, ref. (86) find that the shape does not fit the sharp downturn seen at M^* and both ref. (87) and (88) find an excess of bright galaxies in the blue SDSS bands. There are also hints of an upturn in the local LF at faint magnitudes where the Schechter fit does a poor job (89). We address this faint-end issue in Section 2.3.1, but note that sources at the bright end are efficiently removed from the maps in CIB fluctuations studies. At longer wavelengths ($>5\mu\text{m}$), a double power-law is found to provide a more adequate fit than the Schechter function (90; 91). The mutual consistency of measurements is a primary concern when comparing LFs in the literature. Inconsistencies can be caused by field-to-field variations, photometric system, k-corrections, type of LF-estimator, survey depth and completeness,

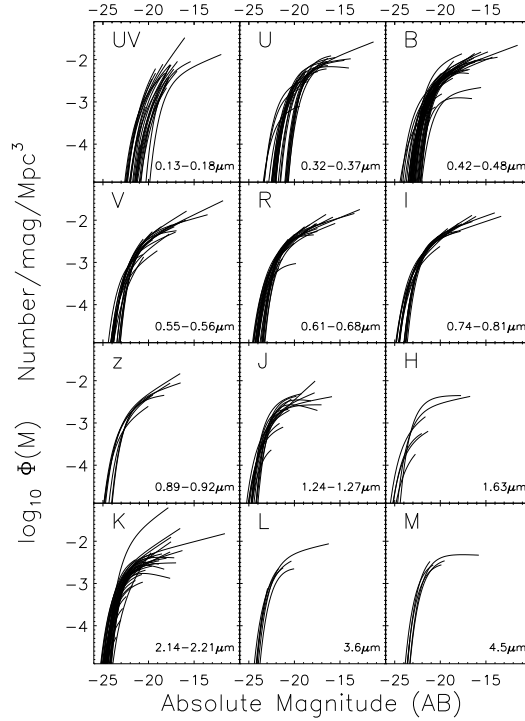


Figure 2.1 All 233 luminosity functions used in our analysis in Schechter parametrization (see original references in Table 2.1). The wavelength bins are listed in the panels (lower right) and their effective wavelengths are listed in Table 2.2 along with other properties. The LFs shown have a range of redshifts.

redshift binning, sample statistics, error estimates, etc. These undoubtedly account for differences in shape and amplitude of the measured LF (see Figure 2.3). We include a discussion of common issues in Appendix A.2, but these do not affect our results because we let all measurements collectively contribute to our derived LF.

Table 2.1: Measurements of the Luminosity Function

Reference	Rest-frame band	Redshift z	Sample N_{gal}	Selection $m_{\text{lim}}(AB)$	Survey Catalog / Field	Symbol / Color ^b
(92)	1500Å	0.2-1.2 1.75-3.4	1039	NUV<24.5 F450&F606<27	GALEX/VVDS HDF	green triangles(up)
(93)	NUV,FUV	0.055	896,1124	$m_{UV} < 20$	GALEX/2dF	blue circles
(94)	1500Å	0.5-2.5	284-403	$\lesssim 26$	HST ERS	yellow circles
(95)	1500Å	~ 8	70	$H < 27.5$	CANDLES/HUDF09/ERS	pink triangles(up)
(96)	1700Å	1.9-3.4	$\sim 15,000$	$\mathcal{R} < 25.5$	^a	blue crosses
(97)	1500Å	$\sim 4,5$	3808,539	$\lesssim 26-27$	Subaru Deep Field	blue squares
(98)	1500Å	$\sim 5,6$	~ 1500	$z' \lesssim 26$	SXDS/UKIDSS	purple squares
(99)	1500Å	7	22	$\lesssim 26$	SDF/GOODS-N	
(100)	1600Å,1350Å	$\sim 4,5,6$	4671,1416,627	$\lesssim 29$	HUDF/GOODS	violet triangles(down)
(101)	1600Å,1750Å	$\sim 7,8$	73,59	$\lesssim 26-29.4$	HUDF09	orange diamonds
(102)	$u'g'$	0.45-5	5558	$I < 26.8$	FORS Deep Field	Green triangles(down)
(103)	^{0.1} u	<0.3	43223	$u < 20.5$	SDSS	red squares
(104)	B	0.2-1.2	~ 34000	$R \lesssim 24$	DEEP2/COMBO-17	tan squares
(105)	b_j	<0.2	110500	<19.45	2dFGRS	purple squares
(87)	^{0.1} $ugriz$	0.1	147986	<16.5-18.3	SDSS	blue plus

(88)	$^{0.1}ugriz$	$\lesssim 0.2$	947053	$< 17-19$	SDSS	green crosses
(106)	$^{0.1}ugriz$	0.002-0.5	8647-12860	$r < 19.8$	GAMA	yellow squares
(107)	$UBVRI$	0.05-2.0	11034	$I < 24$	VIMOS-VLT Deep Survey	pink triangles(up)
(108)	$i'z'r'$	0.45-3.8	5558	$I < 26.8$	FDF	green circles
(109)	BVR	2.0-3.5	989	$K_s \lesssim 25$	MUSYC/FIRES/GOODS/EIS	orange circles
(110)	V	0.4-4.0	19403	$H < 27.8, K < 25.6$	^a	blue triangles(up)
(14)	$ugriz$	0.0033-0.1	2437-3267	$< 18-21$	MGC/UKIDSS/SDSS	purple diamonds
	$YJHK$		1589-1798	$< 17.5-18$		
(111)	UBR	0.1-2	18381	$R < 24.5$	GOODS-HST/CTIO/ESO	dark green diamonds
	J	0.1-1	2768	$K_s < 23.2$		
(86)	$b_j r_f$	< 0.2	138226	$b_j r_f < 15.6, 16.8$	6dFGS/2MASS	dark red plus
	JHK			$JHK < 14.7$	/SuperCOSMOS	
(112)	$ugriz$	< 0.1	22679	$r < 17.5$	SDSS	orange circles
	K		6282	$K < 15.5$	2MASS	
(113)	BK'	0.6-3.5	439	$K' < 24$	Subaru Deep Survey	red crosses
(114)	JH	1.5-3.5	3496	$K_s < 22.7-25.5$	MUSYC/FIRES/FIREWORKS	green squares
(115)	JK_s	0.2-1.3	489	$K_s < 20$	K20 Survey	tan plus
(116)	JK'	0.1-0.6	500	$K' < 19.4-20.9$	MUNICS	yellow crosses
(117)	JK_s	0.01-0.12	16922,15664	$JK_s \lesssim 15.5$	2dFGRS/2MASS	violet diamonds
(118)	JK_s	0.005-0.2	7081,5683	$JK_s \lesssim 15.5$	2dFGRS/2MASS	blue squares
(119)	K	0.01-0.3	40111	$K < 17.9, r < 17.6$	UKIDSS-LAS/SDSS	red triangle(up)

(120)	K_s	0.001-4	285	$K_s < 24.9$	HDFS/FIRES	blue triangles(down)
(121)	K_s	0.003-0.03	4192	$K_{20} < 13.35$	2MASS/CfA2/UZC	magenta circles
(122)	K	0.001-0.57	1056	$K < 15$	2dF/AAO	violet diamonds
(123)	K	0.2-2	21200	$m_{3.6mic} < 21.5$	SWIRE/VVDS /UKIDSS/CFHTLS	dark green squares
(124)	K	0.2-4	~ 50000	$K < 23$	UKIDSS/SXDS	orange plus
(90)	$L_{3.6\mu m} M_{4.5\mu m}$	0.01-0.6	34281	< 20.2	SWIRE/INT WFS	blue crosses
(125)	$L_{3.6\mu m} M_{4.5\mu m}$	0.01-0.6	4905,5847	$LM < 19, I < 20.4$	IRAC-SS/AGES	dark red circles

The measured LF are shown in Figure 2.1 and all Schechter parameters are displayed in Figure 2.3

^aData taken from multiple surveys/fields

^bThe symbols and color of the corresponding data points in Figure 2.2 and 2.3

2.3 Populating the Lightcone with known Galaxy Populations

This section outlines the step-by-step approach leading to the quantification of the galaxy distribution seen on the sky. Using the data in Table 2.1, we populate the evolving lightcone by placing the rest-frame galaxy distribution at a distance such that the associated emission is shifted into the near-IR bands in the observer frame, defined by $\lambda_{\text{NIR}}/(1+z)$. Initially, we bin the LFs according to their rest-frame wavelength in fiducial bands which we call \widetilde{UV} , \widetilde{U} , \widetilde{B} , \widetilde{V} , \widetilde{R} , \widetilde{I} , \widetilde{z} , \widetilde{J} , \widetilde{H} , \widetilde{K} , \widetilde{L} and \widetilde{M} (see Table 2.2). For example, measurements in rest-frame SDSS g' , Johnson B and 2dF b_j are binned together in our \widetilde{B} -band despite having an offset in center wavelength of about $0.03\mu\text{m}$. The largest offset occurs in our \widetilde{I} -bin where the centers of SDSS i and Johnson I is $0.063\mu\text{m}$. The uncertainty associated with the redshift of the population usually dominates these offsets so we do not correct for them. The centers of our fiducial bands, λ_{eff} , are taken to be the mean rest-frame wavelength of all measurements in the bin (see Table 2.2).

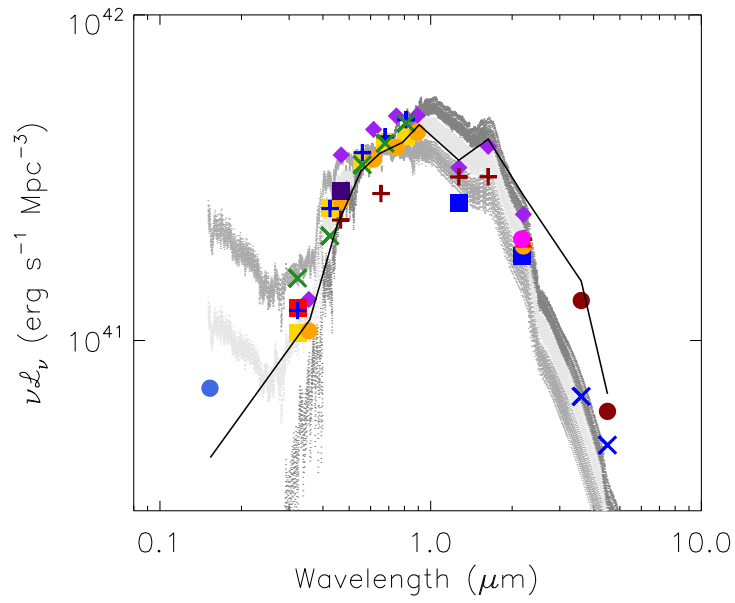


Figure 2.2 The local luminosity density according to all available LF measurements at $z < 0.12$ in Table 2.1, with symbols/colors indicated in the same Table. To avoid overcrowding the region of interest we omit error bars. The solid line shows the luminosity density in our fiducial bands as implied by our fits in Figure 2.3. The sets of gray lines show the contribution from galaxies of different metallicities and ages from synthetic galaxy SED spectra shown in Fig. 14 of (13). The bottom-gray curves show the early type stellar populations, the upper-dark show late type populations and middle-light lines show the average of the two contributions.

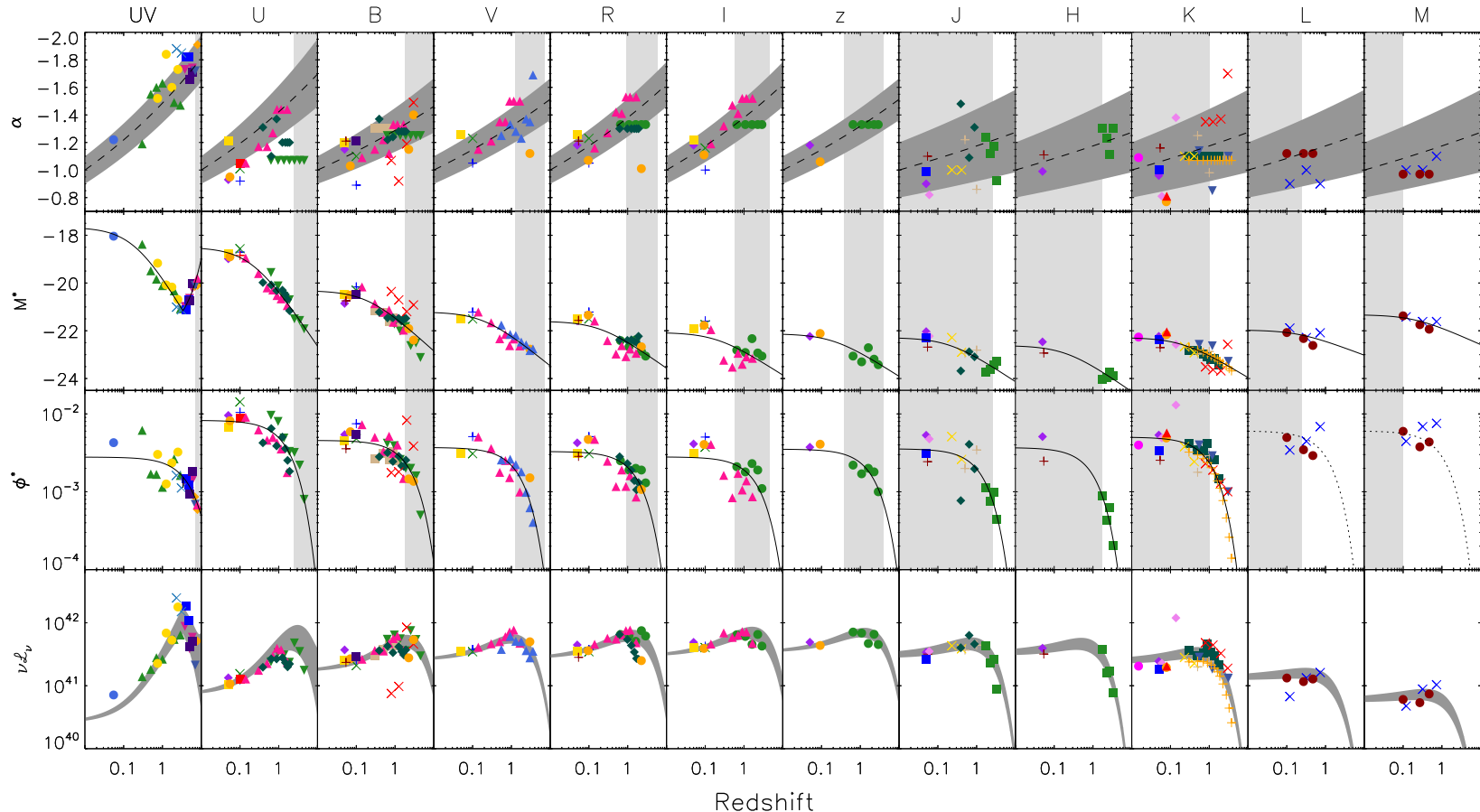


Figure 2.3 The measured Schechter parameters α, M^*, ϕ^* from the studies in Table 2.1 including the luminosity density, $\mathcal{L} = \phi^* L^* \Gamma(\alpha + 2)$, as a function of redshift. The different symbols/colors are listed along with the corresponding references in Table 2.1. We have omitted error bars for the sake of clarity. The solid curves show the evolutionary fits according to Equations (2.2)-(2.3) with the best-fit parameters listed in Table 2.2. We have modified M_{UV}^* to follow the fitting functions of ref. (101) at $z > 3.5$ to better match the turnover seen. We note that our fits are only empirically supported for $z \lesssim 4$, beyond which we extrapolate. The dashed curves in the α panels shows the evolution assumed in our default model whereas the dark shades areas encompass the range bracketed by our *high faint-end* (HFE) and *low faint-end* (LFE) models. These ranges are ultimately constrained by the observed galaxy counts (see Section 2.3.1). The shaded areas in the bottom row ($\nu \mathcal{L}_\nu$) is the evolving quantity $\phi(z) \nu L_\nu(z) \Gamma(\alpha(z) + 2)$ corresponding to this allowed range in $\alpha(z)$. The dotted curves in ϕ^* in \tilde{L} and \tilde{M} -bands are not fits to the data but are instead assumed to have the same form as the \tilde{K} -band fits. The light gray shaded areas correspond to the redshift regions for which the rest-frame emission redshifts into the observed NIR wavelengths of interest, defined to encompass the $1.25\text{-}4.5\mu\text{m}$ range. We are most concerned with the goodness of fit in these regimes.

By placing the entire population of each LF at the median redshift of the sample, z_{med} , we examine the evolution of the individual Schechter parameters (α, M^*, ϕ^*) in our fiducial bands. In the cases where z_{med} is not explicitly given by the authors, we choose the midpoint of the redshift bin of the LF measurement. The distances of the galaxies composing the LF is the dominant uncertainty in the resulting counts on the sky and we have therefore examined the effects of placing the LF at the opposite boundaries of the redshift bin (the resulting counts differ by less than a factor of two at the two extremes (see Section 2.4)). Figure 2.3 shows the Schechter parameters as a function of redshift from 0.15-4.5 μm . Across the spectrum, we see clear indication of evolution in M^* and ϕ^* and in some cases also in the poorly measured α .

Over time, galaxy populations evolve both in brightness and abundance. As small systems merge to form more massive ones, we expect a net increase in the number of bright and massive galaxies with time accompanied by a decrease in fainter ones. This is encoded in the evolution of ϕ^* (the number density of L^* systems), which we expect to increase with time whereas the faint-end slope, α should consequently flatten. The difference of the LF among rest-frame bands reflects the tendency of galaxies of different types being preferentially bright/faint at a given wavelength. The decomposition of the LF into red/blue galaxies typically shows an early-type population of individually bright galaxies with a diminishing faint-end whereas a the late-type population is composed of an increasing number of faint galaxies (104). The characteristic luminosity, L^* therefore depends heavily on the mixture of spectral types at any given epoch. Much work has been devoted to the

K-band LF where the stellar mass-to-light ratio is relatively stable and it can thus be used as an indicator for the stellar mass function (118). It is therefore natural to expect M_K^* to brighten with cosmic time as more mass becomes locked up in low-mass stars. This is indeed what is seen in the red/NIR bands, where the luminosity evolution is typically $\Delta M^* \simeq 0.5 - 1.0$ between redshift 0.1 and 1 whereas it is much stronger in the UV/blue rest-frames indicating higher star formation rates at earlier times. Extensive work has been devoted to measuring the UV LF which is a direct tracer of star formation rate. Lyman dropout galaxies found in deep optical/NIR surveys have allowed us to trace star formation back to very early epochs. We see M_{UV}^* brighten with increasing redshift and then turning over, thus roughly exhibiting the same behavior as the derived star formation history (Madau plot). The wide redshift range of available UV LF measurements makes it the only LF in which a non-monotonic evolution is distinctly seen in M_{UV}^* . In all other bands, the evolution of the Schechter parameters can be fitted with an analytic function to quantify the global evolution, while “washing” out outliers in the process. Several authors have parameterized the evolution in individual bands (e.g., 126; 124), but to our knowledge, our work is the first multi-wavelength parametric study of the evolution of the LF parameters. We find the following forms to fit the data well across our wide range of wavelengths and redshifts:

$$M^*(z) = M^*(z_0) - 2.5 \log [(1 + (z - z_0))^q] \quad (2.2)$$

$$\phi^*(z) = \phi^*(z_0) \exp [-p(z - z_0)] \quad (2.3)$$

and we assume the following *a priori* form for the faint-end slope

$$\alpha(z) = \alpha(z_0) (z/z_0)^r. \quad (2.4)$$

These fits are shown in Figure 2.3. For $M^*(z)$ and $\phi^*(z)$ we have taken $z_0=0.8$, but $z_0=0.01$ for $\alpha(z)$. The other best-fit parameters are listed in Table 2.2. Instead of selecting a preferred LF measurement for a given redshift in each band we have chosen to let all measurements contribute equally to the fitting process regardless of depth, area and sample size of the survey. Although there are a few notable discrepancies between the data and the fits we note that our IR-fluctuation results are unaffected as long as the fits remain good in the light shaded areas of Figure 2.3. These regions correspond to the distance for which the rest-frame emission is redshifted into the observed near-IR wavelengths of interest, defined to encompass the 1.25-4.5 μ m range. In the following sections we will rely on lightcones extrapolated from the highest measured redshift, typically $z\sim 4$, out to $z_{\max}=7$ (see Table 2.2). To account for the turnover observed in M_{UV}^* , we only use our Equation (2.2) out to $z\sim 3$ where they intersect the high- z fitting formulae given by ref. (101) which we adopt for $z\gtrsim 3$.

Evolution is not easily discerned in the faint-end slope, α , which by the very nature of surveys is hard to measure over large distances. For this reason we explore different scenarios for the behavior of $\alpha(z)$ which we explain in Section 2.3.1. In the \tilde{L} and \tilde{M} bands, the redshift range covered by the available measurements is so limited that we can only fit $M^*(z)$ but not the other Schechter parameters. Thus,

Table 2.2 Properties of the data shown in Figure 2.3 and the best-fit evolution parameters of Equations (2.2)-(2.4)

Band (1)	λ_{eff} (2)	N (3)	z_{max} (4)	M_0^*,q (5)	$\phi_{0,p}^*$ (6)	$\alpha_{0,r}$ (7)
\widetilde{UV}	0.15	24	8.0	-19.62,1.1	2.43,0.2	-1.00,0.086
\widetilde{U}	0.36	27	4.5	-20.20,1.0	5.46,0.5	-1.00,0.076
\widetilde{B}	0.45	44	4.5	-21.35,0.6	3.41,0.4	-1.00,0.055
\widetilde{V}	0.55	18	3.6	-22.13,0.5	2.42,0.5	-1.00,0.060
\widetilde{R}	0.65	25	3.0	-22.40,0.5	2.25,0.5	-1.00,0.070
\widetilde{I}	0.79	17	3.0	-22.80,0.4	2.05,0.4	-1.00,0.070
\widetilde{z}	0.91	7	2.9	-22.86,0.4	2.55,0.4	-1.00,0.060
\widetilde{J}	1.27	15	3.2	-23.04,0.4	2.21,0.6	-1.00,0.035
\widetilde{H}	1.63	6	3.2	-23.41,0.5	1.91,0.8	-1.00,0.035
\widetilde{K}	2.20	38	3.8	-22.97,0.4	2.74,0.8	-1.00,0.035
\widetilde{L}	3.60	6	0.7	-22.40,0.2	3.29,0.8*	-1.00,0.035
\widetilde{M}	4.50	6	0.7	-21.84,0.3	3.29,0.8*	-1.00,0.035

Note. — 1) Fiducial rest-frame band, (2) the effective wavelength in microns, (3) number of LFs used, (4) highest redshift of LF available in band, (5) Best-fit parameters for $M^*(z)$ with $z_0=0.8$, (6) Best-fit parameters for $\phi^*(z)$ with $z_0=0.8$ in units of 10^{-3}Mpc^{-3} , (7) The parameters for $\alpha(z)$ chosen to reflect the models (HFE&LFE) presented in Section 2.3.1. *assumed to be the same as in \widetilde{K}

for these two bands we assume $\phi^*(z)$ to take on the same form as the neighboring \widetilde{K} -band. Fortunately, the data available in the \widetilde{LM} -bands covers the redshift range of interest as is indicated by the shaded regions in Figure 2.3.

There is significant degeneracy in the Schechter parameters derived for a given galaxy population which can manifest itself in different values of (α, M^*, ϕ^*) depending on the LF-estimator used (see Appendix A.2). The overall shape of the LF can appear similar despite different Schechter parameters typically resulting in a comparable value for the luminosity density, $\mathcal{L} = \phi^* L^* \Gamma(\alpha + 2)$, which we display in the bottom panels in Figure 2.3. For example, ref. (107) and (108) derive comparable LFs despite giving very different values for the Schechter parameters. The gen-

eral agreement of the \mathcal{L} -data and the curves, $\phi^*(z)L^*(z)\Gamma(\alpha(z) + 2)$, indicates that our separate fits do not systematically over- or under-estimate the total luminosity density.

The second step is to populate the lightcone seen from the standpoint of the observer. Light from distant galaxies appearing in the observed X -band was emitted at wavelength $\lambda_X/(1+z)$ i.e. at all rest-frame wavelengths shortwards of λ_X throughout the redshift cone. We extract the Schechter parameters from our fits in Figure 2.3 at the redshift defined by $z_i = \lambda_X/\lambda_{Y^i} - 1$ where Y corresponds to our fiducial bands ($\widetilde{UV}\widetilde{U}\widetilde{B}\widetilde{V}\widetilde{R}\widetilde{I}\widetilde{z}\widetilde{J}\widetilde{H}\widetilde{K}\widetilde{L}\widetilde{M}$) and $\lambda_Y < \lambda_X$. Our template LFs then become

$$\Phi_i(M|z_i) = 0.4 \ln(10) \phi^*(z_i) \left(10^{0.4(M^*(z_i)-M)}\right)^{\alpha(z_i)+1} \exp(-10^{0.4(M^*(z_i)-M)}). \quad (2.5)$$

The continuous evolution of the LF seen in the X -band is then obtained by interpolating the Φ_i 's from $z = 0$ to z_{\max} . It should be noted that because of the $\alpha - M^*$ degeneracy, our separated $(\alpha(z), M^*(z), \phi^*(z))$ fits used in Equation (2.5) cause some amount of deviation from the original shape of the LF. This is a small effect in comparison with the general disagreement between individual authors on the shape of the LF. We refer to Appendix A.1 where an independent method is used to populate the lightcone, in which the original shapes of the LFs are kept intact. We show that the two different methods produce the same results, confirming the validity of our standard treatment.

As an example we show in Figure 2.4 the Schechter parameters characterizing

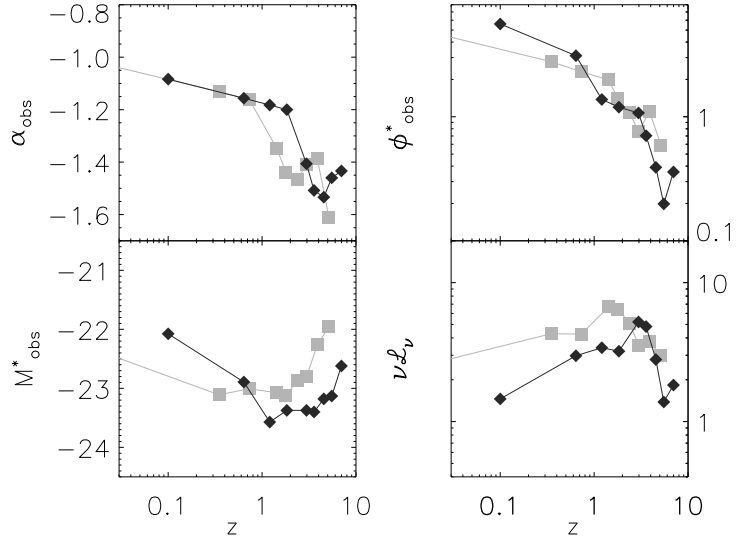


Figure 2.4 Evolution of the Schechter parameters and the luminosity density seen in the observed at $2.2\mu\text{m}$ (light squares) and $3.6\mu\text{m}$ (dark diamonds). The values are extracted from the fits in 2.3 at the appropriate redshifts. ϕ^* is in units of 10^{-3}Mpc^{-3} and $\nu\mathcal{L}_\nu$ in units of $10^{40}\text{erg}\cdot\text{s}^{-1}\cdot\text{Mpc}^{-3}$.

the LFs, probing the sky in two different observer-frame bands centered at $2.2, 3.6\mu\text{m}$ respectively. Although the abundance of galaxies diminishes by itself at high- z according to our fits, we impose a limit of $z_{\text{max}}=7$ in our modeling, beyond which we assume that ordinary galaxy populations were not yet established. But due to the steep drop of ϕ^* at high- z , our results are not sensitive to this parameter: in fact, using $z_{\text{max}}=30$, yields results nearly identical to our fiducial model. We emphasize that our evolution models are empirically supported out to $z\sim 4$ only, beyond which we extrapolate the evolution deduced at lower redshifts.

Information on distance is required in order to deduce the rest-frame LF from survey data i.e. absolute magnitudes need to be derived from apparent magnitudes. To derive the flux from galaxies in our lightcone we backtrack the original procedure i.e. go from absolute magnitudes back to apparent magnitudes. This implies undoing

any corrections the authors have made in this process

$$m = M + DM(z) + K(z) + E(z) + A_b(l, b), \quad (2.6)$$

where $DM(z)$ is the distance modulus, $K(z)$ is the k-correction, $E(z)$ is the evolution correction and A_b is the correction due to galactic extinction at the Galactic coordinate (l, b) . In LF measurements, authors typically use de-reddened magnitudes or correct for extinction using Galactic dust maps (127). This correction can be large in the UV/optical but becomes less severe towards the infrared where we have $A_V/A_K \sim 7-10$ approaching $\sim 15-20$ in the IRAC bands (128; 129). Since we are only concerned with emission entering the Milky Way as near-IR where the extinction correction is typically well within 0.1 mag we neglect it in Equation (2.6). Correcting for evolution is intended to make a sample drawn from a distribution of redshifts reflect the true luminosity function at a given epoch (usually z_{med} of the survey/bin) by accounting for changes in luminosity and number density over time (e.g., 87). This has been done for some local surveys where a considerable spread in the redshift distribution leaves more cosmic time for evolution to take place. This typically results in corrections of ~ 0.1 mag (112) but since the evolution correction simply acts to make the LF more accurate at a given redshift we do not need to make any adjustments. The only magnitude adjustment in Equation (2.6) of concern is the k-correction (130) which is needed to transform to the rest-frame by accounting for the redshifted SED of a given source. There are a variety of methods to deal with this SED dependence and we refer to Appendix A.2 for a more complete

discussion of two commonly used treatments in the literature. From the k-corrected absolute magnitudes, we simply require the spectral independent term to account for the redshift into the observed frame, $K(z) = -2.5 \log(1 + z)$. Equation (2.6) is now reduced to

$$m = M + DM(z) - 2.5 \log(1 + z), \quad (2.7)$$

which is the conversion we use. In Section 2.4 we show that we recover the observed number counts to a very good accuracy using this methodology.

2.3.1 The Faint-End Regime

The source subtracted CIB fluctuations are isolated to faint sources. By the nature of galaxy surveys, the faint-end is generally poorly constrained causing large uncertainties and scatter in measurements of α , especially at high- z . Because of this, many authors prefer to keep α fixed in their Schechter fits. Since the data does not show robust evolution in α in most bands (unlike M^* and ϕ^*) we explore variants of the behavior of the faint-end slope to get a feel for the sensitivity of CIB fluctuations to the abundance of faint galaxies. The substantial scatter in measurements of α leaves us some freedom in modifying the faint-end regime but we find that deep galaxy counts impose strict limits on the allowed range of faint-end slopes. This is most notable in $\tilde{B}\tilde{V}\tilde{R}\tilde{I}$, where a steep faint-end at $z=1-3$ leads to an overproduction of the observed JHK number counts in the faintest magnitude bins (see Figure 2.5). We therefore consider the range of allowed $\alpha(z)$ scenarios that collectively yield galaxy counts consistent with observations across all bands simultaneously. We leave M^*

and ϕ^* unchanged when varying α despite degeneracies in the parameters. We consider two models, *high faint-end* (HFE) and *low faint-end* (LFE), which, based on the resulting galaxy counts, are likely to bracket the true behavior of the faint-end of ordinary galaxy populations. These are shown in Figure 2.3 and 2.5 as the upper and lower boundaries of shaded regions. With the faint-end reasonably well constrained at $z=0$, ranging from -0.8 to -1.2, we fix α at these two values for LFE and HFE respectively and vary later evolution by changing the slope of the power-law in $\alpha(z)$ (called r in Equation (2.4))¹. Our HFE model is characteristic of strong steepening such as that found by ref. (107) (VVDS) out to $z\sim 1$ whereas the LFE implies a more modest evolution, closer to that of ref. (109; 110). Our LFE reflects a lack of evolution in the NIR i.e. $\alpha\sim\text{const.}$, which seems to be favored by some authors (131). We choose a faint-end cutoff for each template LF at $L_{cut} = 10^{-4}L^*$ for LFE and $10^{-8}L^*$ for HFE, thereby extrapolating the LF to very low luminosities. For both scenarios we find $10^{-5}L^*$ to be near saturation with flux contribution for fainter magnitude bins always being $<0.02 \text{ nW m}^{-2}\text{sr}^{-1}$. Our “default” model is the average of HFE and LFE with a cutoff at $10^{-5}L^*$.

We have chosen our LFE/HFE models so that they remain consistent with number counts data. The LFs dominating the faint counts in Figure 2.5 are mostly determined by the faint-end slope, α , at high and intermediate redshifts and it is important to emphasize that more extreme faint-end evolution models generally yield number counts that are inconsistent with observations. Alternatively, one

¹In the rest-frame UV/optical, where the low- z contribution does not matter for the observed NIR, we fix the low- z slope at -0.9 and -1.1 for LFE and HFE respectively.

could imagine an increase in the LF in the faintest magnitudes observed deviating from a Schechter function. In fact, such an upturn has been observed locally, for which a “double” Schechter function provides a better overall fit of the LF (89; 106). Allowing for a much steeper slope at $z=0$ to accommodate this possibility does not affect the resulting CIB fluctuations because the surface density of sources on the sky tends to be dominated by populations at larger distances. This can be illustrated by examining the underlying LFs of the resulting galaxy number counts in Figure 2.5, where the gray lines starting at the bright-end (from left) correspond to the local contribution (the thick line being the most local) moving to high- z LFs to the right. The rapid redshift evolution of the cosmic volume element prevents a large surface density of low- z sources and we find the faint counts always being dominated by populations at intermediate and high redshifts ($z \gtrsim 1$). In order for low- z sources to have sufficient densities to dominate the faint galaxy counts, and thereby also the unresolved fluctuations, we would need an extremely steep faint-end at $z=0$, becoming flatter towards increasing redshift i.e. $\alpha_{\text{low-}z} < \alpha_{\text{high-}z}$ which is the opposite of the observed evolution trend. We therefore consider our HFE scenario to be sufficiently extreme at low- z and making it steeper does not have an effect on our results. On the other hand, if a significant upturn in the LF exists at $z > 0.5$ (so far undetected), then this may result in a non-negligible contribution to the unresolved fluctuations. The large number of small halos predicted by the standard Λ CDM model permits such a scenario, especially if the first population of dwarfs with normal stellar populations formed in halos with mass $< 10^9 M_{\odot}$ (132; 133; 134). For instance, if the ultra-faint dwarf galaxies recently discovered around the Milky

Way can be identified as fossils of the first galaxies formed before reionization, that would imply that we have only discovered a small fraction of a widespread population of dwarfs which were almost certainly brighter in the past (135; 136; 137). However, it is unclear how to make the flux from this population sufficiently large to reproduce the measured fluctuation signal and, furthermore satellite dwarfs are efficiently masked along with their host galaxy in fluctuation measurements as displayed by the masking typically having angular radius of $\simeq 15'$ (ref. (78), see also Fig. A-3 in ref. (66)). In this work we probe whether the known galaxy populations, which we extrapolate to faint magnitudes in our HFE and LFE limits, can account for the observed source-subtracted CIB fluctuations, and the question of the nature of the new populations that can explain these fluctuations is, while important, outside the scope of the current discussion.

2.4 Number Counts and Background Light from LF Data

Galaxy number counts have the advantage of being free of the uncertainties associated with k-corrections and redshift determinations making them an important tool for both cosmology and galaxy evolution models. We project our lightcones onto the sky to obtain the galaxy number counts in each magnitude bin per unit solid angle:

$$\frac{dn}{dm} = \int \Phi(m|z) \frac{dV}{dzd\Omega} dz, \quad (2.8)$$

where $dV/dzd\Omega$ is the comoving volume element per solid angle. In Figure 2.5 we display the number counts from Equation (2.8) in the 0.45-4.5 μ m range and com-

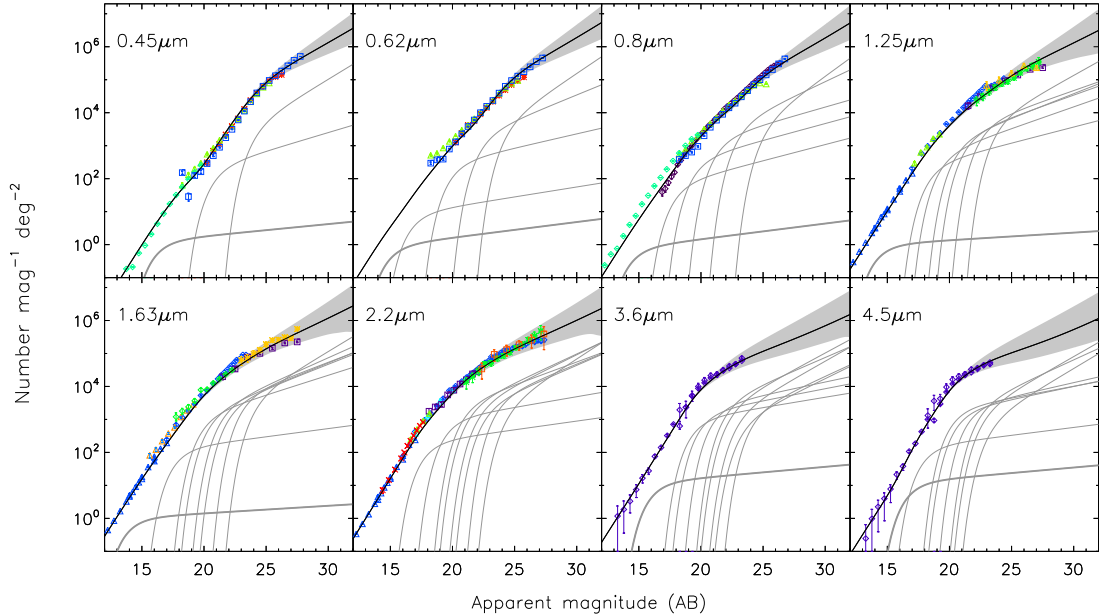


Figure 2.5 Galaxy number counts in our default description (solid curve) including the regions of bracketed by our two extreme models, HFE and LFE (gray shaded areas). The gray curves show the underlying template LFs in our fiducial bands (Equation (2.5)) which we interpolate and integrate to obtain the number counts via Equation (2.8). The low- z LF dominate the bright counts whereas high- and intermediate redshift LFs dominate the faint counts (from left to right). The most local available LF is shown as thick gray curves to demonstrate their negligible contribution to the faint counts. For $0.45\text{-}0.80\mu\text{m}$ panels the data are from references (138, red asterisks), (139, purple diamonds), (140, green triangles), (141, turquoise diamonds) and (142, blue squares). Data in the $1.25\text{-}2.2\mu\text{m}$ panels are taken from (143, green triangles), (144, purple squares), (145, green asterisks), (146, blue triangles), (32, blue diamonds), (147, yellow triangles), (148, yellow asterisks), (149, green diamonds), (150, turquoise triangles), (151, purple squares), (152, orange squares), (153, red crosses) and the $3.6\text{-}4.5\mu\text{m}$ data comes from (34, purple symbols).

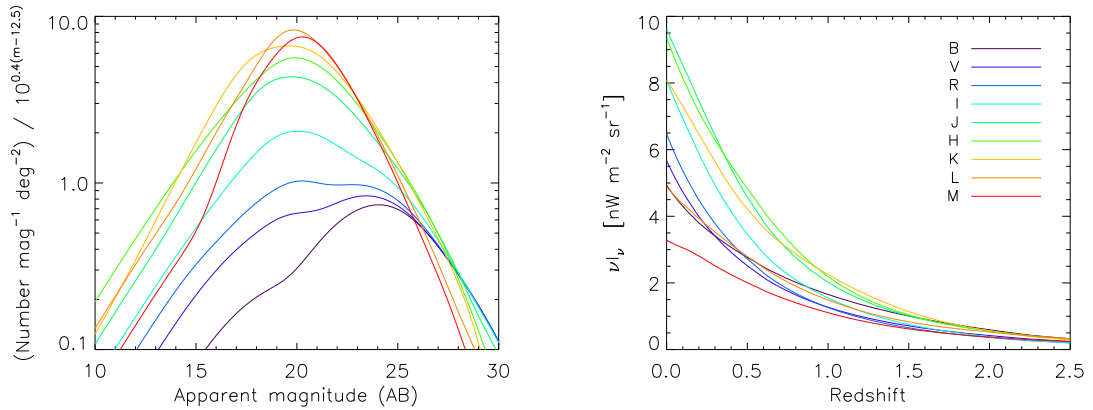


Figure 2.6 *Left:* Our reconstructed number counts in BRIJKHLM compared across the spectrum. The counts have been multiplied by a slope of $10^{-0.4}$ to bring out features in the shape. In this representation is proportional to the flux contribution from each magnitude bin. *Right:* The accumulation of integrated background light from galaxies over time. The flux builds-up from high- z (right) to low- z (left) reaching the present-day observed value listed in Table 2.3

pare with existing data in the literature. The agreement between our modeling and observed counts demonstrates the validity of our method. We also display the range bracketed by our two limiting models for the faint-end slope of the LF, as discussed in Section 2.3.1 (shaded areas). The gray curves in Figure 2.5 reflect the underlying template LFs contributing to the number counts in different redshift bins (bright/left to faint/right correspond roughly to low- z to high- z), elucidating the different populations governing the source surface density on the sky. It is reassuring, although not surprising, that we recover the shape of the galaxy counts using independent observations (the only assumption being the Schechter parametrization of the LF). This explicitly confirms that our multi-wavelength collection of observed LFs provides an accurate description of the photometric properties of resolved galaxies on the sky.

Figure 2.6 (left) examines how the shape of the number counts varies across the spectrum (0.45-4.5 μ m). Both the shape and amplitude of the counts are governed by the behavior of the $(\alpha(z), M^*(z), \phi^*(z))_{\text{obs}}$ -parameters shown in Figure 2.4 and some particular features deserve a few remarks. The bright counts all start out with a well known (Euclidian) slope of $d \log N/dm \sim 0.6$ continuing down to $m \sim 18-20$ where it flattens to ~ 0.4 . To first order this “knee” is simply caused by the transition from M^* -dominated to α -dominated regime. More specifically, a dip appears in the $BVRIJ$ number counts at $m \sim 18-20$ which arises from the lack of very bright galaxies at higher redshifts, i.e. M_{obs}^* becomes fainter with redshift (see Fig. 2.4). At higher redshifts (and shorter rest-frame wavelengths) we see a brightening again which is associated with star forming galaxies, bright in UV rest-frames. This brightening causes another feature at ~ 25 mag revealing a “double-knee” surrounding the dip. This is most pronounced in the $BVRI$ -counts but disappears at longer observed wavelengths where the UV rest-frame becomes too distant. Beyond $m \sim 25-26$, the counts are gradually diminished by the Λ CDM volume element. Depending on the exact faint-end model, the logarithmic slope in this regime is $\sim 0.2-0.3$ in $BVRI$, decreasing as we go to longer wavelengths.

Another clear feature of the number counts seen in Figure 2.6 (left), is the overall amplitude increase per magnitude bin as we go to longer observed wavelengths. We find the reasons for this to be twofold. First, the bright end is typically dominated by galaxies which are more luminous in the red bands such as the case of giant ellipticals. Therefore we see a larger number of them out to greater distances (in Fig. 2.3 we clearly see M^* becoming overall brighter from blue to red). Sec-

ond, when we look at the Universe through redder bands, we observe the redshifted light from bluer rest-frames emitted in epochs when the star formation activity was greater and consequently M^* was brighter. We further point out that our reconstructed counts are immune to confusion and agree well with the confusion corrected *Spitzer*/IRAC counts of ref. (34) (confusion enters around $m_{AB} \sim 20-22$).

We infer the amount of background light from galaxies from our reconstructed counts using Equation 1.19. Figure 2.6 (right) shows how the EBL flux builds up with cosmic time observed through *BVRIJKLM*. This results in present day values of the integrated background light of 9.6, 9.3, 8.1, 4.9 and 3.3 nW m⁻²sr⁻¹ at 1.25, 1.63, 2.2, 3.6 and 4.5 μ m respectively (see Table 2.3), which agree very well with Table 5 of ref. (13) and are also in general agreement with ref. (33), but slightly lower than the values found by ref. (32). A subtle underestimation could be due to the smooth fitting of the LF evolution which smears out any abrupt variation of the Schechter parameters which could either be physical.

2.5 CIB Fluctuations from Unresolved Galaxies

We now turn to evaluating the source-subtracted CIB fluctuations keeping in mind the procedure leading to their detection from raw images. If enough pixels remain in the maps after the masking of resolved sources, the fluctuations can be characterized via their angular power spectrum, which can be computed efficiently by using the fast Fourier transform (FFT). For a detailed description of the process of reducing CIB fluctuation data in the *Spitzer*/IRAC analysis we refer to (78).

Table 2.3 Extragalactic Background Light

Band	m_{lim} 22	m_{lim} 24	m_{lim} 26	m_{lim} 28	νI_ν All
<i>B</i>	3.33 ^{+1.72} _{-0.82}	2.26 ^{+1.56} _{-0.71}	1.17 ^{+1.24} _{-0.50}	0.52 ^{+0.88} _{-0.29}	4.92 ^{+1.81} _{-0.88}
<i>V</i>	2.95 ^{+1.54} _{-0.73}	1.90 ^{+1.36} _{-0.61}	0.96 ^{+1.05} _{-0.41}	0.42 ^{+0.73} _{-0.23}	5.65 ^{+1.73} _{-0.85}
<i>R</i>	2.86 ^{+1.54} _{-0.73}	1.75 ^{+1.31} _{-0.58}	0.85 ^{+0.98} _{-0.38}	0.37 ^{+0.67} _{-0.21}	6.56 ^{+1.82} _{-0.92}
<i>I</i>	2.81 ^{+1.58} _{-0.76}	1.58 ^{+1.27} _{-0.55}	0.72 ^{+0.92} _{-0.34}	0.30 ^{+0.61} _{-0.17}	7.97 ^{+2.01} _{-1.06}
<i>J</i>	2.59 ^{+1.56} _{-0.77}	1.20 ^{+1.10} _{-0.47}	0.48 ^{+0.72} _{-0.25}	0.18 ^{+0.45} _{-0.12}	9.60 ^{+2.40} _{-1.28}
<i>H</i>	2.25 ^{+1.50} _{-0.71}	0.96 ^{+0.96} _{-0.40}	0.36 ^{+0.57} _{-0.19}	0.13 ^{+0.34} _{-0.09}	9.34 ^{+2.59} _{-1.29}
<i>K</i>	1.74 ^{+1.41} _{-0.60}	0.69 ^{+0.82} _{-0.30}	0.24 ^{+0.44} _{-0.13}	0.08 ^{+0.23} _{-0.06}	8.09 ^{+2.52} _{-1.14}
<i>L</i>	0.98 ^{+1.05} _{-0.40}	0.34 ^{+0.57} _{-0.17}	0.11 ^{+0.27} _{-0.06}	0.03 ^{+0.12} _{-0.02}	4.87 ^{+1.72} _{-0.71}
<i>M</i>	0.75 ^{+0.83} _{-0.31}	0.24 ^{+0.45} _{-0.13}	0.07 ^{+0.20} _{-0.04}	0.02 ^{+0.09} _{-0.02}	3.28 ^{+1.21} _{-0.49}

Note. — The upper and lower values are not error but correspond to the HFE/LFE evolution scenarios of the faint-end slope. All quantities are in $\text{nW m}^{-2}\text{sr}^{-1}$.

As discussed in Section 1.1.3, the angular power spectrum from extragalactic sources consists of two components: i) the shot noise from the fluctuation in the number of unresolved sources entering the instrument beam, and ii) the clustering component arising from the correlation of galaxies on all scales. The two dimensional power spectrum of galaxies projected onto the sky can be related to their evolving three dimensional power spectrum, $P(k)$, by the Limber approximation (Equation 1.24). The flux production rate is empirically determined by our populated lightcones via

$$\frac{d\mathcal{F}}{dz} = \int_{m_{lim}}^{\infty} S(m) \frac{dn}{dm dz} dm. \quad (2.9)$$

In current fluctuation studies, sources are removed down to a fixed level of the shot-noise power (see Table 2.4). This is roughly equivalent to removing galaxies down to a limiting magnitude, m_{lim} , so that the remaining unresolved background

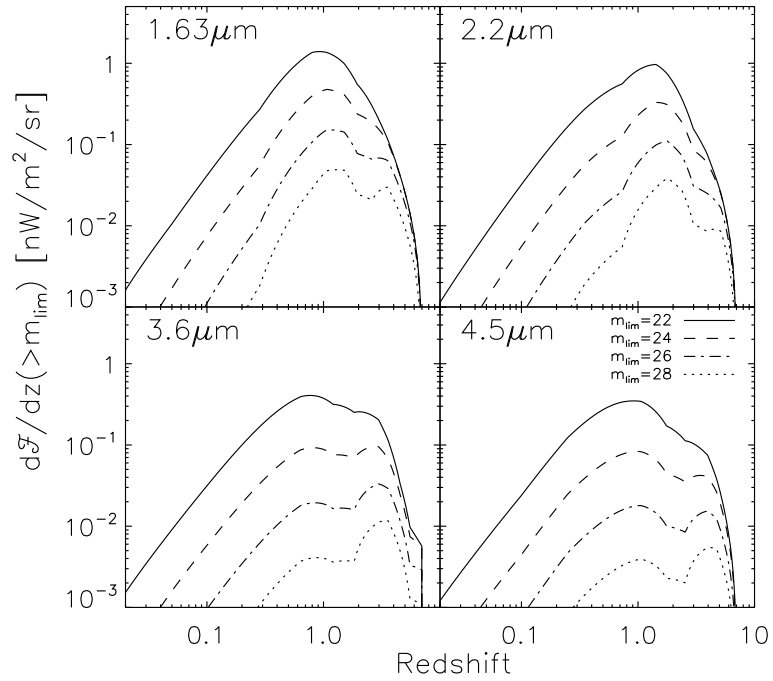


Figure 2.7 Flux production rate (times z) as a function of redshift in the unresolved regime shown for limiting magnitudes of 22, 24, 26, 28 (solid, dashed, dot-dashed, dotted curves respectively). The total unresolved flux under each curve listed in Table 2.3. The figure illustrates how removal of ever fainter sources isolates the unresolved component to higher redshifts.

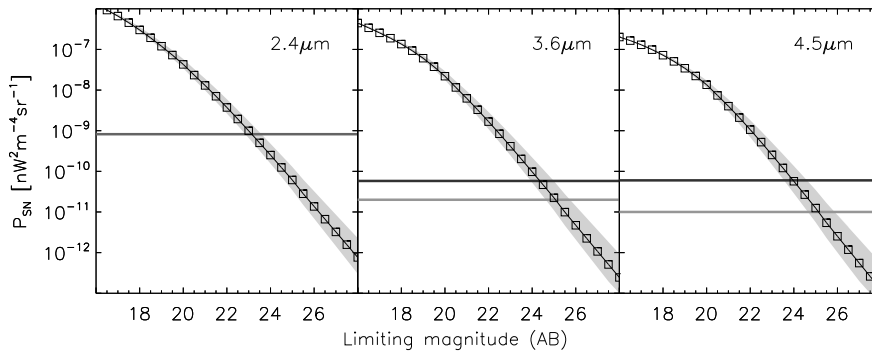


Figure 2.8 Shot-noise power amplitude after integrating the counts as a function of limiting magnitude (connected squares). The gray shaded area corresponds to the allowed range of the faint-end evolution of the LF. The thick gray lines show the levels of P_{SN} reached by ref. (65) at $2.4\mu\text{m}$, ref. (54) (dark) and ref. (62) (light) at 3.6 and $4.5\mu\text{m}$. The intersection corresponds to the limiting magnitude reached in these studies. We tabulate these values in Table 2.4. We point out that our model counts are immune to the effects of confusion.

is given by Equation (2.9). In Figure 2.7 we show the unresolved background from our modeling as a function of redshift, which illustrates how the process of galaxy removal isolates the background to progressively higher redshifts. Note, that there is very little contribution ($\lesssim 0.1 \text{ nW m}^{-2}\text{sr}^{-1}$) from galaxies at $z \lesssim 1$ after removing galaxies down to 26 AB mag. We find that for a limiting magnitude brighter than ~ 24 mag, the unresolved flux is mostly dominated by M^* galaxies at intermediate redshifts whereas galaxies at the faint-end takes over for $\gtrsim 24$ mag. In Table 2.3 we list the total integrated background in the $0.45\text{-}4.5\mu\text{m}$ range including the unresolved background for different limiting magnitudes corresponding to the curves in Figure 2.7.

2.5.1 Shot Noise

The shot-noise level seen in fluctuation measurements is critically important in order to identify the nature of the unresolved populations (69). Shot noise is a directly measurable quantity and is not affected by confusion which may be present. This allows us to evaluate the effective limiting magnitude, m_{lim} , for a given shot noise level using our models which are also immune to confusion. We calculate the shot noise associated with galaxies in our lightcones using Equation 1.25 and display it in Figure 2.8 as a function of limiting magnitude at the relevant bands. As fainter galaxies are removed the shot noise drops steadily in the same manner as seen in measurements. At ~ 22 mag we have already removed most M^* galaxies at $z \lesssim 1$ beyond which the shot noise is mostly determined by the faint-end of the LF. The horizontal lines in Figure 2.8 show the levels reached by the studies listed in Table 2.4. The intersection with our models agrees well with CIB fluctuation studies such as ref. (62) who removed galaxies down to $m \sim 25$ AB mag but is slightly brighter ($m \sim 24$) for the levels reached by ref. (54) who claimed to reach ~ 25 mag. Similarly, our shot noise levels agree well with those found by ref. (65) after removing galaxies down to AB magnitudes 22.9, 23.2 and 23.8 in the *AKARI*/IRC bands at 2.4, 3.2 and $4.1\mu\text{m}$ respectively. This confirms that the small scale power seen in these measurements is dominated by shot noise from unresolved galaxy populations. Table 2.4 lists the limiting magnitude predicted for the shot noise levels reached in several studies.

We have defined m_{lim} as a step-function, separating resolved/removed galaxies

Table 2.4 Limiting Magnitudes Implied by Shot Noise Levels

Reference	P_{SN}	m_{lim}
Band	[10^{-11} nW 2 m $^{-4}$ sr $^{-1}$]	(AB)
Thompson et al. 2007a		
F160W	<1.0	$\gtrsim 27$
Thompson et al. 2007b		
F110W	<1.8	$\gtrsim 27$
Kashlinsky et al. 2005a		
IRAC1 $_{3.6\mu m}$	5.8	24.4 $^{+0.7}_{-0.5}$
IRAC2 $_{4.5\mu m}$	6.0	24.0 $^{+0.6}_{-0.4}$
Kashlinsky et al. 2007a		
IRAC1 $_{3.6\mu m}$	2.0	25.1 $^{+0.7}_{-0.4}$
IRAC2 $_{4.5\mu m}$	1.0	25.1 $^{+0.8}_{-0.5}$
Matsumoto et al. 2011		
IRC $_{2.4\mu m}$	82*	23.2 $^{+0.4}_{-0.3}$
IRC $_{3.2\mu m}$	33*	23.3 $^{+0.5}_{-0.2}$
IRC $_{4.1\mu m}$	8.1*	23.9 $^{+0.5}_{-0.3}$

Note. — The upper and lower values are not error but correspond to the HFE/LFE evolution scenarios of the faint-end slope. *The values are inferred from Figure 3 of ref. (65).

from unresolved sources remaining. In practice however, the selection of the faintest detected objects is a smooth function of m depending on the survey completeness. Furthermore, source extraction can become limited by confusion, depending on exposure and instrument beam. Since our underlying reconstruction of galaxy counts from LFs is immune to confusion, we assume that the measured shot noise levels serve as a reliable indicator for the faintest sources removed, m_{lim} . This obviously assumes that the source removal is done properly and does not introduce spurious signals in the background fluctuations as discussed at length in ref. (78).

2.5.2 Galaxy Clustering

The shape and amplitude of the fluctuations produced in each redshift slice is dictated by the two evolving quantities, i) the amount of light production given by our reconstructed $d\mathcal{F}/dz$ in a given band, and ii) the clustering pattern of the sources in this epoch, described by their three-dimensional power spectrum, $P(k, z)$. For the latter quantity we assume that on large scales sources cluster according to the observationally established concordance Λ CDM power spectrum. However, luminous sources are known to be biased tracers of the dark matter distribution particularly in the non-linear regime where the correlations of sources depends on the *Halo Occupation Distribution* (HOD) of galaxies. We therefore consider a halo model description of the power spectrum which decomposes it into two terms, a two-halo term (P^{2h}) on large scales arising from the correlations of isolated halos, and a one-halo (P^{1h}) from correlations of particles within the same halo on small scales (154). We follow the treatment of ref. (155) and write,

$$P^{gal}(k) = P^{1h}(k) + P^{2h}(k), \quad (2.10)$$

where,

$$P^{1h}(k) = \int \frac{dn}{dM} \frac{2\langle N_{\text{sat}} \rangle \langle N_{\text{cen}} \rangle u(k|M) + \langle N_{\text{sat}} \rangle^2 u^2(k|M)}{\bar{n}_{\text{gal}}^2} dM, \quad (2.11)$$

$$P^{2h}(k) = P^{\text{lin}}(k) \left[\int \frac{dn}{dM} \frac{\langle N_{\text{gal}} \rangle}{\bar{n}_{\text{gal}}} b(M) u(k|M) dM \right]^2, \quad (2.12)$$

and dn/dM is the halo mass function (156, from), \bar{n}_{gal} is the average number density of galaxies, $P^{lin}(k)$ is the linear Λ CDM power spectrum (computed using the transfer function of ref. (157)), $u(k|M)$ is the normalized Fourier transform of the halo profile (158), and $b(M)$ is the halo bias (156). The occupation number has been separated into that of central galaxies, $\langle N_{cen} \rangle$, and satellite galaxies, $\langle N_{sat} \rangle$, such that

$$\langle N_{gal} \rangle = \langle N_{cen} \rangle + \langle N_{sat} \rangle. \quad (2.13)$$

We take the mass dependence of our HOD model to follow the four parameter description of ref. (159):

$$\langle N_{cen} \rangle = \frac{1}{2} \left[1 + \operatorname{erf} \left(\frac{\log M - \log M_{min}}{\sigma_{\log M}} \right) \right], \quad (2.14)$$

$$\langle N_{sat} \rangle = \frac{1}{2} \left[1 + \operatorname{erf} \left(\frac{\log M - \log 2M_{min}}{\sigma_{\log M}} \right) \right] \left(\frac{M}{M_{sat}} \right)^{\alpha_s}, \quad (2.15)$$

where $\langle N_{cen} \rangle$ is characterized by M_{min} , the minimum halo mass that can host a central galaxy and $\sigma_{\log M}$, which controls the width of the transition of the step from zero to one central galaxy. The satellite term has a cut-off mass which is twice as large as the one for central galaxies and grows as a power-law with a slope of α_s , normalized by M_{sat} . This form has been explored both numerically and observationally. Since the measurements of HOD-parameters are obtained from samples of resolved galaxies at low- z , their validity may not extend into the unresolved regime or, in particular, to higher redshifts. Since we are concerned with the unresolved regime it is important to note that the measured cut-off mass of central galaxies,

M_{\min} , is typically set by the lowest luminosity probed by the survey so halos may continue to host central galaxies to lower masses but are excluded due to selection criteria. In Section 2.4 we showed how the unresolved light is typically dominated by the faint-end of the LF for $m \gtrsim 25$ with most bright central galaxies removed out to $z \sim 3$ in measurements of CIB fluctuations. One would also expect the masking to eliminate most of the surrounding satellite galaxies. We have adopted the following parameters of the HOD-model motivated by SDSS measurements of ref. (160): $\sigma_{\log M} = 0.2$, $M_{\min} = 10^{10} M_{\odot}$, $M_{\text{sat}} = 5 \cdot 10^{10} M_{\odot}$, and $\alpha_s = 1$ where we have deliberately chosen a lower cut-off reflecting low mass halos hosting galaxies well into the unresolved regime, and a lower M_{sat} allowing for large amounts of unresolved satellite galaxies, while keeping $\alpha_s = 1$. It should be noted, that in the absence of any HOD-assumptions, a simple linear Λ CDM clustering with typical bias, $b^2 P^{\text{lin}}(k)$, produces nearly identical fluctuations on large scales. The one-halo term has white-noise power spectrum ($P = \text{const}$) with its amplitude limited from above by the measurements at small scales and so its modeling is irrelevant to interpreting the clustering signal at scales $> 1'$.

We assume that unresolved sources in our lightcones are uniformly mapped onto the halo distribution i.e. the clustering is independent of galaxy luminosity. In practice however, we expect the most luminous galaxies to be removed in the masking process along with most of the accompanying satellites. This could motivate one to introduce an upper mass limit in the integrals in Equations (2.11), $M_{\text{max}}(z)$. However, this would require an additional mass-to-light ratio assumption and since it would always result in a decrease of the clustering amplitude, we do not

apply $M_{\max}(z)$ and consider the result to be an upper limit for the resultant power spectrum. This includes the mass-dependent bias which is similarly integrated over the entire range of occupied halos ($\gtrsim 10^{10}$). The large scale (linear regime) galaxy bias seen by ref. (160) in the local SDSS sample is $b \approx 1$ when all galaxies are included. At somewhat higher redshifts, ref. (161) find $b = 1.38 \pm 0.05$ averaged over $0.5 < z < 1.2$. Further increase of the linear bias with redshift is expected on theoretical grounds as collapsing density peaks were increasingly rare in the past. The bias prescription used here shows the same general behavior (156). Several CIB studies at far-IR wavelengths claim a linear bias as high as $b=2-3$ for far-IR sources (e.g., 162; 163) but at these redshifts, the samples are already biased towards the most luminous objects due to selection effects. If anything, we expect the bias to be lower in the faint and unresolved regime after the more strongly biased luminous galaxies are masked and removed.

Fluctuations on large scales are always dominated by clustering in the linear regime (two-halo term). On the other hand, the non-linear clustering described by the one-halo term in Equation (2.11) exhibits a $P(k)=\text{const}$ behavior making it indistinguishable from shot noise in measurements. Given that we found excellent agreement between the shot noise in our models and the measurements at the same magnitude levels, there does not seem to be any need to invoke non-linear clustering to explain fluctuations on small-scales. In addition, we explored the pure dark-matter treatment of the non-linear clustering of ref. (164) but find it to be inconsequential in comparison with the shot noise dominated fluctuations on small scales. Although we see the one-halo term contributing somewhat to the HFE fluc-

tuations in Figure 2.9, it becomes less relevant if one accounts for the more massive halos being masked/removed along with satellites. In fact, we will see in Section 2.5.4 that current fluctuation measurements place a limit on the amount of non-linear power in the unresolved regime.

2.5.3 Comparing with Semi-Analytic Models

To compare our results with the clustering of halos seen in large scale N-body simulations, we have made use of the theoretical lightcones constructed by ref. (165). These mock catalogs are based on semi-analytical models for galaxy evolution (82) which are implemented on two very large dark matter simulations, the Millennium Simulation (166) and the Millennium-II Simulation (167). The simulations provide a description of the evolving spatial distribution of dark matter halos and subhalos whereas the nature of the baryonic content is described by the latest version of the semi-analytical Munich model (82). The Millennium Simulation follows structure formation in a box of side $500h^{-1}\text{Mpc}$ comoving with a resolution limit of $\sim 10^{10}h^{-1}M_{\odot}$ whereas the Millennium-II Simulation focuses on a region of $100h^{-1}\text{Mpc}$ but with complete merger trees down to $\sim 10^8h^{-1}M_{\odot}$. The predicted faint near-IR counts are higher than observations suggest due to an unusually high abundance of relatively low mass galaxies ($\sim 10^{10}M_{\odot}$) at $z > 1$ (the models were tuned to match the local populations). A comparison of the predicted correlation function of these models with local SDSS data shows decent agreement for massive galaxies whereas correlations of low mass systems are overpredicted, particularly at small

separations². For a detailed description of these models we refer to ref. (166), ref. (82) and ref. (165).

Despite the limitations mentioned above, we find that this study provides a useful comparison to our fluctuation analysis. After constructing images using the publicly available mock data (165), we calculate the projected angular power spectrum, convolved with the instrument beam. We analyze two independent regions observed in H, K, IRAC1 and IRAC2 each covering 1.4×1.4 degrees on the sky, extracting all galaxies in the magnitude range $m_{lim} < m < 30$ to produce the unresolved fluctuations which we display alongside our results in Figure 2.9. Because of the overabundance of faint galaxies at 3.6 and $4.5 \mu\text{m}$ in the semi-analytical description of ref. (82), we need to remove galaxies down to 0.2 mag deeper in order to normalize to a common shot noise level. This NIR overabundance (despite the resolution limit of $\sim 10^{10} h^{-1} M_{\odot}$) results in the Millennium fluctuations (dark-gray shades in Figure 2.9) being in closer agreement with our HFE scenario at 3.6 and $4.5 \mu\text{m}$ but are otherwise consistent with our main results.

2.5.4 Results

The clustering patterns emerging on the sky from our NIR lightcones are displayed in Figure 2.9. The limiting magnitudes have been chosen such as to normalize the shot noise (dot-dashed lines) to the measurements shown in each band. The shot-noise is seen to dominate the fluctuations on small scales whereas the clustering compo-

²The Millennium Simulation and the resulting lightcones of ref. (165) assume a WMAP1-based cosmology (168) with parameters $h=0.73$, $\Omega_m=0.25$, $\Omega_{\Lambda}=0.75$, $n=1$ and $\sigma_8=0.9$ which are slightly different than our adopted parameters of $h=0.7$, $\Omega_m=0.3$, $\Omega_{\Lambda}=0.7$ but this is of no appreciable consequence for the results in Figure 2.9.

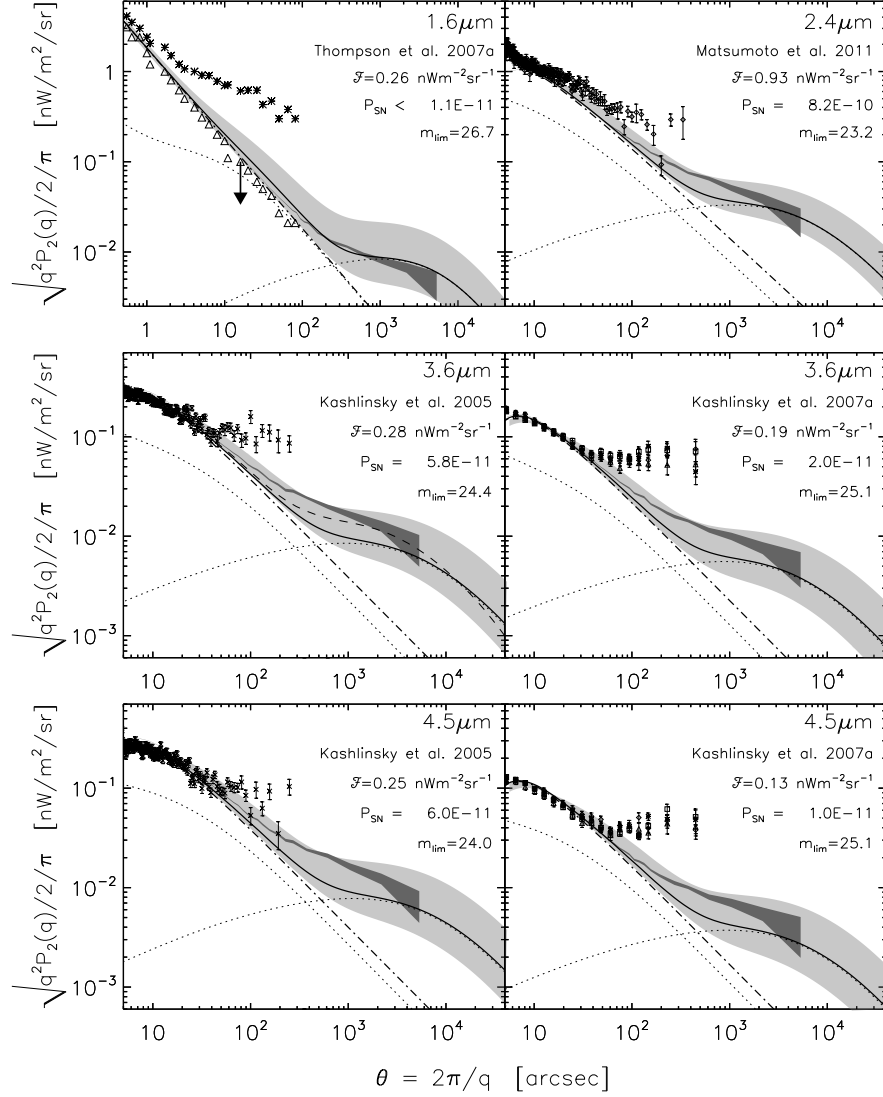


Figure 2.9 Models of the unresolved near-IR fluctuations compared to measurements from authors listed in the panels. We have chosen the limiting magnitude such that the models are normalized to the shot noise levels reached in these studies (including a contribution from a one-halo term). The solid curves show the total contribution from clustering and shot noise whereas the light shaded areas indicate the region bracketed by our HFE and LFE models. These are all suppressed by the instrument beam on small scales. The dotted lines indicate the separate one-halo and two-halo terms of the power spectrum. Shown in each panel is the total unresolved flux associated with the default model (\mathcal{F}), the values of P_{SN} (in units of nW²m⁻⁴sr⁻¹) and the associated m_{lim} . The dark shaded regions correspond to fluctuations arising from galaxies in the lightcones of (165) derived from the Millennium Simulation in the magnitude range $m_{lim} < m < 30$. Because of their overabundance of faint galaxies at 3.6 and 4.5 μm we have increased the m_{lim} of the Millennium fluctuations by 0.2 mag to normalize to the correct shot noise levels. In the 3.6 μm panel we also show the default model from ref. (169) (dashed line). In the 1.6 μm panel the notation follows Fig. 2 of ref. (63): asterisks correspond to fluctuations with all sources removed whereas the triangles indicate their estimate of the instrumental Gaussian noise.

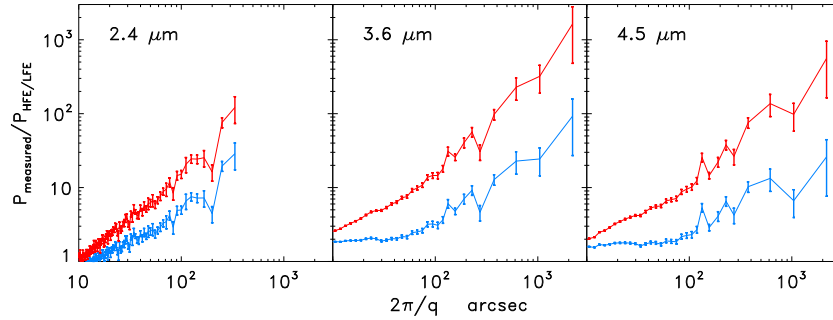


Figure 2.10 The lines show the ratio of the measured source-subtracted power spectrum from the *AKARI* 2.4 μm data and the latest *Spitzer*-based measurements at 3.6 and 4.5 μm (66) to the HFE and LFE expectations (red/upper and blue/lower respectively). The results show that the measured CIB fluctuations continue to diverge from our models as we go to larger scales and are thus unlikely to result from extra-biasing of these faint populations: in order to explain the measured signal the biasing would have to be 1) scale-dependent, i.e. non-linear, 2) biasing amplification would have to be more non-linear on scales where the amplitude of the underlying correlation function is weaker (larger scales), and 3) the biasing would have to be different at 3.6 and 4.5 μm .

ment becomes significant at arcminute scales. We focus on 1.6, 2.4, 3.6 and 4.5 μm where we can compare with measurements from *Hubble*/NICMOS, *AKARI*/IRC, and *Spitzer*/IRAC. Our models have been convolved with the beam profile (or PSF) of these instruments. It is immediately clear from Figure 2.9 that the contribution from known galaxy populations falls short of the measured clustering signal in every band shown. We briefly discuss each comparison:

Ref. (62) find excess fluctuations of $\delta F \sim 0.05\text{-}0.1 \text{ nW m}^{-2}\text{sr}^{-1}$ at arcminute scales in the *Spitzer*/IRAC channels after removing sources down to ~ 25 mag or shot-noise levels $P_{\text{SN}} \lesssim 3 \times 10^{-11} \text{ nW}^2\text{m}^{-4}\text{sr}^{-1}$. Galaxy populations remaining at the measured shot-noise levels cannot account for the observed fluctuations for any faint-end modeling of the LF. We have displayed the data of ref. (54) and ref. (62)

in panels side-by-side illustrating that the discrepancy gets larger as galaxies are removed to deeper levels. The unresolved flux associated with our default model is $0.18 \text{ nW m}^{-2}\text{sr}^{-1}$ in the deepest $3.6\mu\text{m}$ maps of ref. (62), so in order to explain the observed level of the excess fluctuations the relative levels of the source-subtracted CIB fluctuations would have to be close to non-linear, $\delta F/F \sim 1$, all the way to $\sim 10'$. The spatial spectra of the CIB fluctuations from the known galaxy populations is such that the gap increases toward large scales making it more difficult to explain. The additional linear biasing that would be required to amplify the arcminute scale signal to the observed levels is $b \sim 6 - 20$ which is highly unlikely for small systems in the $1 \lesssim z \lesssim 3$ range where most of the flux is produced. Figure 2.10 shows the ratio of the measured power spectrum from the new large scale *Spitzer*/IRAC data of ref. (66) to the power spectra of our HFE and LFE (red and blue), illustrating that the data keeps diverging from our models out to $\sim 0.5^\circ$. This further argues against the detected CIB fluctuations arising from the a faint-end extension of the known populations.

Ref. (170) stack deep *Spitzer* exposures to detect faint ACS galaxies beyond the detection threshold of the frames used in ref. (62) and explore the sensitivity of the IR-fluctuations to these ACS sources. Their stacked source detections down to 25.0-26.2 mag imply a net flux of $0.12\text{-}0.35 \text{ nW m}^{-2}\text{sr}^{-1}$. For comparison, the flux associated with our lightcones in the 25-26.2 mag range is 0.04 and 0.2 $\text{nW m}^{-2}\text{sr}^{-1}$ at $3.6\mu\text{m}$ for LFE and HFE respectively with $0.04\text{-}0.35 \text{ nW m}^{-2}\text{sr}^{-1}$ from still fainter galaxies, >26.2 mag. However, ref. (76) already demonstrated observationally the negligible correlations on arcminute scales between their source-

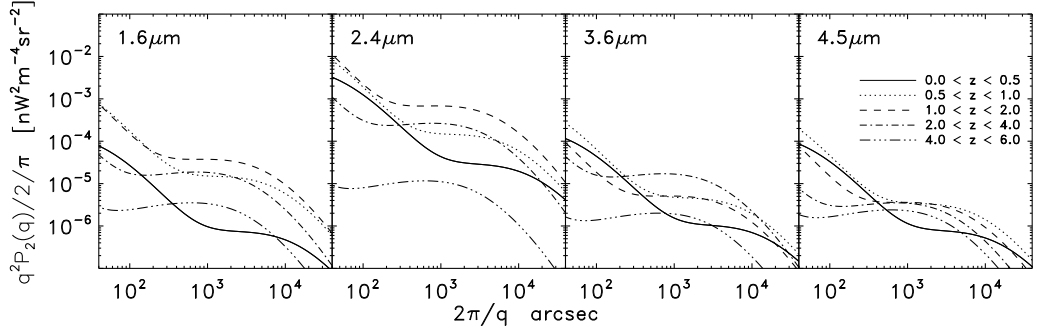


Figure 2.11 The contribution of different redshift bins to the unresolved IR-fluctuations shown in Figure 2.9 for the m_{lim} indicated in the panels. The 3.6 and 4.5 μm panels correspond to the models at the shot noise levels of ref. (62). The different set of lines correspond to the redshift bins indicated in the legend. This illustrates that depending on the observed band and the depth of source removal, the unresolved fluctuations from known galaxies are dominated by populations at different epochs. The amplitude and shape is governed by 1) the flux production history (see Fig. 2.7), and 2) the evolving power spectrum, $P(k, z)$. The non-linear clustering component is important at low- z but moves towards small scales for higher z . The dependence on the volume element is manifested in the peak of the ΛCDM power spectrum shifts towards smaller scales with increasing redshift.

subtracted CIB maps and ACS source maps.

Ref. (63) measure fluctuations at 1.6 μm on scales out to 80'' using *HST*/NICMOS (and at 1.1 μm in ref. (64)) and ascribe the signal to faint galaxies emitting at redshifts $z \sim 0.5-1.5$. Their fluctuations at 80'' have amplitudes of $\sim 0.4 \text{ nW m}^{-2}\text{sr}^{-1}$, which is a factor of 2-7 times higher than the total unresolved component, 0.06-0.20 $\text{nW m}^{-2}\text{sr}^{-1}$, for sources fainter than $>28 \text{ mag}$, indicating that the clustering of the underlying galaxies must be highly non-linear. For their CIB fluctuation levels to be reconciled with our empirical estimates, the one-halo term would have to be significantly higher, but then its amplitude would overshoot the data at all the other NIR wavelengths. If we take the upper limit on the shot noise at these wavelengths to be at the levels of the estimated instrument noise of ref. (63), then our shot noise

already matches at AB magnitude of ~ 27 (see triangles in Figure 2.9). But even at that level we cannot reproduce the fluctuations (asterisks) with the clustering of known galaxy populations out to $1'$. We point out in this context the clearly visible outer halos of the sources removed by Thompson et al (2007a, see their Fig. 4) whose contribution to their CIB fluctuations shown may be significant and should be estimated for more quantitative conclusions at $1.6 \mu\text{m}$.

The ref. (65) measured fluctuations at $2.4, 3.2, 4.1 \mu\text{m}$ using data *Akari* satellite and conclude that they are consistent with stars from early epochs confirming the identification proposed in ref. (54). The left panel in Fig. 2.10 confirms that the Akari signal at $2.4 \mu\text{m}$ cannot be explained by the remaining known galaxy populations.

In Figure 2.9 we also display the default model from ref. (169) (dashed lines) who combined a halo model and conditional luminosity functions to calculate IR-fluctuations at $3.6 \mu\text{m}$. Our models have a somewhat lower amplitude considering the fact that we use $m_{lim}=24.4$ as opposed to the 25.3 mag used by ref. (169) (and quoted in ref. (54)) but the two are in rough agreement nevertheless. For $m_{lim}=25.3$ our unresolved flux is $0.1 \text{ nW m}^{-2}\text{sr}^{-1}$ (LFE) which is roughly consistent with the $0.08 \text{ nW m}^{-2}\text{sr}^{-1}$ found by ref. (169). However, they claim that the fluctuations measured by ref. (54) at $3.6 \mu\text{m}$ can be explained by galaxies in the magnitude range 25.3 to 28.8 (AB) at $z \sim 1-3$. This is a somewhat puzzling conclusion when comparing their model with the data in Figure 2.9 as it clearly fails to account for the clustering excess³.

³The data-points from ref. (54) appear only in the electronic version of ref. (169).

In Figure 2.11 we show the contribution of different redshift bins to the unresolved IR-fluctuations for the m_{lim} indicated in the panels of Figure 2.9. This illustrates the different epochs in which unresolved galaxy populations contribute to the fluctuations in different observed NIR bands. The redshift dependence is governed by 1) the flux production history (see Fig. 2.7), and 2) the evolving power spectrum, $P(k, z)$. The Figure also reflects the dependence on the Λ CDM volume element per solid angle as the overall clustering pattern shifts towards smaller angular scales with increasing redshift.

2.6 Discussion

We have reconstructed the emission histories seen in the near-IR of present-day observers to model the unresolved CIB fluctuations and compared with current measurements. Our compilation of 233 luminosity functions used to populate light-cones at $z < 7$ reproduces the observed number counts remarkably well and accounts for the features shaping them. We assume the Schechter-type LF and model the evolution of its parameters from the available datasets. We then considered high and low faint-end LF limits within the constraints permitted by deep galaxy counts data. Extending these to faint magnitudes and to high- z we calculated the range of unresolved background flux in deep images and derived CIB-fluctuations from these galaxy populations predicted by the standard Λ CDM clustering power spectrum. We find good agreement between the predictions of our analysis and semi-analytical galaxy evolution models combined with the large scale Millennium N-body simula-

tion.

By varying the limiting magnitude of source subtraction we normalize our models to the observed shot noise levels, finding good agreement with the depths reached in current fluctuation measurements. We show that the known galaxy populations fail to account for the observed source subtracted CIB clustering signal in either LFE or HFE limits. Although, in principle, by varying m_{lim} one can find a population of brighter galaxies that matches the measured clustering amplitude at some angular scale, the associated shot noise levels always imply that all such populations have been removed in the source subtraction thereby not contributing to the unresolved fluctuations. Thus it means that the emitters producing the source-subtracted CIB fluctuations on arcminute scales are below the detection limits of current surveys and furthermore, cannot be a part of the known evolving galaxy populations. In other words, since the observed galaxy populations (extrapolated to very faint limits) cannot explain the measurements, the CIB fluctuations must originate in new populations so far unobserved in galaxy surveys i.e., a highly clustered population with low shot noise. Furthermore, this result is consistent with the lack of large scale correlations between the source-subtracted CIB maps and ACS source maps reaching AB mag of $\simeq 28$ (76). This implies that either the CIB fluctuations originate in a large unknown population of very faint systems or they are produced at high redshift populations whose Lyman break is shifted passed the longest ACS channel (at $0.9\mu\text{m}$).

Chapter 3: The γ -ray Opacity of the Universe

3.1 Overview

The extragalactic background light (EBL) supplies opacity for propagating high energy GeV-TeV photons via an electron-positron pair production ($\gamma\gamma \rightarrow e^+e^-$) (36; 37). Determining the transparency of the universe is of fundamental importance for a wide variety of current observatories such as the space-borne *Fermi*/LAT instrument operating at energies $\lesssim 500$ GeV and ground-based γ -ray telescopes probing energies $\gtrsim 1$ TeV. The distance at which the optical depth due to this interaction is $\tau_{\gamma\gamma} \sim 1$ defines a horizon of the observable universe at γ -ray energies, and has been a subject of extensive efforts designed to model the build-up of EBL with time from the posited emission history of galaxy populations (e.g., 38; 39; 40; 41).

Quantifying the optical depth of the universe to high energy photons requires knowledge of the properties of the intervening EBL. With galaxy populations observed over a wide range of wavelengths, one can uniquely reconstruct the optical depth at these energies out to redshifts $z \sim 4$. The wealth of galaxy survey data has recently reached adequate redshift coverage to make such empirical estimation of the evolving EBL feasible and independent of theoretical modeling describing the build-up of EBL over time. In this Chapter, we follow the methodology of Chapter

2 that relies exclusively on data from an extensive library of galaxy LFs and was shown to reproduce independent data from galaxy counts and the cosmic infrared background. We calculate the γ -ray opacity in the *Fermi*/LAT energy range using galaxy surveys probing $\lambda \leq 4.5\mu\text{m}$ out to $z \lesssim 4$. Extending to TeV energies, probed by the ground-based Cherenkov observations, we use measurements out to $24\ \mu\text{m}$; this extrapolation is robust for the redshifts currently probed by these observations. All in all, our data encompasses 18 finely sampled wavelengths from UV to mid-IR (0.15-24 μm). This empirical reconstruction defines the absolute floor of the photon-photon optical depth due to known galaxy populations and deviations from it would allow the characterization of any emissions inaccessible to direct telescopic studies (171; 172). We use this to argue that *Fermi*/LAT ($\lesssim 500\ \text{Gev}$) is particularly suitable for probing the CIB from early populations. The levels of this contribution may be identified or significantly constrained from the high- z gamma-ray absorption induced in the spectra of high/intermediate redshift sources; both GRBs and blazars (171; 173; 174). Whereas CIB fluctuation studies have established an unresolved CIB component, γ -ray studies offer a way to measure this component in a foreground-independent manner.

3.2 Reconstructing the Evolving EBL from Data

Evolving galaxy populations compose the bulk of the EBL which is dominated by starlight in the UV/optical and thermally radiating dust at longer IR wavelengths. We use multiwavelength survey data to fit the evolution of a single derived quantity,

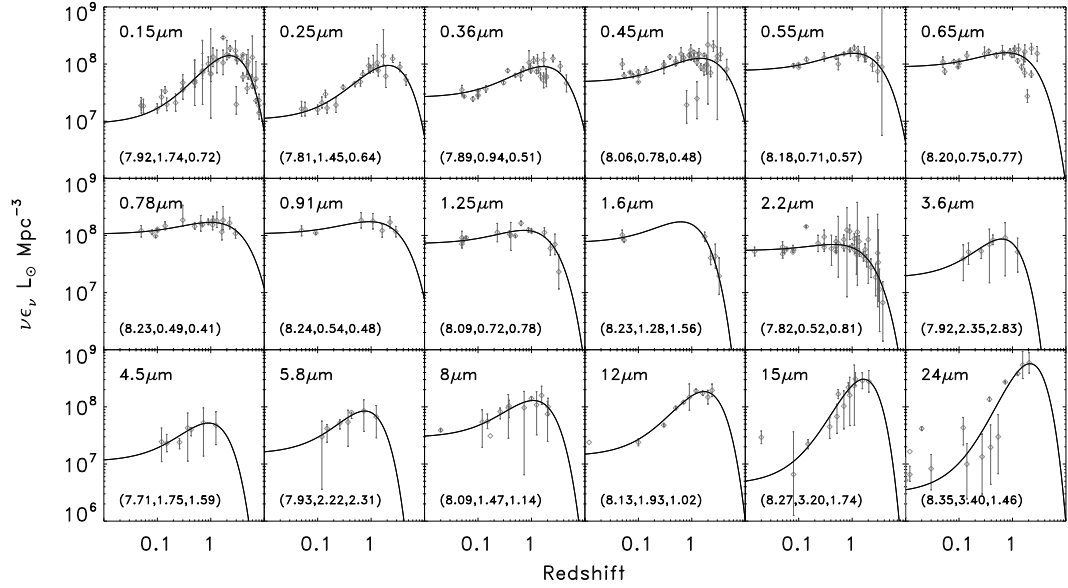


Figure 3.1 Measurements of the evolving luminosity density in our binned rest-frame wavelength range $0.14\text{--}25\mu\text{m}$ in units of $L_\odot\text{Mpc}^{-3}$. The solid curves are fits through the data points according to our fitting function (Equation 3.2) with best-fit parameters displayed in each panel as $(\log_{10} a_\lambda, b_\lambda, c_\lambda)$ where a_λ is also in $L_\odot\text{Mpc}^{-3}$. All data points have been converted to units with $h = 0.7$. The references for the data points can be found in Table 2.1 with the addition of UV data from (175; 176; 177; 178; 179; 180; 181) and mid-IR data from (182; 183; 184; 185; 186; 187; 91).

the luminosity density, in this otherwise assumption-free approach¹. The survey data used here extends the collection of LFs listed in Table 2.1 with expanded coverage in the UV (175; 176; 177; 178; 179; 180; 189; 181) and out to mid-IR wavelengths (187; 182; 183; 184; 185; 91; 186). This library now contains 342 measured LFs and allows us to reconstruct the evolving EBL and its spectrum in a finely sampled wavelength grid encompassing 0.15-24 μ m out to $z \sim 4$. This therefore assumes only the existence of populations as faint as $m_{\text{AB}} \sim 23 - 26$ with extrapolation to fainter magnitudes; additional populations at $z \gtrsim 6$ would then exist at still earlier times and have much fainter fluxes.

In the rest-frame UV to near-IR, the LF is well described by the conventional Schechter parameterization whereas at mid-IR wavelengths, the LF seems to be better described by a broken power-law or a double-exponential profile. Regardless of the functional form, the LFs can be integrated to give the comoving volume emissivity (we refer to this as the luminosity density) in the given rest-frame band

$$j_\nu(z) = \int L_\nu \phi(L_\nu, z) dL_\nu \quad (3.1)$$

where $\phi(L_\nu, z)$ is the measured LF. Each data point in Figure 3.1 represents the luminosity density given by the authors along with 1σ error bars. In the cases where this value is not given explicitly in the original papers, we have integrated the best-fit parameterized LF to obtain j_ν and have estimated the errors from the distribution of all of the values of j_ν allowed within the 1σ solutions of the individ-

¹Ref. (188) have used a similar approach to reconstruct the EBL at $< 0.7\mu$ m.

ual fit parameters. However, mutual comparison of uncertainties among the many different studies is not very meaningful since some authors include various effects in addition to the statistical errors from the method of LF estimation, such as cosmic variance, k -corrections, incompleteness and photometric system. Here, we have chosen to maximize our wavelength and redshift coverage by letting all available measurements contribute to our fitted evolution regardless of the error treatment. In the cases where the median redshift of the sample is not explicitly given, we have placed the measurements at the midpoint of the redshift bin. Our wavelength interval is sampled at the rest-frame bands shown in the panels of Figure 3.1 where most of the LFs have been measured. The offsets from these defined wavelengths due to filter variations (e.g. SDSS u' and Johnson U) are small enough to be neglected.

Motivated by the fitting formulae in Section 2.3, which we found to be reliable over a wide range of wavelengths, we consider the following three parameter fits for the evolution of the luminosity density

$$j_\nu(z) = a_\lambda(1 + (z - z_0))^{b_\lambda} \exp(-c_\lambda(z - z_0)) \quad (3.2)$$

where we fix $z_0 = 0.8$. Although not restricted to Schechter LFs, this functional form for $j_\nu(z)$ is nevertheless equivalent to the underlying Schechter parameters evolving as $L^* \propto (1 + (z - z_0))^{b_\lambda}$ and $\phi^* \propto \exp(-c_\lambda(z - z_0))$ with a constant faint-end slope. Interpolating the rest-frame data between our 18 reference bands defines the rest-frame emissivity spectrum at any given epoch. We apply a cutoff to the spectrum above the Lyman limit, $E_{\text{cutoff}} = 13.6\text{eV}$, corresponding to efficient absorption of

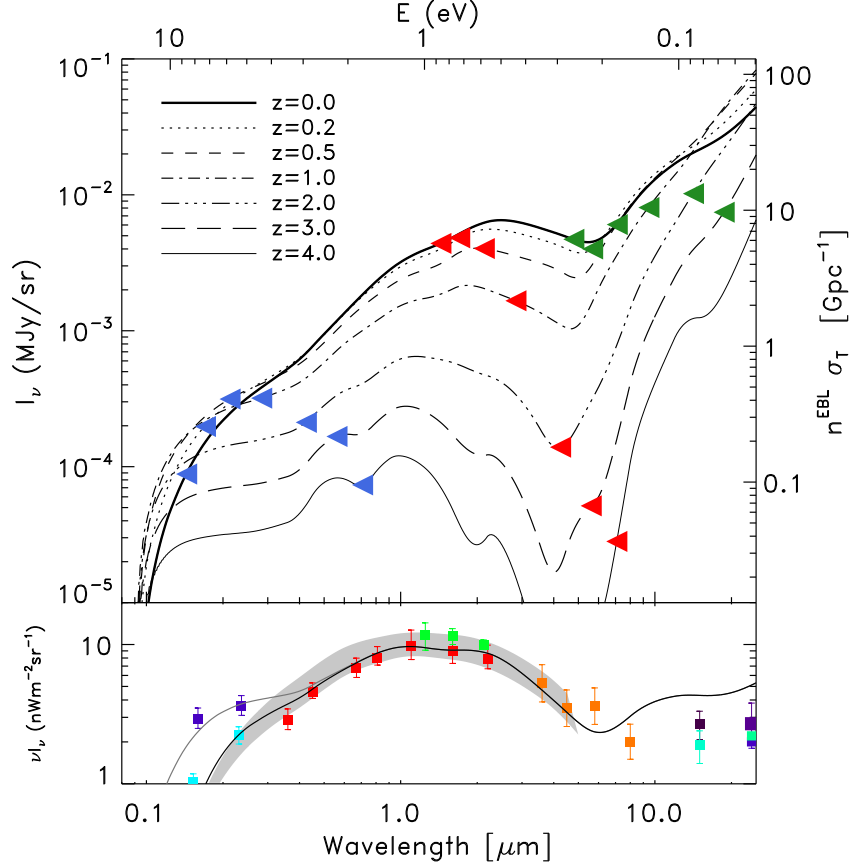


Figure 3.2 *Upper panel:* The evolving EBL resulting from our empirical reconstruction. The different lines illustrate the build-up of EBL with cosmic time leading to the present day levels (thick solid curve). We display the evolving EBL in comoving coordinates i.e. without the expansion factor $(1+z)^3$ for better mutual comparison. The left pointing triangles show the EBL threshold energy needed to interact with an observed 30GeV photon (blue), 300GeV, (red) and 1TeV (green) originating at the redshifts shown. *Lower:* Our reconstructed EBL compared to integrated counts in the literature along with the region bound by the upper/lower faint-end scenarios in Chapter 2 (shaded). The black and gray lines represent the case of $E_{\text{cutoff}} = 10.2\text{eV}$ and 13.6eV respectively. The counts data are from (190, purple), (191, cyan), (33, red), (146, green), (34, orange), (192, cyan), (193, black), (194, deep purple), (195, light green), (196, blue).

ionizing photons by hydrogen in the local environments. At all lower energies, the universe is assumed to be completely transparent to background photons. The integrated light from galaxies seen today can be calculated using Equation 1.14.

In Chapter 2 we considered two limiting cases for the evolution of the faint-end of the LF and showed that the distribution of galaxies from LF data, when projected onto the sky, accurately recovered the observed galaxy counts across the optical and near-infrared. The flux from the integrated counts is displayed as shaded regions in the lower panel of Figure 3.2 along with our empirically determined EBL (solid line) which is in good agreement with integrated counts data in the literature apart from wavelengths $\gtrsim 6\mu\text{m}$ where the steep evolution of the mid-IR LFs (8-24 μm) causes our EBL to be a factor of $\sim 2-3$ higher than integrated counts from references (196; 192; 194; 195). Although these authors do not claim to fully resolve the CIB at these wavelengths, the discrepancy is large enough to indicate a mismatch between number counts and mid-IR LF measurements at $z > 0.5$. This issue is apparently also encountered in galaxy evolution models; ref. (197) are not able to simultaneously account for the integrated counts and the bright-end of the observed LF in the 8-24 μm range using different dust templates. In fact, this is the wavelength regime where varying degrees of dust contribution and PAH emission make the spectrum less predictable. Recent upper limits derived from a TeV source spectra also favor low levels of CIB at these wavelengths (45; 44). At this stage, one must therefore question the robustness of EBL reconstructed from LFs at $\gtrsim 8\mu\text{m}$.

The UV/blue end of the EBL turns out to be sensitive to the abundance of photons with energies just below the Lyman limit, 13.6eV. The redshifted far-UV

contribution dominates the EBL below $0.5\mu\text{m}$ due to the steep increase of the star formation rate at earlier times. For all galaxy types, there is considerable absorption in the Lyman series which we do not account for and we illustrate this dependence by considering the case where Lyman-series absorption completely suppresses the spectrum above 10.2eV (instead of $E_{\text{cutoff}} = 13.6\text{eV}$); shown as gray lines in Figure 3.2 (lower panel). We subsequently display our optical depths for the both cases which bracket the true behavior.

3.3 The Photon-photon Optical Depth

The relevant quantity for computing the optical depth due to photon-photon interaction is the rest-frame number density of photons as a function of time and energy, $n(E, z)$. We shall refer to the energy of a photon belonging to the EBL as E and we use \mathcal{E} for the propagating γ -rays. Rest-frame quantities are denoted with a prime. At any given epoch, the photon number density (in proper coordinates) is composed both of sources emitting in the rest-frame as well as the accumulated emission from earlier times

$$n(E', z) = (1 + z)^3 \int_z^\infty \frac{j_{\nu'}(z')/h}{h\nu'} \frac{dt}{dz'} dz', \quad (3.3)$$

where h is the Planck constant (the extra h is to convert j_ν to per unit energy, $dE = h d\nu$) and $\nu' = (1 + z')/(1 + z)$. The condition for pair production is that the total energy in the center-of-mass frame must satisfy $\mathcal{E}'E'(1 - \cos\theta) \geq 2(m_e c^2)^2$ where θ is the angle of incidence. This means that in order to interact with a γ -ray of energy \mathcal{E}' , background photons must have wavelengths of $\lesssim 5.0(\mathcal{E}'/1 \text{ TeV})\mu\text{m}$.

The cross section for this interaction is

$$\sigma(E', \mathcal{E}', \mu) = \frac{3\sigma_T}{16}(1 - \beta^2) \left[2\beta(\beta^2 - 2) + (3 - \beta^4) \ln \left(\frac{1 + \beta}{1 - \beta} \right) \right], \quad (3.4)$$

where

$$\beta = \sqrt{1 - \frac{2m_e^2 c^4}{E' \mathcal{E}' (1 - \mu)}}, \quad \mu = \cos \theta.$$

For the most likely angle of incidence, $\mu = 0$ (side-on), the probability for interaction is maximized at roughly four times the minimum threshold energy, $\sim 4m_e c^2 / \mathcal{E}$. The optical depth encountered by a high energy photon originating at z ($\tau \sim \sigma n d$) can be expressed in terms of its observed energy, \mathcal{E} , as

$$\tau_{\gamma\gamma}(\mathcal{E}, z) = c \int_0^z \frac{dt}{dz'} dz' \int_{-1}^1 (1 - \mu) \frac{d\mu}{2} \int_{2m_e^2 c^4 / \mathcal{E}' (1 - \mu)}^\infty \sigma(E', \mathcal{E}', \mu) n(E', z') dE' \quad (3.5)$$

where $n(E, z)$ comes from Equation 3.3. In Figure 3.3 we display the calculated optical depths as a function of observed energy for γ -rays originating at several redshifts. The optical depth roughly traces the shape of the number density of EBL photons with a sharp drop in the optical depth at the lowest energies due to the cutoff at the Lyman limit. We also show the regions encompassed by the two scenarios of the faint-end evolution from the reconstruction in Chapter 2.

3.4 Application to High Energy Observations

What do these reconstructed opacities imply for observations of high-energy sources with the current instruments? Blazars and gamma-ray bursts (GRBs) are examples

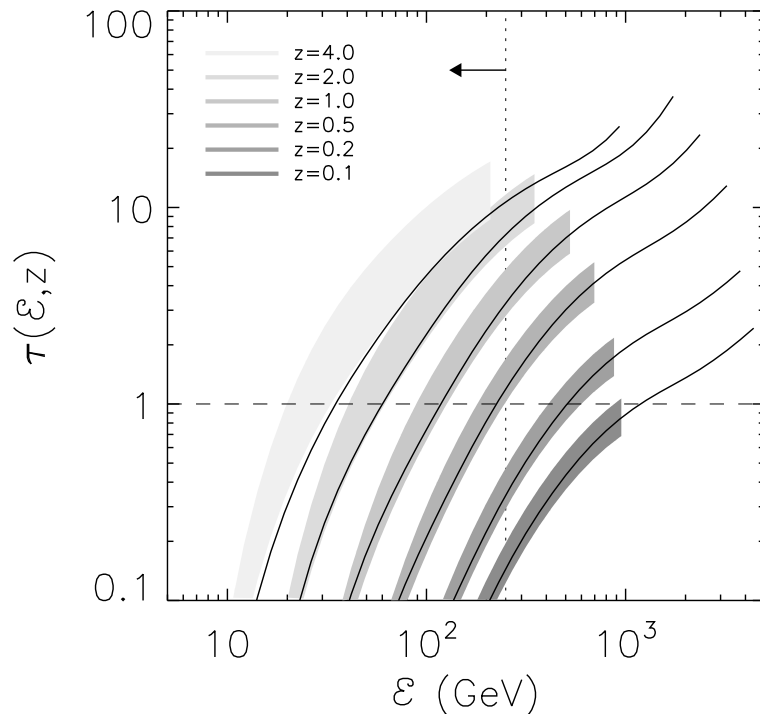


Figure 3.3 Solid lines show the $\gamma\gamma$ optical depth contributed by known galaxy populations assuming $E_{\text{cutoff}} = 13.6\text{eV}$ (gray curve in the lower panel of Figure 3.2). The curves are not drawn beyond the energy of $(m_e c^2)^2 / E_{24\mu\text{m}}(1+z)$ as we do not consider data at $\lambda > 25\mu\text{m}$. The shaded regions show the boundaries of the upper/lower scenarios in the empirical reconstruction in Chapter 2 out to $4.5\mu\text{m}$. The dotted vertical line shows roughly the highest energy probed by *Fermi*/LAT and the dashed line shows where $\tau = 1$ for reference.

of high energy extragalactic sources whose spectra is affected by attenuation of photons in excess of $\gtrsim 10\text{GeV}$. Two types of datasets are relevant for this discussion: space-borne *Fermi*/LAT measurements at $\lesssim 500\text{GeV}$ and ground-based telescopic measurements extending out to $\sim\text{TeV}$ energies. Because extragalactic γ -ray absorption increases with both with redshift and energy, the EBL can be constrained based on the highest energy photons observed from a source provided the redshift is known (198). GRBs have the advantages of being observable across great distances and typically displaying harder spectra than most blazars at sub-GeV energies. Figure 3.2 shows that for *Fermi*-observed sources it is sufficient to use data out to $\simeq 4.5\mu\text{m}$ (red symbols), whereas for TeV range observations, survey data are needed out to the longer wavelengths (green symbols). Figure 3.3 shows the reconstructed optical depth explicitly confirming this. We now briefly discuss the implications:

Fermi/LAT detects blazars and GRBs out to energies $\sim 250 - 300\text{ GeV}$. In Figure 3.4 (upper panel) we show curves of constant $\gamma\gamma$ optical depth in $\mathcal{E} - z$ space and compare with the most constraining high energy *Fermi*/LAT sources with known redshifts (taken from 198). The contours of $\tau = 1, 2, 3, 5$ correspond to probabilities of photon being absorbed by the EBL of 63%, 86%, 95%, 99.3%, respectively. In the absence of new populations, the universe remains fairly transparent at the *Fermi*/LAT energies out to $z \sim 2-3$. Our reconstructed EBL is fully consistent with all the available LAT data and, in fact, allows for non-negligible extra levels of the CIB from new populations such as possibly have existed at higher z . As the *Fermi* mission progresses and Figure 3.4 (upper) becomes more populated at the highest energies, sources at high- z will provide better constraints for the optical/NIR EBL.

Ground-based Cherenkov telescopes have produced good quality spectra for TeV-blazars, although for sources at significantly lower redshifts than *Fermi*/LAT. If the evolving EBL is known to a good accuracy, one can deabsorb observed blazar spectra to reveal the intrinsic component, which is expected to have a power-law form, $dN/dE \propto E^{-\Gamma}$. The lower panels in Figure 3.4 demonstrate how our reconstructed EBL affects the spectrum of two known blazars at relatively high redshifts, both of which have been used to place upper limits on the optical/NIR EBL. Good quality spectrum of the BL Lac object 1ES 1101-232 ($z = 0.186$) has been obtained by HESS in the energy range 0.16 – 3.3TeV which at $z = 0.186$ interacts most strongly with optical and near-IR background photons (42). The observed spectrum is relatively hard ($\Gamma = 2.88 \pm 0.17$) and results in a best-fit intrinsic photon index of $\Gamma_{\text{int}} = 1.49$ after deabsorption. For this particular source, the upturn at TeV energies is largely driven by the EBL photons at $\gtrsim 5\mu\text{m}$ and would be less pronounced if our EBL reflected the integrated counts data in the lower panel of Figure 3.2. Because the EBL changes with time in both shape and amplitude, the effects on γ -ray absorption become even more prominent for more distant sources. The spectrum of the distant radio quasar 3C 279 has been captured by MAGIC during different flaring events (200; 201). The deabsorbed spectrum of 3C 279 shown in Figure 3.4 (lower) also deviates substantially from a simple power-law in the highest energy bins which is unlikely to be due to our near-IR background being overestimated. This behavior of the deabsorbed 3C 279 spectrum has been pointed out by ref. (41) who suggest either improved emission models or instrumental systematic

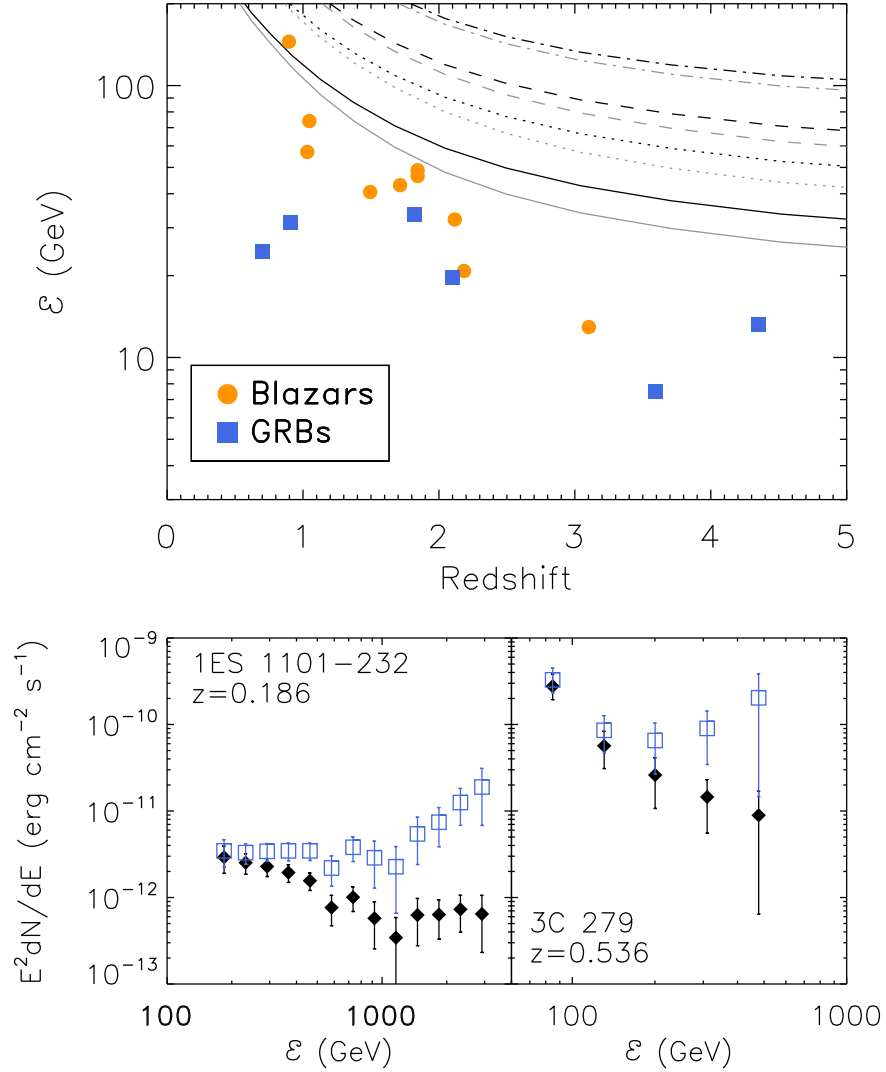


Figure 3.4 Upper: the curves show where a photon of energy \mathcal{E} originating at z , encounters exactly $\tau_{\gamma\gamma} = 1, 2, 3, 5$ (solid, dotted, dashed, dash-dotted respectively). Black and gray correspond to the cases of the rest-frame spectrum cutoff energy is at 10.2 and 13.6eV respectively. The symbols show the highest energy photon observed in GRBs (blue squares) and a selection of the most constraining of *Fermi*/LAT blazars (orange circles) (198; 199). Lower: the observed energy spectrum of the sources 1ES 1101-232 ($z = 0.186$; *left*) and 3C 279 ($z = 0.536$; *right*) shown with black diamonds, and the corresponding deabsorbed data as blue squares. The deabsorbed spectra have best-fit photon indices $\Gamma_{\text{in}} = 1.49$ and $\Gamma_{\text{in}} = 2.28$ respectively, but deviate substantially from a power-law at the highest energy bins.

uncertainties as potential solutions. Another possibility is that some fundamental effects are missing such as secondary γ -rays produced along the line of sight by cosmic rays accelerated by the blazar jet (50). In absence of such secondary effects however, the universe should be completely opaque for TeV sources at $z \gtrsim 0.5$.

Upper limits for the EBL derived from TeV spectra rely on assumptions of the hardness of the intrinsic blazar spectrum. Ref. (44) derives limits for the whole range of optical to far-IR EBL using an extensive source sample from both *Fermi*/LAT and ground-based Cherenkov telescopes. Their results allow a total integrated NIR flux (1-10 μ m) of $\sim 20 \text{ nW m}^{-2} \text{ sr}^{-1}$ in excess of known galaxy populations whereas there is, at most, little room for extra contribution in the mid-IR ($> 10 \mu\text{m}$). In fact, our LF-derived EBL is inconsistent with the lowest mid-IR limits (45).

3.5 Discussion

We have shown that it is possible to robustly reconstruct the evolving EBL in the universe using library of multiwavelength survey data. This reconstruction uniquely defines the γ -ray opacity out to TeV energies for sources at $z \lesssim 4$ and shows that at the energy bands probed by *Fermi*/LAT, the universe is fairly transparent out to $z \sim 2 - 3$, unless unknown sources at high redshifts contribute non-negligible amounts of CIB. Our reconstructed EBL is consistent with the γ -ray horizon that has been detected at low/intermediate- z (47; 48). At TeV energies, probed by ground based telescopes, the universe becomes optically thick at $z \sim 0.5$ so any such photons associated with the sources at higher redshifts would have to be of

secondary origin.

Unlike ground-based Cherenkov telescopes, the LAT ($\lesssim 500$ GeV) is particularly suitable for probing the CIB excess from early populations. There are several reasons for this: 1) the onset of γ -ray absorption occurs at lower energies for sources at higher z , where LAT is more sensitive; 2) the $\gamma\gamma$ -optical depth depends on the proper photon number density, $\propto(1+z)^3$, which at high- z becomes large even for low CIB excess levels; 3) any CIB already in place since the era of the first stars can be more readily discerned at higher- z in the absence of contamination from the bright galaxy populations of later times. Isolating CIB emissions from early epochs is therefore optimally probed with $\gtrsim 10$ GeV photons originating at $z > 1$. This may be possible with the recently released *The First LAT Catalog of High Energy Sources* (1FHL) (202). The 1FHL contains 47 blazars with measured redshifts above $z = 1$ (39 FSRQs, 8 BL Lacs) out of which 35 are significantly detected above 30 GeV.

Chapter 4: X-ray Emission from the CIB Sources: The Origin of the CIB×CXB Signal

4.1 Overview

The large scale clustering of the source-subtracted CIB fluctuations does not provide direct information on whether the underlying sources are powered by stellar nucleosynthesis or accretion onto compact objects. Recently, Cappelluti et al. 2013 (77, C13 hereafter) provided observational evidence for a substantial population of accreting objects among the CIB sources. C13 used deep source-subtracted *Spitzer*/IRAC and Chandra maps of an overlapping region on the sky to reveal a highly significant cross-correlation signal between the unresolved CIB at 3.6,4.5 μ m and the soft 0.5-2 keV CXB. If this signal originates at high- z , it may have important implications for galaxy formation, the growth of early black holes and reionization. However, since there are a variety of ways in which X-ray production can spatially correlate with optical/IR emitting counterparts, a more quantitative analysis of known source classes at $z \lesssim 6$ is needed; such as X-ray binaries, AGN and hot gas.

The deepest Chandra surveys have been able to resolve $\sim 80-90\%$ of the [0.5-8] keV CXB into individual point sources, the majority of which is made up of AGN

(203; 204). However, at the faintest fluxes, the abundance of sources identified as normal galaxies rapidly approaches that of AGN and is likely to dominate at fainter levels. The X-ray emission within galaxies comes predominantly from X-ray binaries (XRBs), a compact object accreting from a companion star, which have been found to scale well with galaxy properties such as star formation rate and stellar mass (e.g. 205; 206; 207). These sources have recently been detected out to deeper levels, and higher redshifts, by stacking analyses (208; 209). The bulk of the unresolved CXB fluctuations ($\gtrsim 2 \times 10^{-16} \text{erg s}^{-1} \text{cm}^{-2}$) remaining in deep Chandra exposures has been assigned to gas residing in galaxy groups and clusters ($\sim 50\%$), with the rest being contributed by AGN and galaxies (210). At these levels, any contribution from high- z miniquasars would be overwhelmed by these low- z components ($< 5\%$), although the systematic uncertainty in the mean level of the CXB increases such constraints by a large factor. The signal measured in C13 is revealed only after eliminating undetected X-ray sources down to unprecedented flux levels, $\ll 5 \times 10^{-17} \text{erg s}^{-1} \text{cm}^{-2}$, using the deep source-subtracted *Spitzer* maps.

In this Chapter, we explore the contribution of the intermediate redshift sources to the measured level of the CIB \times CXB coherence (C13) by modeling components from different source classes: galaxies, AGN and diffuse emission, in both IR and X-rays. We present a formalism for reconstructing the cross power spectrum of the fluctuations produced by each source class using the latest observational evidence for their clustering and abundance. We also discuss the intrahalo light model of ref. (67) in light of the full CIB constraints and its measured coherence with the unresolved CXB.

4.2 The Measured CIB×CXB Coherence

The cross-power describing the correlations between fluctuations at different wavelengths (m, n) is $P_{mn}(q) = \langle \Delta_m(q)\Delta_n^*(q) \rangle = \mathcal{R}_m(q)\mathcal{R}_n(q) + \mathcal{I}_m(q)\mathcal{I}_n(q)$ with \mathcal{R}, \mathcal{I} standing for the real, imaginary parts of the Fourier transform, $\Delta(\vec{q})$. The cross-power spectrum is a real quantity which can assume positive or negative values. Coherence is then defined in its usual way as $\mathcal{C}(q) \equiv \frac{[P_{mn}(q)]^2}{P_m(q)P_n(q)}$ (66). In the absence of common (coherent) populations at wavelengths m and n the cross-power, measured from a map of N_{pix} pixels, will oscillate around zero with a random statistically uncertainty of order $[P_m P_n]/\sqrt{N_{\text{pix}}}$.

The spatial coherence measured between the source-subtracted CIB fluctuations and the unresolved CXB used data from the deep Chandra ACIS-I AEGIS-XD survey and The *Spitzer* Extended Deep Survey (SEDS) in the EGS field, where the two datasets overlap in a $\simeq 8' \times 45'$ region of the sky (for details, see 77). The measured cross-power between the source-subtracted IRAC maps at $(3.6, 4.5)\mu\text{m}$ and Chandra $[0.5-2]$ keV maps was detected, at angular scales $10''-1000''$, with an overall significance of $\simeq(3.8, 5.6)\sigma$ respectively. At the same time, no significant signal was detected between the IRAC source-subtracted maps and the harder Chandra bands. The measured coherence signal has been detected after jointly masking resolved sources down to $m_{\text{AB}} \simeq 25$ and $7 \times 10^{-17} \text{erg s}^{-1} \text{cm}^{-2}$ in IR and X-rays respectively¹. The signal is characterized by the cross-power spectrum, $P_{\text{IR,X}}(q)$ shown

¹Throughout, all quantities referred to as “X-ray” or denoted by “X” correspond to the emission in the soft X-ray band 0.5-2 keV, unless noted otherwise. The suffix IR refers to the near-IR wavelengths $3.6\mu\text{m}$ and $4.5\mu\text{m}$ i.e. the effective wavelengths of *Spitzer*/IRAC bandpasses 1 and 2 whereas FIR refers to the total infrared quantities, integrated over $10-1000\mu\text{m}$.

in Figure 4.10, and exhibits a broad band averaged cross-power in the 10–1000'' angular range

$$\langle P_{3.6\mu\text{m},0.5-2\text{keV}} \rangle = 6.4 \pm 1.7,$$

$$\langle P_{4.5\mu\text{m},0.5-2\text{keV}} \rangle = 7.3 \pm 1.3,$$

in units of $10^{-20} \text{erg s}^{-1} \text{cm}^{-2} \text{nWm}^{-2} \text{sr}^{-1}$. We refer to the opposite ends of the measured angular interval [10'',1000''] as small and large angular scales respectively.

In this Chapter we examine the contribution to this signal from extragalactic populations at $z \lesssim 6$ i.e. excluding the putative high- z populations. We decompose the total cross-power spectrum of the fluctuations into the sum of power from sources of types known to emit both in X-rays and optical/IR

$$P_{\text{total}} = P_{\text{galaxies}} + P_{\text{AGN}} + P_{\text{diffuse}} \quad (4.1)$$

with each of these components contributing both in terms of their large scale clustering on the sky as well as shot noise dominating small scale power. We refer to sources of X-ray emission arising collectively from stars, stellar remnants and gas within galaxies as “normal galaxies” whereas the term “AGN” is used in its broadest sense referring to any black hole activity in the centers of galaxies regardless of subclasses. We also consider non-point sources such as hot diffuse gas and dispersed light around galaxies which we collectively refer to as “diffuse” components.

The measured coherence can be interpreted as the product of the fraction of

the emission due to common populations i.e. $\mathcal{C} = \zeta_m^2 \zeta_n^2$, where ζ_m is the fraction contributed by the common populations in band m . At large angular scales ($>20''$) the level of the measured coherence between $4.5\mu\text{m}$ and $[0.5-2]$ keV is measured to be $\mathcal{C}(q) \sim 0.03 - 0.05$ implying that at least 15–25% of the large scale power of the CIB fluctuations is correlated with the spatial power spectrum of the X-ray fluctuations, i.e. $\sqrt{\mathcal{C}} \gtrsim 15\text{--}25\%$. This implies that the true nature of the signal lies somewhere in between two limiting scenarios

- (1) 100% of the large scale CIB fluctuations are contributed by common X-ray sources, that make up $\sim 15\text{--}25\%$ of CXB fluctuations,
- (2) $\sim 15\text{--}25\%$ of the large scale CIB fluctuations are contributed by common X-ray sources, that make up 100% of CXB fluctuations.

Note however, that $\sqrt{\mathcal{C}(q)}$ is a scale dependent value. It is important to stress that the term “common sources” does not necessarily imply that the corresponding parts of the CIB and CXB are produced by the same physical sources emitting at both IR and X-rays. The IR and X-ray emitters may simply be separated by an angle smaller than the Chandra Gaussian beam of $\simeq 10''$ corresponding to a physical scale of $\sim 0.1h^{-1}\text{Mpc}$ at $z = 1$. This defines the scale of the individual “objects” in the analysis that follows.

C13 also note that the unresolved CXB fluctuations may be contaminated by ionized gas in the Milky Way. Unfortunately, this component is difficult to model and subtract but it is not expected to exhibit positive cross-correlation with the Galactic cirrus and should rather anti-correlate with infrared emitting dust clouds.

Therefore the observed X-ray fluctuations are an *upper* limit for the extragalactic CXB component and its coherence with the CIB, quoted at $\mathcal{C} \sim (0.2)^2$, should be considered a *lower* limit.

4.3 Sources of the CIB

The CIB levels from undetected populations implied by the source-subtracted fluctuations require $\gtrsim 0.5 \text{ nW m}^{-2}\text{sr}^{-1}$ (69) on top of the extrapolated flux from known galaxies (146; 35). This level of CIB is therefore easily accommodated by both direct and indirect measurements but the sources of this component have not been conclusively identified. However, valuable insight can be obtained from population studies and deep observations at other wavelengths.

4.3.1 Galaxies

According to the analysis in Chapter 2, extrapolation of faint galaxy populations suggests an unresolved CIB of $\sim 0.1\text{--}0.3 \text{ nW m}^{-2}\text{sr}^{-1}$ at $3.6\mu\text{m}$ which is mostly produced in the $1 < z < 4$ range (73). The large scale clustering of these populations, $\delta F/F \lesssim 0.05$, was found to be insufficient to account for the observed CIB fluctuations at large scales (see Figure 4.6). However, provided that unresolved galaxies dominate the unresolved CXB fluctuations, they could in principle produce enough coherence with the CXB to reach $\mathcal{C} \sim 0.02 - 0.05$ while remaining a underdominant component in the CIB fluctuations. Here we use the empirical calculation from Chapter 2 where the CIB from galaxy populations was reconstructed using

233 observed multiwavelength luminosity functions measured at $z \lesssim 5$. We address the X-ray emission from these galaxies in Section 4.4.1.

4.3.2 AGN

The AGN fraction of the resolved CIB sources is small, $\lesssim 8\text{--}10\%$ (211), but their leading role for the CXB energetics makes them important for the interpretation of the CIB \times CXB correlation. Here we estimate the CIB production from AGN by constructing an AGN population model from measured J-band luminosity functions (212). This sample consists of 1838 AGN (Type 1 and 2) at $0 < z \lesssim 6$ selected in both IR and X-ray, and is therefore less affected by incompleteness and biases seen in purely optical or infrared selected samples. The choice of rest-frame J-band ($1.25\mu\text{m}$) luminosity functions minimizes the uncertainty in the k-correction as distant populations observed at $3.6\text{--}4.5\mu\text{m}$ emit light at rest-frames $0.7 \lesssim \lambda \lesssim 4.5\mu\text{m}$ for $z < 4$. We use the pure luminosity evolution parameterization of the AGN LF given in ref. (212) which includes both host galaxy emission and reddening, extrapolating the parameterized evolution beyond $z > 5$ (assuming LDDE model instead does not affect our results). The inclusion of the host galaxy is important since the X-ray faint AGN tend to be optically obscured and dominated by their host galaxy light which also contributes to the CIB. At every distance the $1.25\mu\text{m}$ emission is corrected to $\lambda_{\text{em}} = \lambda_{\text{obs}} / (1+z)$ using the average low resolution AGN spectral template of ref. (213) where λ_{obs} is either 3.6 and $4.5\mu\text{m}$ for this paper (see also ref. 214). Figure 4.1 shows a reasonable agreement between this projected population and

Spitzer/IRAC AGN counts from ref. (211). Inaccuracies in the shape of the counts may arise from the fact that our mean AGN spectrum is corrected for host galaxy contribution and reddening.

The typical faint-end slope measured for AGN luminosity functions ranges from -1.6 to -1.3 showing marginal evidence for flattening at higher redshifts (215; 216). In our model, we conservatively extrapolate a non-evolving faint-end slope of $\beta = -1.4$ to account for unresolved AGN but this likely *overestimates* the AGN contribution for several reasons. First, because we use LFs uncorrected for host galaxy contribution which bias the faint-end slope and increase the number of faint objects (217). This effect can be particularly pronounced in the near-IR, as the ratio of host to AGN in unobscured objects has a typical maximum at $1.6\mu\text{m}$. Second, the $0.5\text{-}2\text{ keV}$ vs $3.6\mu\text{m}$ flux ratio turns towards $X/O < 0$ at faint fluxes suggesting a decreasing importance of AGN contribution (218). This is consistent with significant number of optically normal galaxies that are seen as hosts of low-luminosity X-ray AGN, (e.g. 219). Diminishing nuclear activity makes the host galaxy dominate at low luminosities and the distinction between galaxy and AGN becomes less meaningful. Then these sources should be largely accounted for by our treatment of IR galaxies. In addition, our treatment of normal galaxies (see Section 4.3.1) is based on a compilation of observed galaxy LFs which do not typically exclude AGN.

From Figure 4.1, it is clear that normal galaxies are far more numerous than AGN at all flux limits regardless of the extrapolation to faint levels. The CIB contribution of AGN is always $\lesssim 10\%$ of the galaxy contribution and their sky

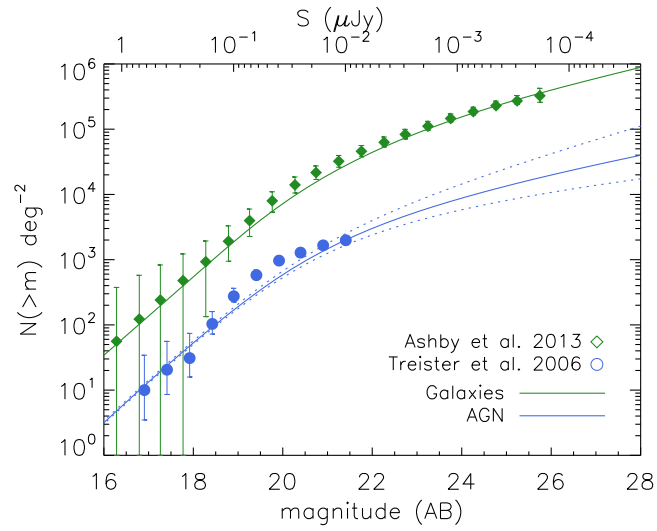


Figure 4.1 The cumulative source number counts of galaxies (green line) compared with AGN (blue line). The models for AGN are constructed from J-band LFs and are uncorrected for host galaxy contribution (explained in the text). Corresponding AGN counts data is from ref. (211) (circles). The dotted lines show the cases in which the faint-end slope of the AGN LF is extrapolated with a constant slope of -1.6 (upper) and -1.2 (lower). The green line shows the galaxy reconstruction of ref. (73) compared with SEDS data (35) (diamonds).

surface density is $\sim 2-3$ orders of magnitude smaller than the $\sim 1 \text{ arcsec}^{-2}$ required to explain the measured CIB fluctuations (69). AGN would need to live in low mass halos to exist in sufficient numbers at $z \lesssim 4$ and our mask eliminates most halos $\gtrsim 10^{12} M_{\odot}$ where AGN are typically found. Furthermore, a recognizable signature of faint AGN is that their near-IR spectrum should increase with wavelength due to their dusty torus emission but this is inconsistent with the blue colors of the measured CIB fluctuations (65). We therefore assert that the IR emission from AGN themselves is insufficient to produce significant unresolved CIB fluctuations. However, this does not necessarily eliminate AGN as sources of the CIB \times CXB correlation as their X-ray emission can produce stronger correlation with other IR populations sharing common large scale structures (see Section 4.6).

4.3.3 Diffuse emission, intrahalo light

Recently, some modeling of the origin of the CIB fluctuations has focused on a form of “missing light” associated with galaxy populations but distributed in diffuse structures around masked sources. There are several empirical lines of observational evidence that argue strongly against such an origin:

1. There are no spatial correlations between the source-subtracted *Spitzer*/IRAC maps and galaxies detected in deep Hubble/ACS maps ($0.5-0.9 \mu\text{m}$) $\lesssim 28$ mag (76). However, there are very significant correlations between the ACS galaxies and the unmasked *Spitzer* maps. This means that ACS galaxies and any associated diffuse emission, cannot contribute significantly to the large scale

CIB fluctuations found in source-subtracted *Spitzer* data.

2. The large scale CIB fluctuations are not sensitive to increasing/decreasing the size of masked regions around resolved galaxies. Indeed, Fig. 17 of ref. (78) shows that there is little variation in the CIB fluctuation as the source masking is eroded or dilated to masking fractions varying from $\simeq 7\%$ to $\simeq 46\%$.
3. There are no correlations between the source-subtracted CIB fluctuations and the identified removed extended sources. Moreover, ref. (78) constructed artificial halos around masked sources and demonstrated that the diffuse emission in the final image does not correlate spatially with the halos around masked sources that mimic missing light (54) and ref. (78).

These arguments contradict scenarios invoking any form of “missing light” associated with masked galaxies.

One such scenario was proposed by ref. (67) who considered diffuse starlight scattered around and between galaxies at $z \sim 1 - 4$ as an alternative explanation for the origin of the unresolved CIB fluctuations. This can arise from stars stripped in mergers or ejected via other processes. Here we consider such a diffuse component following definitions in ref. (67) deriving the CIB production history as

$$\frac{dF_{\text{IHL}}}{dz} = \frac{c}{4\pi} \int_{M_{\text{min}}}^{M_{\text{max}}} L_{\text{IHL},\lambda'}(M, z) \frac{dn}{dM} dM \frac{dt}{dz} (1+z)^{-1} \quad (4.2)$$

where $\lambda' = \lambda_{\text{obs}}(1+z)$ using a spectral template of a typical elliptical galaxy containing old stellar populations from Starburst99 (220). This template assumes a 900

Myr old stellar population forming at the same time with a Salpeter IMF ($1-100M_{\odot}$) and metallicity $Z = 0.008Z_{\odot}$. In Figure 4.4 we show that different choices of SED parameters do not affect the IHL flux to a great extent (unless the population is very young <20 Myr). In all other respects we follow the formulation in ref. (67) recovering a flux of $1 \text{ nW m}^{-2}\text{sr}^{-1}$ at $3.6\mu\text{m}$ which is consistent with but slightly higher than the $0.75 \text{ nW m}^{-2}\text{sr}^{-1}$ quoted in ref. (67). We are unable to get the large scale clustering up to the quoted $\delta F/F = 10 - 15\%$ and as a result our large scale fluctuations are a factor of $\sim 2-3$ lower (see Figure 4.6). As is shown in Figure 4.4, the CIB from this IHL component *exceeds* the *total* CIB from all galaxies already at $z \gtrsim 2$ according to the empirical reconstruction of Chapter 2. Although this by itself makes the model non-viable, we calculate the coherence levels between CIB and diffuse X-ray emission for this component.

4.4 Sources of the CXB

4.4.1 Normal X-ray Galaxies

The bulk of the CXB ($\sim 80 - 90\%$) has been resolved into point sources, most of which is contributed by AGN (203; 204). However, the number counts from the Chandra deep fields reveal that the contribution of normal galaxies (mostly XRBs) approaches that of AGN at the faintest levels (221; 204). A simple extrapolation of the slope of galaxies implies that they will ultimately dominate AGN at $\lesssim 10^{-17} \text{ erg s}^{-1}\text{cm}^{-2}$ (see Fig. 4.5); this is in fact suggested by deep stacking analyses (208). Although ref. (73) demonstrated the low contribution of known galaxy

populations to the unresolved CIB, their CXB×CIB amplitude ultimately depends on their X-ray properties.

The X-ray galaxy luminosity function (XLF) derived from *Chandra* and *XMM-Newton* data is limited to small samples of local galaxies of $L_X \gtrsim 10^{40}$ erg/s with luminosity evolution consistent with $L^* \propto (1+z)^{2.3}$ out to $z \sim 1$ (222; 223). The X-ray emission in galaxies is dominated by a population of compact objects accreting from a stellar companion although hot gas can contribute substantially to the soft X-ray flux ($\lesssim 1$ keV). To gain a better understanding of the X-ray galaxy population and its evolution a popular approach takes advantage of empirical correlations of X-ray luminosity with various galaxy properties derived from longer wavelength data. The XLF can be related to LFs measured at other wavelengths following ref. (224)

$$\Phi(\log L_X) = \int_{-\infty}^{\infty} \Phi(\log L_Y) P(\log L_X | \log L_Y) d \log L_Y \quad (4.3)$$

(in $\text{num} \cdot \text{Mpc}^{-3} \text{dex}^{-1}$) where Y represents a rest-frame band which correlates with X-ray luminosity via some specified L_X - L_Y relation and $P(\log L_X | \log L_Y)$ describes the probability of a source of L_Y having an X-ray luminosity of L_X . Here we assume the probability distribution to be Gaussian

$$P(\log L_X | \log L_Y) = \frac{1}{\sqrt{2\pi}\sigma} \exp \left[-\frac{(\log L_X(L_Y) - \log L_X)^2}{2\sigma^2} \right] \quad (4.4)$$

where $L_X(L_Y)$ is the X-ray luminosity predicted by a L_X - L_Y relation and σ is the standard deviation of the scatter in the measured correlation.

We consider the X-ray luminosity of normal galaxies to be the sum of contributions from HMXBs, LMXBs and hot gas

$$L_X^{\text{gal}} = L_X(\text{HMXB}) + L_X(\text{LMXB}) + L_X(\text{gas}) \quad (4.5)$$

Other forms of galaxy-wide X-ray emission, such as from WD binaries and supernova remnants, have been found to be at least ten times weaker so we ignore their contribution (225). A strong correlation is found between the star formation rate (SFR) and the overall X-ray emission of the galaxy which is attributed to active star forming regions producing bright short-lived ($\lesssim 100$ Myr) high mass X-ray binaries (HMXBs). On the other hand, long-lived ($\gtrsim 1$ Gyr) low mass X-ray binaries (LMXBs) have been found to correlate well with the net stellar mass in galaxies. For a full census of X-ray galaxies and their different emission mechanism, it is therefore helpful to decompose the population into late(active) and early(quiescent)-type galaxies, $\Phi^{\text{tot}} = \Phi^{\text{late}} + \Phi^{\text{early}}$. In the picture that follows, late-types can be assumed to contain HMXBs, LMXBs as well as hot gas whereas early-types only contain LMXBs and hot gas.

4.4.1.1 Late-types

The tight correlation between X-ray luminosity and SFR has established HMXBs as the dominant mechanism for X-ray production in late-type galaxies (e.g. 205). For the purpose of re-constructing the evolving population of X-ray galaxies, we rely

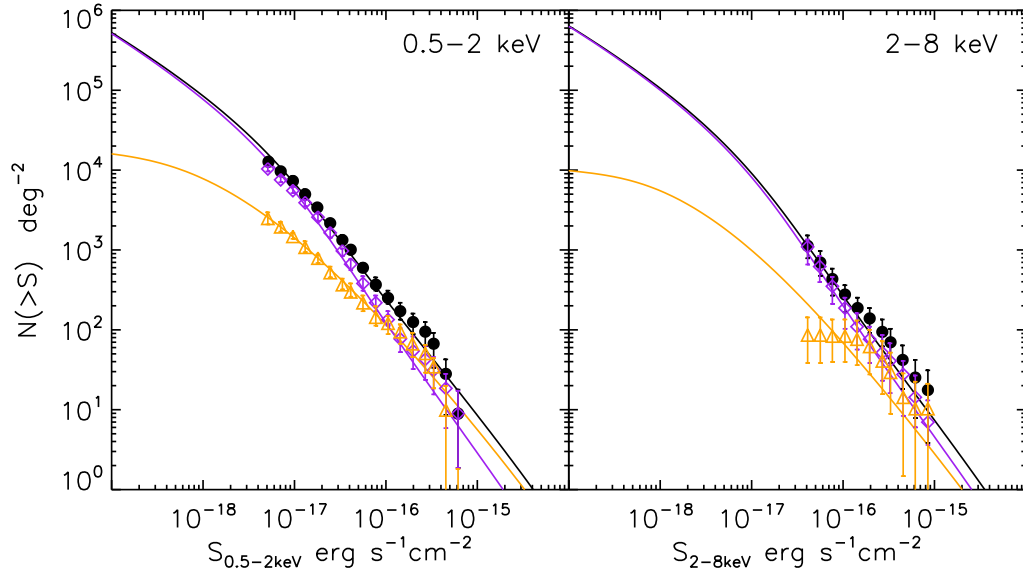


Figure 4.2 Cumulative X-ray source counts in soft (left) and hard (right) X-ray bands. The panels show observed galaxy counts from the CDF-S 4Ms survey (204) where the black circles represent all galaxies and the sub-contributions from late and early-type galaxies are shown as purple diamonds and orange triangles respectively. The solid lines show the prediction of our population model in the same colors scheme (black, purple and orange for total, late and early-types respectively). We show the extrapolation all the way down to $10^{-19}\text{erg s}^{-1}\text{cm}^{-2}$ to emphasize the expected behavior in the unresolved CXB regime.

on the total infrared luminosity function (8-1000 μm)². This choice is motivated by several points, 1) re-radiated dust emission in the FIR is an established tracer of star formation which bypasses uncertainties in UV tracers due to obscuration, 2) the L_X - L_{FIR} correlation is both very significant and well calibrated, 3) the evolution of the FIR LF has been probed out to $z \sim 3$ allowing the estimation of HMXB activity for 4/5 of the cosmic time. Since the bulk galaxy-contributed CXB comes from $z \lesssim 3$ it is not necessary to rely on UV LFs probing $z > 3$. We adopt the FIR LF measured from deep *Spitzer* GOODS/FIDEL data in the $0 < z < 2.5$ range (226; 91). The measurement is in good agreement with other FIR LFs in the literature (227; 228) and is described by a double power-law parameterized by the characteristic luminosity L^* , normalization ϕ^* , and bright and faint-end slopes α and β . The evolution is consistent with pure luminosity evolution $L^* \propto (1+z)^{3.6}$ out to $z = 1$ with very mild evolution of both L^* and ϕ^* at $z > 1$. Beyond $z = 3$ we assume L^* gets fainter with z at the rate implied by the UV LF of ref. (101) but this has little impact on our results.

The L_X -SFR relation was studied by (207) for galaxies covering roughly four orders of magnitude in SFR, $-1.5 \lesssim \log \text{SFR} \lesssim 2.5$ in M_\odot/yr . The relation is derived at 2–10 keV where hot gas becomes negligible and the emission is predominantly

²We denote the total infrared (8-1000 μm) as “FIR” to avoid confusing with “IR” which we use to refer to the near-IR

driven by HMXBs and LMXBs. They find a local best fit to be

$$\log L_{2-10\text{keV}} = \begin{cases} 0.94 \log L_{\text{FIR}} + 30.17, & \log L_{\text{FIR}} \lesssim 9.6 \\ 0.74 \log L_{\text{FIR}} + 32.09, & \log L_{\text{FIR}} \gtrsim 9.6 \end{cases} \quad (4.6)$$

with a 1σ scatter of roughly 0.4 dex. It is important to note that because ref. (207) derive the SFR solely based on IR luminosity our model does not depend on a L_{FIR} -SFR calibration. The duality of the relationship in Equation 4.6 over a wide range of SFR (0.01 - $100 M_{\odot}/\text{yr}$) arises because LMXBs provide a non-negligible contribution to the low SFR regime. Indeed, the K-band luminosity is used to trace stellar mass leading to a relationship $M^* \propto \text{SFR}^{1.1}$ for $\text{SFR} \lesssim 5 M_{\odot}/\text{yr}$ and $M^* \propto \text{SFR}^{0.3}$ for $\text{SFR} \gtrsim 5 M_{\odot}/\text{yr}$ which combines SFR and M^* in a more physically justified relation $L_X = \alpha M^* + \beta \text{SFR}$. Our adopted relation (Eqn 4.6) therefore accounts for both the HMXBs and LMXBs contribution in late-type galaxies. We assume an average spectral index of $\Gamma=1.8$ to convert to the 0.5-2 keV band.

Recent evidence seems to indicate that the local L_X -SFR relation is not constant with redshift. Ref. (209) find an evolution $L_X \propto (1+z)^{0.9}$ for galaxies with $\text{SFR} \gtrsim 5 M_{\odot}/\text{yr}$. However, including this evolution in our relation slightly overproduces the faintest CDFS counts (204). We therefore include a term of $\log L_X \propto 0.5(1+z)$ in Equation 4.6 which results in good agreement with the data. If we use the observed evolution regardless (overproducing faint X-ray galaxies) this gives a CIB \times CXB signal which is within a factor of 1.5 larger but our final conclusions are unchanged.

4.4.1.2 Early-types

The X-ray emission from quiescent galaxies is thought to be dominated by long-lived LMXBs leftover from earlier episodes of star formation and hot gas in extended halos. The X-ray luminosity of early-types is found to correlate well with K-band luminosity, the preferred indicator of stellar mass. For the template LF for early-type galaxies we have chosen the local K-band LF of ref. (121) (2MASS) for $z < 0.05$ and the evolving LF ref. (123) from combined SWIRE-VVDS-CFHTLS data reaching $z = 2$. These measurements separate the contribution from the early-types and late-type to the total LF. The bright(high mass)-end of the LF (stellar mass function) is dominated by early-types whereas late-types are much more numerous at the faint(low mass)-end. All the K-band LFs are well described by the Schechter function with parameters L^*, ϕ^* and α measured out to $z=2$. We fit the evolving parameters in the $0 < z < 2$ range using the functional forms in ref. (73) and extrapolate them beyond $z > 2$.

Ref. (225) studied the distinct components of X-ray emission in nearby early-types in great detail, resolving the individual XRBs. The total LMXB luminosity is found to correlate with K-band luminosity via the relation

$$\log L_{0.3-8keV} = \log L_K + 29 \quad (4.7)$$

where L_K is in $L_{\odot,K} = 4.82 \times 10^{32} \text{erg}\cdot\text{s}^{-1}$ and the 1σ scatter is ≈ 0.3 dex. We convert the 0.3-8 keV luminosity to the 0.5-2 keV band assuming a spectral index of $\Gamma=1.8$.

4.4.1.3 Hot gas

It is well known that galaxies contain extended hot halos of gas heated to the virial temperature emitting in lines and thermal continuum. We find that a luminosity comparable to that of XRBs is needed from hot gas in early types to account for the number of bright 0.5-2 keV sources (Fig. 4.2) whereas XRBs are sufficient to explain the entire late-type population. This is consistent with the fact that hot gas in early-types is found to constitute a much greater fraction of the total L_X than in late-types (229). The unresolved CXB, however, cannot contain significant contributions from hot gas for several reasons. First, groups and clusters close by with $kT > 1$ keV are easily detected and removed in the Chandra maps and the joint IR/X-ray mask used in C13 further eliminates galaxies residing in $\gtrsim 10^{12} M_\odot$ (~ 0.1 keV) halos out to $z \sim 2$ where high-mass systems become increasingly rare. Second, normal galaxies have characteristic temperatures of < 1 keV where their spectrum decreases exponentially. At $z > 1$, their contribution quickly redshifts out of the 0.5-2 keV band. Both of these considerations act to reduce hot gas contribution in the faint unresolved regime which is dominated by low-mass systems at increasingly high redshifts.

To demonstrate this, we use the hot gas properties predicted in publicly available semi-analytic models mapped onto the Millennium simulations (82). The hot gas mass is calculated based on the baryon content, cooling and infall rate onto the halo. We assume a density profile $\propto (1 + (r/r_0)^2)^{-3\beta/2}$ with a constant $r_0 = R_{\text{vir}}/10$ and $\beta = 2/3$ and apply k-corrections assuming a thermal continuum spectrum

$\propto T_{\text{vir}}^{-1/2} \exp(-E/kT_{\text{vir}})$ (229). In this description, the observed [0.5-2 keV] counts are reproduced when all systems with masses below $10^{13}M_{\odot}$ are included, which is roughly the mass scale of the the most massive galaxies. However, the hot gas counts flatten towards lower fluxes where are dominated by the HMXB component. This is shown as red dotted line in Figure 4.5. In Section 4.4.3 we consider diffuse X-ray emission in more complex environments such as groups and filaments, including the warm-hot intergalactic medium (WHIM).

4.4.1.4 The unresolved CXB from galaxies

We now have constructed the evolving XLF, $\Phi(L_X, z)$, for normal galaxies based on Equation 4.3 and L_X -relations for both late- and early type galaxies. The source density on the sky can then be obtained via projection (Equation 1.17). For a power-law spectrum, $E^{-\Gamma}$, with a spectral index Γ , the k -correction becomes $(1+z)^{2-\Gamma}$. The power-law slope of X-ray galaxy spectra has been found to lie in the $1 < \Gamma < 3$ range with a mean of ≈ 1.8 which is what we assume for the HMXB and LMXB contribution. For the hot gas component we k -correct using a thermal continuum spectrum, $\propto T^{-0.5} \exp(-E/kT)$.

Figure 4.2 shows the predicted cumulative X-ray counts of our galaxy population models and compares them with the observed deep CDFS counts showing both the early and late-type contribution. The bright counts rise with a near-Euclidian slope and start turning over towards the faint regime as expected from both the LF turnover and cosmic expansion. At the flux limit of today's deepest measurements,

$\sim 10^{-17} \text{erg s}^{-1} \text{cm}^{-2}$, the source counts are dominated by L_{FIR}^* galaxies (at the knee of the LF) gradually turning over to the faint-end regime which only becomes relevant at much fainter levels ($\lesssim 10^{-19} \text{erg s}^{-1} \text{cm}^{-2}$). As long as the flux converges, the unresolved CXB fluctuations are not very sensitive to the faint-end slope of the XLF.

The spatial CIB \times CXB correlation signal is detected by C13 after masking sources resolved in both the Chandra and *Spitzer*/IRAC maps. The common IR/X-ray mask leaves $\sim 68\%$ of the pixels in the overlapping $8' \times 45'$ region for the Fourier analysis. The superior resolution and depth reached in the *Spitzer* exposure maps causes faint X-ray sources to be subtracted well below the detection threshold of the Chandra maps. The depth of the joint CXB \times CIB analysis is therefore mostly determined by the IR source subtraction. We therefore assume a fixed magnitude limit in the *Spitzer*/IRAC maps with X-ray sources removed according to a selection function $\eta(S_X | m_{\text{lim}})$ where m_{lim} refers to the IRAC magnitude limit of the near-IR mask. We also tried relaxing the assumption of a fixed m_{lim} and instead used the complement of the source selection completeness in the SEDS EGS field. This has little effect on our results. In order to obtain $\eta(S_X | m_{\text{lim}})$ at flux levels inaccessible to current X-ray observatories, we look at the distribution of f_X/f_{IR} predicted in the semi-analytic model (SAM) of ref. (82) mapped onto the Millennium Simulation. Mock lightcones based on this model were constructed by ref. (165). Although mostly consistent with galaxy counts in the optical, the semi-analytic model tends to *overestimate* the number of small systems causing the abundance of faint galaxies to overpredict observed $3.6\mu\text{m}$ and $4.5\mu\text{m}$ counts. We therefore apply a post-correction

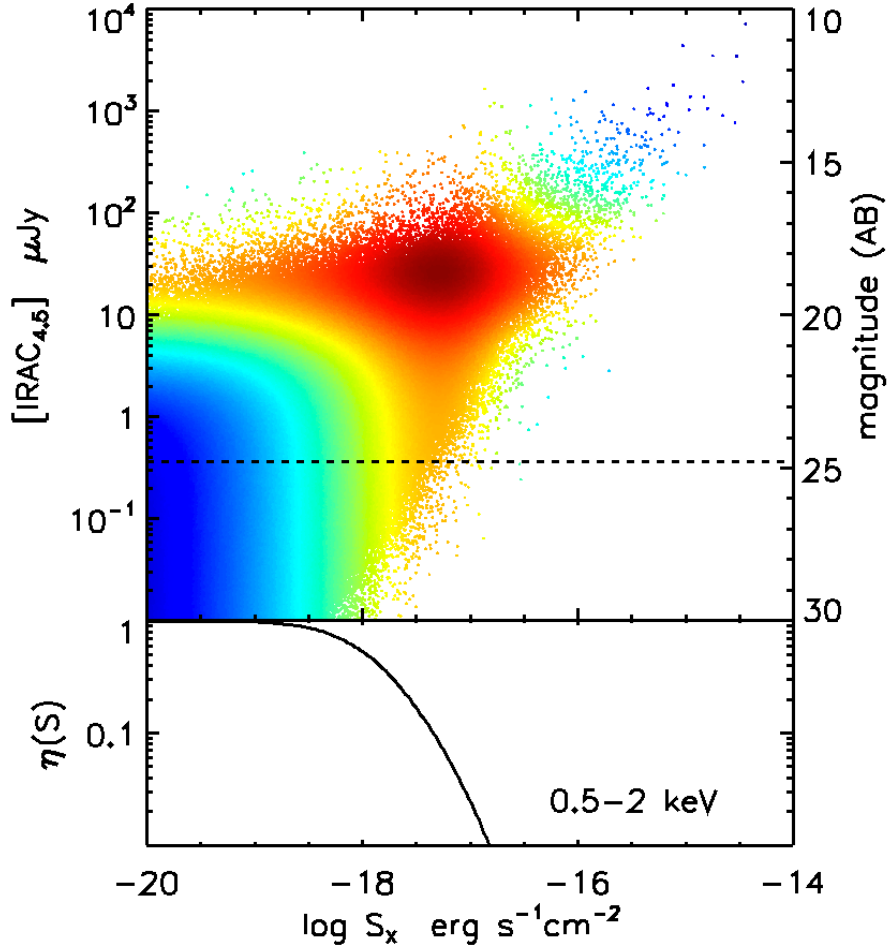


Figure 4.3 *Top:* The $4.5\mu\text{m}$ vs $0.5\text{-}2\text{keV}$ flux distribution of normal galaxies from the Millennium Simulations lightcones of Henriques et al. 2012. The flux limit of the *Spitzer*/IRAC maps of ref. (66) is shown as the horizontal line. The color scheme corresponds to the log-scaled flux contribution to the total (resolved+unresolved) CIB×CXB SdN/dS , red/blue representing large/low contribution *Bottom:* the unresolved selection for X-ray galaxies using an IR threshold of 25 mag extracted from this catalog (see Eqn 4.9).

to the galaxy population by shifting excess sources of magnitude m by a factor

$$\Delta m = \frac{|m(n_{obs}) - m(n = n_{obs})|}{\delta} \quad (4.8)$$

where $m(n)$ are the Millennium SAM derived counts and n_{obs} are the observed counts. We find that for a modification factor of $\delta = 1.05$ the population of ref. (165) is brought into a good agreement with the observed counts while conserving the total number of systems and their redshift distribution. Figure 4.3 shows the $4.5\mu\text{m}$ versus 0.5–2 keV brightness distribution of normal galaxies according to the Millennium SAM where we have used the SFR and M^* to predict the X-ray luminosity via $L_X = \alpha M^* + \beta \text{SFR}$ of ref. (207) and include a scatter of $\sigma = 0.4$ (this is the same relation as the L_X - L_{IR} in Equation 4.6 with the conversion $\text{SFR}/L_{IR}=9.8 \times 10^{11}$). The approximate detection limit of the *Spitzer* maps is shown in Figure 4.3 as horizontal line and the color scheme scales with flux per solid angle i.e. depicting the contribution to the total CXB×CIB background. From Figure 4.3 it is clear that most of the background light is resolved and eliminated in the masking process with a diminishing contribution from the remaining unresolved sources towards the bottom left. We define the selection function of 0.5–2 keV source removal as the unresolved galaxy fraction

$$\eta(S_X|m_{lim}) = \frac{N(S_X|m > m_{lim})}{N(S_X|m)} \quad (4.9)$$

and display it in the bottom panel in Figure 4.3. This shows that for an IR limit of

25 mag, 90% of sources are removed at $\simeq 3 \times 10^{-18} \text{erg s}^{-1} \text{cm}^{-2}$ which considerably fainter than the flux limit of CDFS (221). Systems identified as subhalos in the Millennium catalog were removed together with its parent halo provided it is brighter than m_{lim} . The subhalos have little effect on our results.

Our XLF model allows us to construct the flux production rate per solid angle from undetected galaxies by folding $\eta(S)$ into Equation 1.19

$$\frac{dF_X}{dz} = \int \eta(S) S \frac{dn}{dS dz} dS \quad (4.10)$$

where F_X is the X-ray flux per solid angle. Figure 4.4 shows the history of the emitted X-rays from galaxies remaining after removing IR sources brighter than 25 mag. Very little CXB remains at $z \lesssim 0.5$ after source subtraction but rises thereafter and peaks at $z \sim 1$ close to the peak of the star formation history.

4.4.2 X-ray AGN

The resolved CXB is dominated by AGN populations which have been studied in detail by Chandra and XMM-Newton out to $z \sim 3$. For X-ray AGN we use the population model of ref. (231) based on X-ray luminosity functions and evolution of AGN. The models consider the observed XLFs, k -corrections, absorption distribution and spectral shapes of AGN and return the observed X-ray flux distribution at any redshift. The models have been shown to adequately reproduce source counts, redshift distribution and intrinsic column densities. Our adopted AGN population contains sources in the $0 < z < 8$ range with a wide range in luminos-

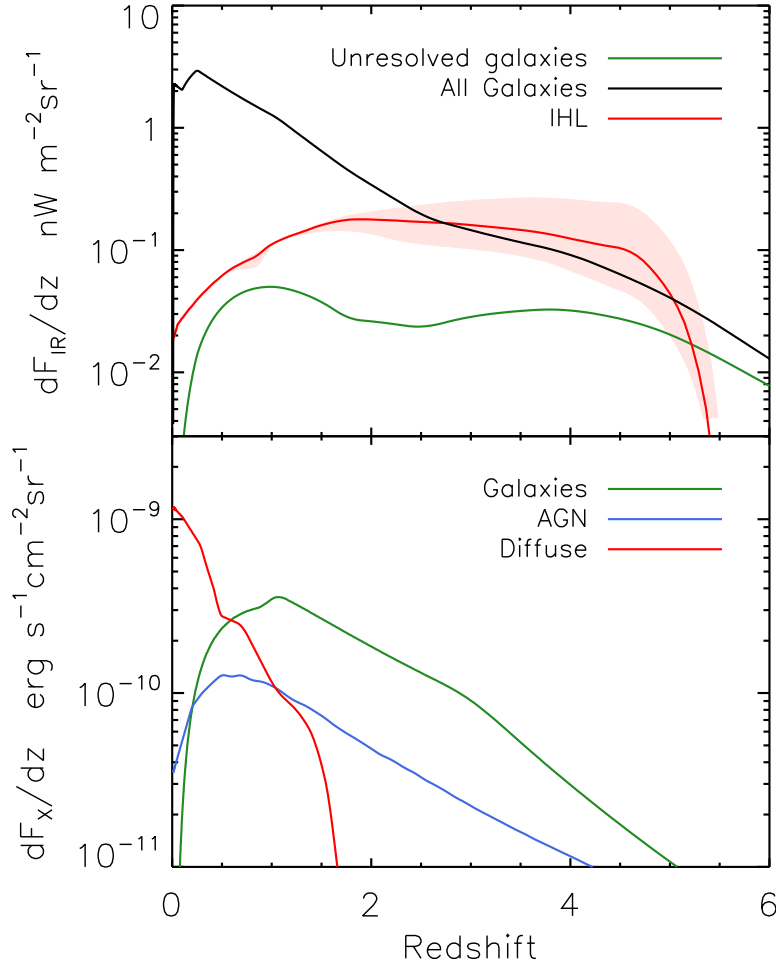


Figure 4.4 *Top*: The unresolved CIB ($4.5\mu\text{m}$) production rate from unresolved galaxies, all galaxies and intrahalo light (green, black, red). The light shaded region shows the range of IHL flux for SED templates with different ages (20–900 Myr), metallicities ($0.04\text{--}0.001Z_{\odot}$) and IMF. Model details are explained in Section 4.3. The AGN contribution falls slightly below the plot range. *Bottom*: The unresolved 0.5–2 keV CXB production histories from galaxies, AGN and diffuse gas (green, blue, red).

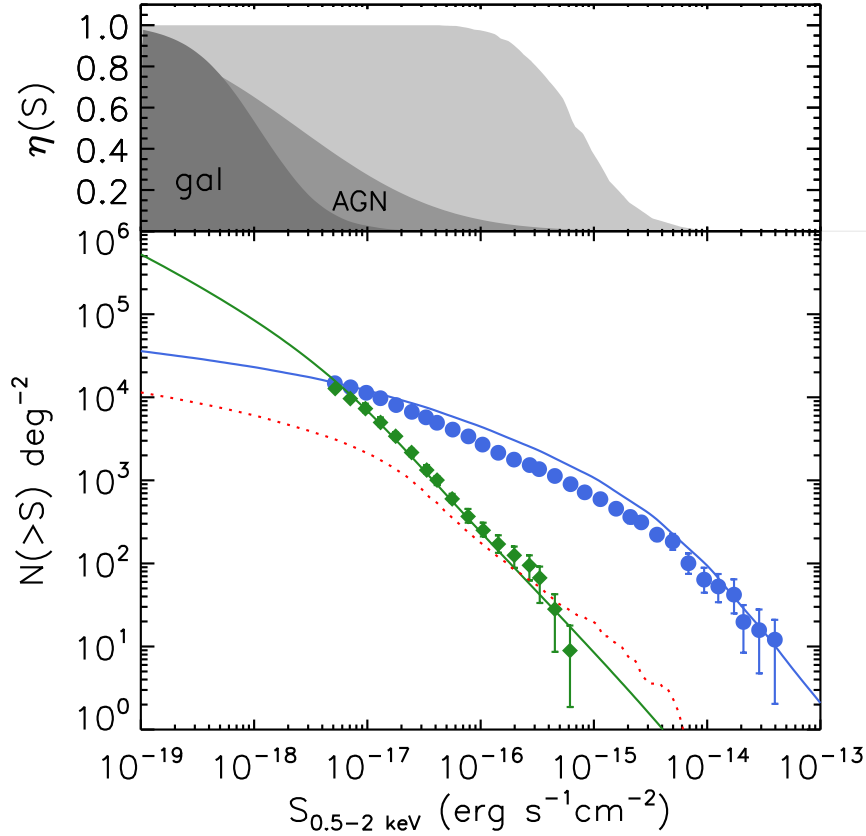


Figure 4.5 *Upper:* The selection of the unresolved regime for galaxies (darkest gray shade) and AGN (gray shade). Note that for a constant m_{IR} limit, a larger fraction of AGN remain unresolved due to their higher X/O ratio and greater dispersion. The complement of the X-ray source selection in AEGIS-XD ref. (230) is shown for comparison (lightest gray shade). This essentially defines the unresolved regime in C13 for X-ray source removal i.e. without additional IR masking. *Lower:* The source counts of ref. (204) compared with our adopted ref. (231) model for AGN (blue), and our XRB population model (green). The dotted line shows the hot gas contribution from virialized halos.

ity, $38 < \log(L_X/\text{erg s}^{-1}) < 47$, to allow for very faint unresolved sources. Column densities are $20 < \log(N_H/\text{cm}^2) < 26$. The evolution of the AGN XLF is modeled with and without an exponential decay at $z > 2.7$ on top of the extrapolated evolution from lower redshift parametrization of ref. (232), i.e. $\phi(L, z) = \phi(L, z_0)10^{-0.43(z-z_0)}$ with $z_0=2.7$ (231). We do not include the decrease at high- z which results in a CIB×CXB signal within a factor of two of the case with a decline. In Figure 4.5 we show the counts from our adopted AGN model and compare with data.

The extent to which AGN are removed by the joint IR/X-ray mask of C13 is estimated based on data from ref. (218) who provide X/IR flux ratios for 1761 sources in the COSMOS survey reaching $S_{0.5-2\text{keV}} = 1.9 \times 10^{-16} \text{erg s}^{-1} \text{cm}^{-2}$. Towards faint fluxes AGN tend to become brighter at $3.6\mu\text{m}$ deviating from the classic $X/O=0$. We fit a linear relation to the $3.6\mu\text{m}$ vs 0.5-2 keV distribution, $m_{\text{IR}} = -1.5 \log S_X - 1.7$, and extrapolate to the faint regime with a large Gaussian dispersion of $\sigma=1.5$ mag. We then apply $m_{\text{lim}} = 25$ to extract the selection $\eta(S)$ for the X-ray removal (see Eqn 4.9). The scatter $\sigma=1.5$ mag is chosen such that the resulting shot noise P_{SN}^X in the X-ray power spectrum matches the data. The selection is shown in the top panel in Figure 4.5 demonstrates the extended tail of unresolved X-ray AGN caused by the wide dispersion in their IR flux (see 218). In Figure 4.4 we show the unresolved AGN CXB production rate as function of the redshift. The bulk of the CXB flux from undetected AGN comes from $z \sim 1$.

4.4.3 Diffuse Hot Gas and WHIM

In Section 4.4.1 we calculated the CXB contribution of gas heated within galaxies. However, diffuse gas in groups and filaments (including the WHIM) also contributes to the CXB and was found to dominate the unresolved 0.5-2 keV CXB fluctuations of (210). Scaling relations indicate that the X-ray masking of C13 removes galaxy clusters and groups down to $\log(M/M_{\odot}) = (12.5 - 13.5)$ (i.e. $kT < 1.5$ keV) (233). Thus only the low luminosity (low mass) and warm population of galaxy groups and filaments contributes to the unresolved CXB.

Since this class of objects is difficult to model analytically, we describe their properties using a set of mock maps from ref. (234), who used a cosmological hydrodynamical simulation to define the expected X-ray surface brightness due to the large scale structures. The original hydrodynamical simulation (see the details in ref. (235)) follows the evolution of a comoving volume of $37.5 h^{-1}\text{Mpc}^3$ considering gravity, hydrodynamics, radiative cooling and a set of physical processes connected with the baryonic component, among which a chemical enrichment recipe that allows to follow the evolution of seven different metal species of the intergalactic medium (IGM). From its outputs, ref. (234) simulated 20 lightcones with a size of ~ 0.25 deg² each covering the redshift interval $0 < z < 1.5$. Each pixel of the maps contains information about the expected observed spectrum in the 0.3–2.0 keV band with an energy resolution of 50 eV. The emission coming from the IGM was computed assuming an emission from an optically thin collisionally-ionized gas (Apec in XSPEC) model and considering the abundances of the different metal species provided by the

simulation.

These maps/spectra have been convolved with the Chandra response in order to reproduce the effective Chandra count rates. Since the CXB data of C13 are masked for galaxy clusters, we apply a source masking on the simulated maps. We have simulated observations with the actual depth of the C13 field and added an artificial isotropic particle and cosmic background according to the levels estimated directly from the maps of C13. Random Poisson noise was artificially added to the image and we ran a simple wavelet detection with a signal to noise ratio threshold of 4. We have then excluded all the regions within which the overall encircled signal from sources is above 4σ with respect to the background. The unresolved CXB production rate averaged over all the realizations is shown in Fig. 4.4.

4.5 The Angular Auto/Cross Power Spectrum of Multiple Populations

As before, we describe cosmic background fluctuations by the angular power spectrum, $P(q) = P(q) + P_{\text{SN}}$. The first term, representing the clustering, can be related to the three dimensional power spectrum of the underlying sources, $P(k, z)$, by Equation 1.24

$$P(q) = \int \frac{H(z)}{cd_c^2(z)} \sum_i \sum_{j \geq i} \left[\frac{dF}{dz} \right]_i \left[\frac{dF}{dz} \right]_j P_{ij}(qd_c^{-1}, z) dz \quad (4.11)$$

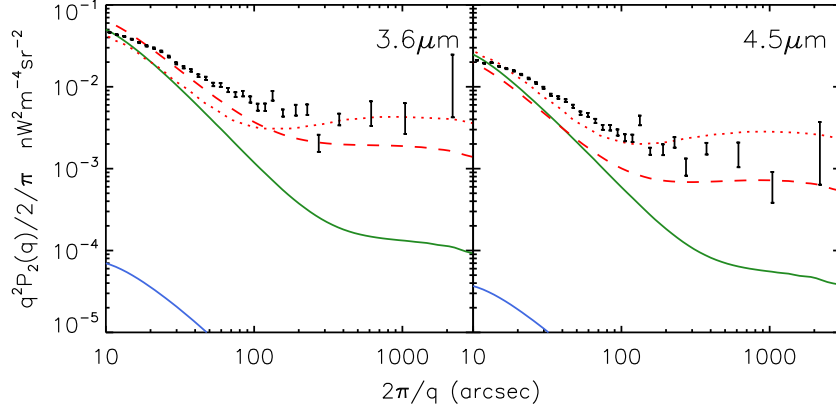


Figure 4.6 The auto power spectra of the unresolved CIB fluctuations at $3.6\mu\text{m}$ and $4.5\mu\text{m}$. Data points are from ref. (66). The contribution from known galaxies and AGN are show as green and blue line respectively (the AGN contribution barely visible above the plot range). The hypothetical IHL contribution is shown as red dashed line. We compare this with the original IHL model from ref. (67) (dotted lines). All models are convolved with the IRAC beam taken from ref. (54; 78).

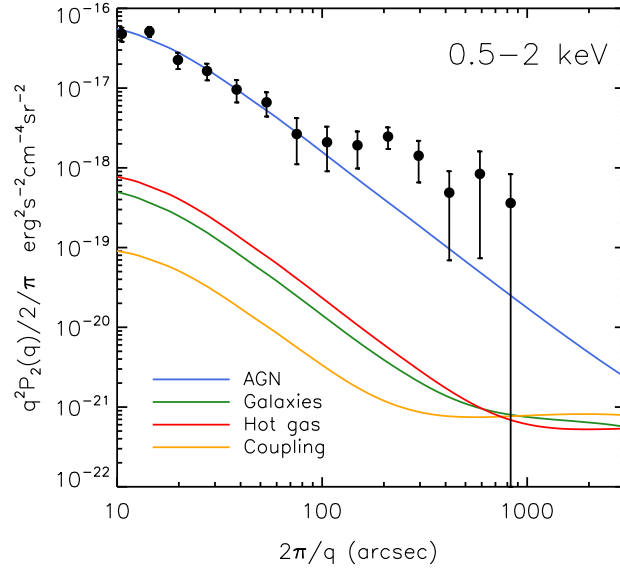


Figure 4.7 The auto power spectra of the unresolved X-ray background fluctuations from different populations at the levels of C13. The contribution of normal galaxies (mostly XRBs) is shown in green and AGN in blue and hot/warm gas in red. We also display the net coupling term of the three components (orange).

which we have modified to account for several distinct populations. The quantities in the square brackets are the unresolved flux production rates constructed in the previous sections for each source population which are denoted by the indices i and j running over 1: galaxies, 2: AGN, 3: diffuse emission. The summation results in six terms, three auto power terms ($i = j$) and three cross terms ($i \neq j$) that represent the coupling of different populations that live at the same epochs and share the same environments. The shot noise then takes the form

$$P_{\text{SN}} = \int_0^{S_{\text{lim}}} S^2 \sum_i \left[\frac{dn}{dS} \right]_i dS \quad (4.12)$$

where S_{lim} is the minimum detected source brightness and i denotes the source population as before. Note, that the shot noise, sometimes called Poisson term, does not have coupling (cross) terms as it represents a random process and is uncorrelated between different populations. Figures 4.6 and 4.7 show the modeled auto power spectrum of the angular fluctuations in the CIB and the CXB respectively, comparing them with current measurements.

In the description above, “coupling” terms ($i \neq j$) refer to the correlation of different populations at the same wavelength, not cross power between two wavelengths. The CIB×CXB cross power spectrum can be written

$$P_{\text{tot}}^{\text{X,IR}}(q) = \int \frac{H(z)}{cd_c^2(z)} \sum_i \sum_j \left[\frac{dF^{\text{X}}}{dz} \right]_i \left[\frac{dF^{\text{IR}}}{dz} \right]_j P_{ij}(qd_c^{-1}, z) dz \quad (4.13)$$

where the summation results in nine terms representing all combinations of cross

correlated X-ray and IR contributions from different source populations (note the different summation over j compared to the conditional $j \geq i$ in Equation 1.24).

The cross power of the shot noise term is

$$P_{\text{SN}}^{\text{IR,X}} = \int_0^{S_{\text{lim}}^{\text{IR}}} \int_0^{S_{\text{lim}}^{\text{X}}} S^{\text{IR}} S^{\text{X}} \frac{d^2 N}{dS^{\text{IR}} dS^{\text{X}}} dS^{\text{IR}} dS^{\text{X}} \quad (4.14)$$

which is added to $P^{\text{IR,X}}(q)$. This expression however, requires additional knowledge of the $dS_{\text{IR}}/dS_{\text{X}}$ dependence of each population in order to be evaluated. As our model construction lacks this information we use instead

$$P_{\text{SN}}^{\text{IR,X}} = \int \left[\frac{dP_{\text{SN}}^{\text{IR}}}{dz} \frac{dP_{\text{SN}}^{\text{X}}}{dz} \right]^{1/2} dz. \quad (4.15)$$

We test the accuracy of this Equation using the Millennium lightcones which give $P_{\text{SN}}^{\text{IR,X}}$ directly and find it to be a good approximation to Equation 4.14 (see Figure 4.9).

4.5.1 Halo Model

Our description of angular fluctuations requires knowledge of the power spectrum of luminous sources. The distribution of sources inside the same collapsed dark matter halos can be related to the Λ CDM matter density field adopting a *Halo Occupation Distribution* (HOD) within a widely used halo model formalism (155). Similar to the procedure in Chapter 2, the power spectrum of clustering can be approximated

as the sum of two terms

$$P_{ij}(k) = P_{ij}^{1h}(k) + P_{ij}^{2h}(k), \quad (4.16)$$

a one-halo term, P^{1h} , describing the correlated fluctuations between sources within the same parent halo, and a two-halo term, P^{2h} , arising from the spatial correlation of two sources hosted by separate parent halos. As before, the $i \neq j$ terms represent coupling terms between different populations, whereas for $i = j$ the expressions reduce to the more familiar form used in Section 2.5.2. For source populations i and j these can be written

$$P_{ij}^{1h}(k) = \int \frac{dn}{dM} \frac{(N_i^s N_j^c + N_j^s N_i^c)u(k|M) + N_i^s N_j^s u^2(k|M)}{\bar{n}_i \bar{n}_j} dM \quad (4.17)$$

$$P_{ij}^{2h}(k) = P^{\text{lin}}(k)(B_i^c + B_i^s)(B_j^c + B_j^s) \quad (4.18)$$

where

$$B_i^c = \int \frac{dn}{dM} \frac{N_i^c}{\bar{n}_i} b(M) dM \quad (4.19)$$

$$B_i^s = \int \frac{dn}{dM} \frac{N_i^s}{\bar{n}_i} b(M) u(k|M) dM. \quad (4.20)$$

The individual quantities are defined as follows

- dn/dM is the evolving halo mass function for which we use the formalism of ref. (156)
- $\langle N_i^c(M, z) \rangle$ (N_i^c shorthand) is the average halo occupation of central sources

- $\langle N_i^s(M, z) \rangle$ (N_i^s shorthand) is the average halo occupation of satellite sources
- $\bar{n}_i(z)$ is the average number density of population i such that

$$\bar{n}_i = \int (\langle N_i^c(M, z) \rangle + \langle N_i^s(M, z) \rangle) \frac{dn}{dM} dM. \quad (4.21)$$

- $P^{\text{lin}}(k, z)$ is the linear Λ CDM power spectrum computed using the transfer function of ref. (157) and the adopted cosmological parameters.
- $u(k|M)$ is the normalized Fourier transform of the NFW halo profile (158; 155)
- $b(M, z)$ is the linear halo bias adopted from the ellipsoidal collapse formalism of ref. (156)

It should be kept in mind that all quantities in Equations (4.16)–(4.19) are evolving with redshift but we have omitted this in the expressions to keep the notation tidy.

4.5.2 Halo Occupation, Bias and Mass Selection

The halo occupation distribution (HOD) has been widely investigated for both galaxies and AGN. We adopt standard parameterizations of $N^c(M)$ and $N^s(M)$ which have been found to match observed data. For galaxies, we assume the four parameter description of (159)

$$N_{\text{gal}}^c = \frac{1}{2} \left[1 + \text{erf} \left(\frac{\log M - \log M_{\text{min}}}{\sigma_{\log M}} \right) \right], \quad (4.22)$$

$$N_{\text{gal}}^s = \frac{1}{2} \left[1 + \text{erf} \left(\frac{\log M - \log 2M_{\text{min}}}{\sigma_{\log M}} \right) \right] \left(\frac{M}{M_{\text{sat}}} \right)^\alpha, \quad (4.23)$$

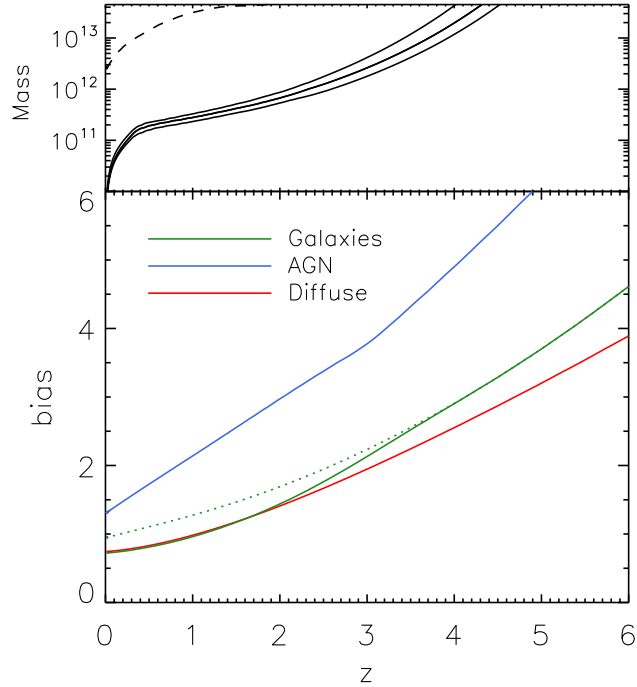


Figure 4.8 *Upper:* The approximate lowest halo mass removed by the IR mask as a function of redshift obtained from the Millennium SAM of ref. (82). The three lines correspond to 80,90,95% of systems in the Millennium catalog being removed (top to bottom). The dashed line indicates the approximate removal threshold of groups/clusters in the X-ray maps (see 236) *Lower:* The large scale bias, b_{eff} (Eqn. 4.27), from galaxies, AGN and diffuse components. The solid lines show the biasing for a masked density field with the mass selection function in the upper panel whereas the dotted lines show the case of no source subtraction. Notice that at low redshift, the density field of undetected systems is underbiased.

where M_{\min} is the minimum halo mass that can host a central galaxy and $\sigma_{\log M}$ controls the width of the transition of the step from zero to one central galaxy. The satellite term has a cut-off mass which is twice as large as the one for central galaxies and grows as a power-law with a slope of α and is normalized by M_{sat} . The amplification of the fluctuations through large scale biasing is most sensitive to the choice of M_{\min} which is not well known as galaxies in the lowest mass halos are not detected. At a given redshift however, the source subtraction removes the massive halos from top-down and limits the range of mass scales where the unresolved fluctuation signal arises, $M_{\min} < M < M_{\text{cut}}(z)$, where $M_{\text{cut}}(z)$ is the lowest mass halo removed at z (see Figure 4.8, upper). We have adopted the following parameters of the HOD-model motivated by SDSS measurements of ref. (160): $\sigma_{\log M} = 0.2$, $M_{\min} = 10^{10} M_{\odot}$, $M_{\text{sat}} = 5 \times 10^{10} M_{\odot}$, and $\alpha = 1$ where we have deliberately chosen a low cutoff mass, M_{\min} , allowing low mass halos hosting galaxies well into the unresolved regime.

The HOD of AGN is less certain due to low number statistics but AGN seem to be preferentially found in halos of $\sim 10^{12.5} M_{\odot}$. The HOD has been measured for X-ray selected AGN at $z \lesssim 1$ (237; 238; 239) and optical quasars out to $z \sim 3$ (240; 241). Previous studies suggest that, compared to optical quasars, X-ray selected AGN are more strongly clustered and reside in more massive host halos but the host halo mass range is insufficiently constrained for a definitive conclusion (242). Like galaxies, the central AGN are modeled as a softened step function at M_{\min} but the satellites

are described by a power law with a low mass rolloff

$$N_{\text{AGN}}^c = \frac{1}{2} \left[1 + \operatorname{erf} \left(\frac{\log M - \log M_{\min}}{\sigma_{\log M}} \right) \right], \quad (4.24)$$

$$N_{\text{AGN}}^s = \left(\frac{M}{M_1} \right)^\alpha \exp \left(-\frac{M_{\text{cut}}}{M} \right) \quad (4.25)$$

This description has five free parameters: M_{\min} , the characteristic mass scale of the step where the HOD goes from zero to a single AGN per halo, with the transition width controlled by $\sigma_{\log M}$. The mass at which a halo contains on average one satellite AGN is described by M_1 ; α is the power-law index controlling the steepness of the satellite HOD with increasing host mass; M_{cut} is the mass scale below which the satellite HOD decays exponentially. We have chosen parameters obtained in a numerical study of ref. (243) which agree with measured values when a selection of $L_{\text{bol}} > 10^{42} \text{erg/s}$ is applied. We interpolate the redshift evolution of the $L_{\text{bol}} > 10^{42} \text{erg/s}$ parameters given in Table 2 of ref. (243).

The HOD of our diffuse component is somewhat uncertain as it does not describe the same population in X-rays and IR i.e. hot/warm gas as opposed to diffuse starlight. We allow the diffuse component to trace the NFW halo profile by considering a satellite term only, setting the HOD of central sources to zero. For diffuse IR, we adopt the parameters from the IHL model of ref. (67) discussed in Section 4.3.3, and assume that this component arises in halos in the $\sim 10^9 - 10^{12} M_\odot$ range. However, gas does not reach sufficient temperatures in such small halos but we neglect this by allowing hot gas is to live in halos anywhere below the mass limit of detected (and removed) groups and clusters identified by ref. (236) in the EGS

field (see dashed line in Fig. 4.8).

When faced with source-subtracted images, the density field is modified in the process of masking the brightest sources which live in the most massive, and consequently, most biased halos. This effect can be accounted for by knowing the mass dependent luminosity distribution i.e. the conditional luminosity function. Since we do not have this information, we use the semi-analytical model of (82) mapped onto the Millennium Simulations to explore the halo mass dependence of source removal in deep IR maps. We eliminate all galaxies brighter than $m_{\text{lim}}=25$ and construct a mass selection function defined as the fraction of unresolved systems as a function of host halo mass

$$\eta(M, z) = \frac{N(M, z | > m_{\text{lim}})}{N(M, z)}. \quad (4.26)$$

We display this function in Figure 4.8 (upper panel) which shows the mass scale at which 80%, 90% and 95% of the systems are removed as a function of redshift. We multiply our galaxy HOD (Eqn. 4.22) by this function, thereby subtracting the massive halos from the density field (including their satellites). Since this function is derived from galaxies, we do not apply this mass selection to the AGN and diffuse component and instead use the X-ray cluster/group detection limits of ref. (236) as the upper mass limits. The overall effect of this is shown in Figure 4.8.

The amplification of fluctuations through large scale biasing of the sources

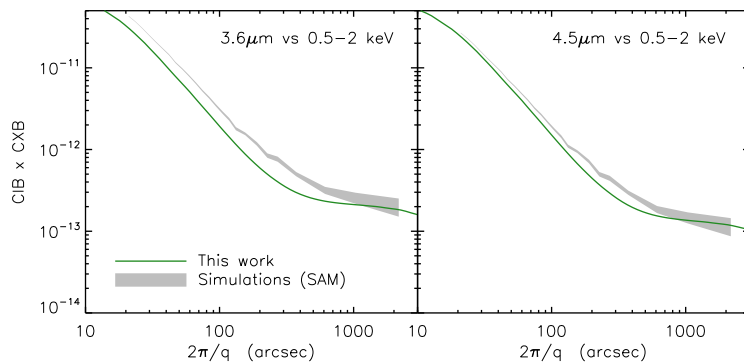


Figure 4.9 The net cross-power spectrum $q^2 P^{\text{IR,X}}(q)/2/\pi$ from normal galaxies in units of $\text{erg s}^{-1}\text{cm}^{-2}\text{nWm}^{-2}\text{sr}^{-2}$. The green line shows the prediction from our population model calculated using the Limber equation and the halo model formalism described in the text. The gray areas show the result from directly Fourier transforming simulated images, $P_{\text{IR,X}}(q) = \langle \Delta_{\text{IR}}(q)\Delta_{\text{X}}^*(q) \rangle$, obtained from a semi-analytic models based on the Millennium Simulation (82).

follows from Equations 4.19 in the limit where $u(k|M) \rightarrow 1$, or equivalently

$$b_i^{\text{eff}}(z) = \int \frac{dn}{dM} \frac{N_i^c + N_i^s}{\bar{n}_i} b(M, z) dM \quad (4.27)$$

where the mass dependent halo bias comes from the prescription of ref. (156). The quantity is shown in Figure 4.8 for galaxies, AGN and diffuse emission. We also show the bias without halo subtraction due to $\eta(M)$ i.e. in the absence of source masking. Note, how the density field becomes underbiased at low redshifts where the mask is most effective.

4.5.3 Comparing fluctuation models with N-body simulations

In real measurements, the angular power spectrum is obtained directly from the masked and Fourier transformed image, $P_{mn}(q) = \langle \Delta_m(q)\Delta_n^*(q) \rangle$. However, our

calculation of $P(q)$ relies on the projection of emitting populations via the Limber equation with empirically motivated assumptions for their HOD. A more sophisticated treatment would link the source luminosities to host halo masses in a conditional luminosity function, $\Phi(L(M))$ (see e.g. 244; 245). In order to test the validity of the approximations made, we make use of the Millennium Simulation SAM of ref. (82) to derive the unresolved CIB \times CXB power spectrum from galaxy populations. The evolving simulation box has been projected to construct lightcones that provide 2 deg^2 mock images of the extragalactic sky based on the SAM (165). From the mock catalogs, we remove all galaxies brighter than IRAC_{3,6,4,5} magnitude 25 AB including substructure associated with the parent halo. The X-ray emission is calculated using the relation of ref. (207) $L_X = \alpha M^* + \beta \text{SFR} + (1+z)^{0.5}$ where we have added the last term to account for evolution (see Section 4.4.1).

We calculate the source-subtracted fluctuations directly from the mock images, $\langle \Delta_m(q) \Delta_n^*(q) \rangle$, and compare the results with our fluctuation model in Figure 4.9. Despite the difference in approach, this SAM and our population model predict consistent fluxes and CIB \times CXB cross-power.

4.6 Results

4.6.1 CIB Fluctuations

Figure 4.6 shows the auto power spectrum of CIB fluctuations from unresolved galaxies, AGN and IHL, comparing them with the measurements of C13. The contribution from unresolved galaxies (green) is discussed in detail in ref. (73) and

the IHL (red) is close to that of ref. (67). We only use the default model from ref. (73) which has been validated in the SEDS survey (Fig. 34 in 35) reducing the uncertainties of the faint-end extrapolation of the luminosity function. The contribution from AGN (blue) is much smaller due to their low numbers compared to IR galaxies, $< 10\%$. In addition, C13 found that their source-subtracted CIB power spectrum is independent of the X-ray mask. This means that X-ray flux that may be missed by the IR mask, such as from the wide wings of the extended Chandra PSF, will show up in the CXB power spectrum but will not contribute to the cross-power CIB \times CXB.

4.6.2 CXB Fluctuations

We find that the CXB power spectrum is dominated by shot noise from unresolved AGN (see Fig 4.7) with the contribution from galaxies and gas being considerably lower. However, a different study finds the largest contribution to come from hot gas ref. (210). There are various reasons for the different findings. First, the X-ray maps of ref. (210) are deeper (4Ms) than C13 (800ks) allowing ref. (210) to directly mask AGN to much fainter levels. Second, ref. (210) modeled AGN in the luminosity range $42 < \log(L/L_{\odot}) < 47$ whereas we include AGN all the way down to $\log(L/L_{\odot})=38$. This makes a substantial difference in the abundance of faint AGN.

The net CXB from unresolved galaxies and AGN is 2.1×10^{-13} and 7.9×10^{-14} erg s $^{-1}$ cm $^{-2}$ deg $^{-2}$ respectively. Whereas the CXB power spectrum is consistent with being entirely due to shot noise from unresolved AGN there is a hint of

additional clustering towards large scales which is not accounted for. No reasonable amount of clustering (bias $\lesssim 30$) is sufficient to account for enhanced CXB fluctuations on scales $> 200''$. If this component is real and extragalactic in nature, it could indicate the source of the coherence with the CIB fluctuations. However, it is important to note that the 0.5–2 keV fluctuations are contaminated by foreground emission from the Galaxy which is not sensitive to the removal of extragalactic point sources. Any interpretation of the CXB power spectrum therefore carries an intrinsic source of uncertainty due to the contribution of the Galaxy. A non-negligible Galaxy component at < 1 keV could explain why C13 measure a low-level of cross-correlation between [0.5–2] keV and [2–4.5]–[4.5–7] keV maps. While irrelevant for the CXB \times CIB cross-power spectrum, correcting for the Galaxy would reduce the measured CXB power spectrum. Additionally, the extended point-spread function (PSF) of Chandra could spread some fraction of the X-ray point source flux outside the finer IR mask. This would not show up in the CIB \times CXB cross-power as the large scale CIB fluctuations do not correlate with either IR or X-ray removed sources.

4.6.3 CIB \times CXB Fluctuations

We start with summarizing the resultant contributions to the cross-power from three main components appearing in Figure 4.10: galaxies, AGN and diffuse:

- **Galaxies.** The largest contributions to the cross-power comes from galaxies ($\text{gal}_{\text{IR}} \times \text{gal}_{\text{X}}$, green line) and AGN ($\text{gal}_{\text{IR}} - \text{AGN}_{\text{X}}$, purple line). A significant

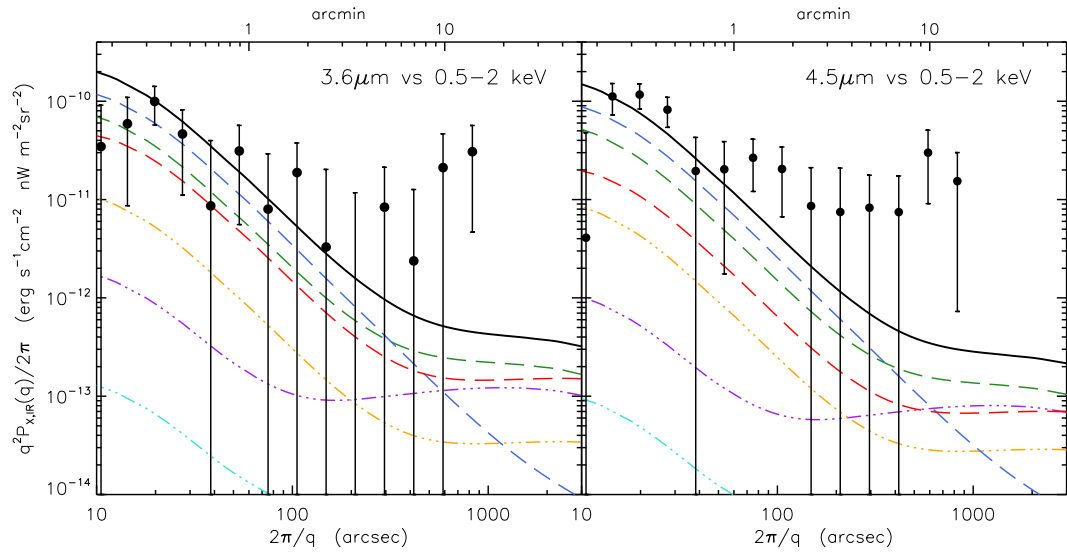


Figure 4.10 The X-ray versus IR cross-power terms of all source populations compared to measurements from ref. (77). The total cross-power spectrum from all terms is shown as solid black line. The individual terms are $\text{galaxies}_{\text{IR}}\text{-galaxies}_{\text{X}}$ (green), $\text{galaxies}_{\text{IR}}\text{-AGN}_{\text{X}}$ (purple), $\text{galaxies}_{\text{IR}}\text{-diffuse}_{\text{X}}$ (orange), $\text{AGN}_{\text{IR}}\text{-galaxies}_{\text{X}}$ (turquoise), $\text{AGN}_{\text{IR}}\text{-AGN}_{\text{X}}$ (blue) and $\text{diffuse}_{\text{IR}}\text{-diffuse}_{\text{X}}$ (red). Auto terms are shown as dashed lines ($i = j$) whereas coupling terms ($i \neq j$) are shown as dashed-dotted lines.

galaxy–galaxy component is expected because i) they make-up a substantial unresolved CIB component and ii) dominate AGN at faint X-ray fluxes (see Fig. 4.5). The small scale cross-power is in good agreement with the data, the $\text{gal}_{\text{IR}} \times \text{gal}_{\text{X}}$ shot noise making up $\sim 30\%$. This fraction decreases towards large scales however. In order to explain the shape of the CIB \times CXB fluctuations at all scales in terms of galaxies only, one needs to alleviate the problem of the low clustering with respect to shot noise, as is the case with the CIB fluctuations. Simply increasing the flux of the unresolved populations would overproduce the small scale power. A way of increasing the large scale power without affecting the shot noise is to enhance the galaxy bias. However, this requires bias of $\gtrsim 10$ which is not expected for faint low-mass systems. We therefore conclude that the entire CIB \times CXB signal cannot originate from normal galaxies unless future measurements show that the cross-fluctuations ($q^2 P(q)/2/\pi$) decrease towards large scales as opposed to staying roughly flat as indicated by the C13 data.

- **AGN.** Shot noise from unresolved AGN provides the largest contribution, $\sim 60\%$ to the small scale CIB \times CXB power (Fig 4.10, blue line). This is because a greater fraction of bright AGN remains unresolved after IR masking (see Figure 4.5). At large scales, their $\text{AGN}_{\text{IR}} \times \text{AGN}_{\text{X}}$ contribution is small due to lower flux in both IR and X-rays compared with galaxies. However, a substantial contribution comes from X-ray AGN correlating with IR galaxies (purple line). As shot noise does not appear in this term, the cross power

spectrum has a shape that resembles the data but with an amplitude which is more than an order of magnitude below the data. To test whether this term could be enhanced, we examined the case in which the IR source subtraction removes no additional AGN i.e. only AGN detected in X-rays are removed. This gives an amplitude that is one order of magnitude below the data points. Enhancing the clustering of the AGN population to the levels of very biased high- z quasars, corresponding to AGN living in $> 10^{13}M_{\odot}$ halos, still falls below the measured levels. In fact, both our AGN population model (231) and our AGN removal selection (218) are chosen conservatively and should, if anything, give a smaller signal (see Figure 4.5).

- **Diffuse.** Dispersed starlight around and between masked galaxies can share the same environment with diffuse warm gas in collapsed halos and filaments. For distant structures however, the thermal spectrum of the ionized gas, ~ 1 keV, quickly redshifts out of the 0.5-2 keV band (see Section 4.4.3) and has therefore limited correlations with the IHL which mostly arises at different epochs, $z \sim 1 - 4$. Despite this, the large scale CIB \times CXB component arising between IHL and warm gas at $z < 1$ is comparable to that of galaxies and AGN (see Figure 4.10, red). The diffuse component could be made larger if the bulk of IHL emission arose at low- z in halos $\gtrsim 10^{12.5}M_{\odot}$, but this would be unlikely to explain the entire CIB \times CXB data. Coherence between IHL and X-ray galaxies/AGN is also difficult to accommodate for the following reasons. In the resolved regime, the point sources are masked so any X-ray

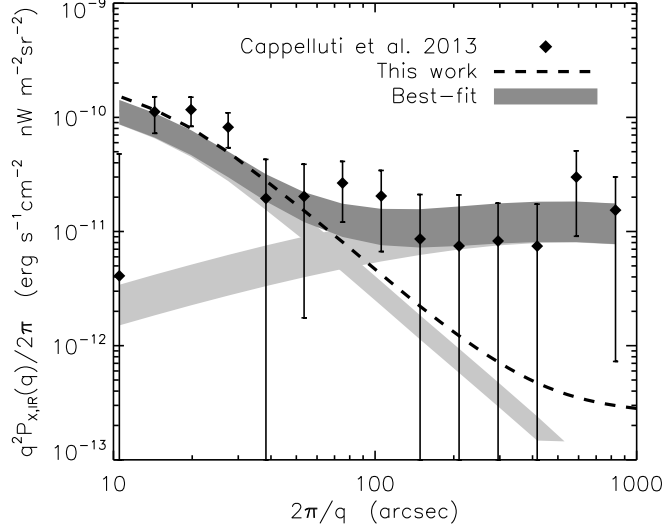


Figure 4.11 The 4.5 vs 0.5–2 keV cross power spectrum. Data points are from C13. The dark gray region corresponds to the 1σ uncertainty in the best fit model $P(q) = a_1 P_{\text{ACDM}} + a_2$ with the two individual terms shown as light gray regions. Our model of net contribution from galaxies, AGN and diffuse emissions is shown as black dashed line.

emission originating in the central regions is eliminated with no correlation with diffuse IR light outside the mask. In the unresolved regime, the IR galaxies themselves should dominate over IHL which can only constitute a fraction of the total galaxy light. We already account for the coherence of unresolved IR galaxies with X-ray galaxies/AGN. Furthermore, the fact that the CIB fluctuations are not sensitive to the X-ray mask argues against the removed X-ray sources being responsible for the $\text{CIB} \times \text{CXB}$ signal. We note the additional problems with the IHL hypothesis in Sec. 4.3.3.

Despite the large uncertainties in the data, there seems to be a systematic lack of cross-power at the large scales $> 300''$ where the source clustering is in the linear regime. At small scales, our modeled shot noise term is in agreement with

Table 4.1 Comparison of our net model with the best-fit model $P(q) = a_1 P_{\Lambda\text{CDM}} + a_2$. The power is in units of $\text{erg s}^{-1}\text{cm}^{-2}\text{nW m}^{-2}\text{sr}^{-1}$

	Clustering ¹		Shot noise	
	$(a_1 \times 10^{17})$		$(a_2 \times 10^{19})$	
	$3.6\mu\text{m}$	$4.5\mu\text{m}$	$3.6\mu\text{m}$	$4.5\mu\text{m}$
Best-fit	2.5 ± 2.1	4.3 ± 1.7	1.0 ± 0.4	1.3 ± 0.3
This work	0.21	0.11	1.93	1.44

Note. — ¹clustering at $1000''$

the data. To better understand these results, we consider a simple model composed of linear ΛCDM clustering and a noise term, $P(q) = a_1 P_{\Lambda\text{CDM}} + a_2$ where a_1 and a_2 are free parameters and $P_{\Lambda\text{CDM}}$ is normalized to unity at $1000''$. This model is then convolved with the Chandra response function. For $4.5\mu\text{m}$ vs $[0.5\text{--}2\text{ keV}]$, we find best-fit parameters $a_1 = (4.3 \pm 1.7) \times 10^{-17}$ and $a_2 = 1.3 \pm 0.3 \times 10^{-19}$ in $\text{erg s}^{-1}\text{cm}^{-2}\text{nW m}^{-2}\text{sr}^{-1}$, resulting in a $\chi^2/12 = 1.2$ (see Figure 4.11)³. The net power from our model of $z < 6$ sources (black line) is a poor fit to the data ($\chi^2/8 = 2.8$) falling more than an order of magnitude below the best-fit model. This distinction is not significant at $3.6\mu\text{m}$ vs $[0.5\text{--}2\text{ keV}]$ due to the large uncertainties but the systematically growing discrepancy towards large scales suggests the same behavior as $4.5\mu\text{m}$ vs $[0.5\text{--}2\text{ keV}]$. This is illustrated in Figure 4.12.

³The smallest scale data point at $10.5''$ is offset with respect to the rest and as a result leads to smaller a_2 and drives up the χ^2 . This is why the gray best-fit region seems somewhat below the small scale data points. If we neglect this data point the best-fit model is brought in perfect agreement with our modeled shot noise.

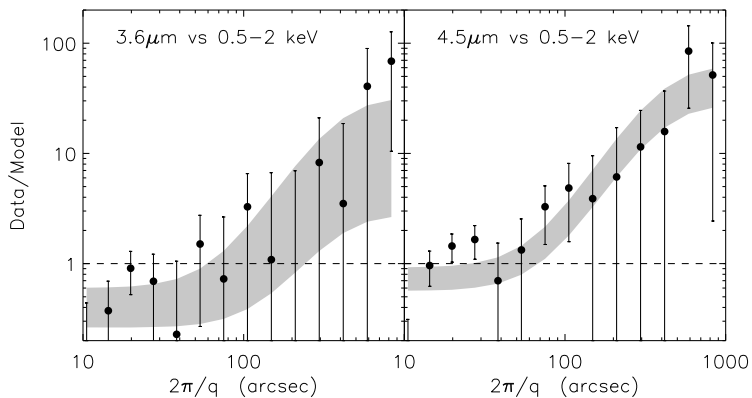


Figure 4.12 The systematic discrepancy of the cross power spectra of our model and the data as a function of angular scale, $P_{\text{data}}(q)/P_{\text{model}}(q)$. The normalized model is indicated by the dashed line. The 1σ regions of the best-fit two parameter model is show in light gray.

4.7 Discussion

In this paper we have considered known populations of X-ray sources at $z < 6$ in an attempt to explain the measured spatial coherence of the unresolved CIB and CXB. The dominant contribution to the modeled CIB \times CXB signal comes from unresolved galaxies containing X-ray binaries and IR galaxies associated with X-ray emitting AGN found within the same large scale structures. However, we find that the combined contribution from galaxies, AGN and hot gas, is unable to produce the large scale cross-power needed to explain the data. At $4.5\mu\text{m}$ vs $0.5\text{--}2$ keV, the large scale cross-power is only $(2.6 \pm 1.0)\%$ of the best-fit model, but the discrepancy decreases towards small angular scales where the shot noise becomes consistent with the best-fit. At $3.6\mu\text{m}$ vs $0.5\text{--}2$ keV these identifications are not robust due to larger uncertainties in the data.

While other mechanisms capable of producing a correlation between X-rays and IR may exist, they are generally expected to be much weaker than the dominant forms considered in this work: galaxies, AGN and hot gas. Thermal emission from hot dust $\sim 700\text{K}$ would have to arise in the local universe as it would otherwise redshift out of the near-IR bands and it is also inconsistent with the observed blue color of the source-subtracted CIB fluctuation in the $2.4\text{-}4.5\mu\text{m}$ range. Because of its red colors, any dust dominated component would have to be underdominant in the CIB fluctuations while being associated with X-ray emission from the dominant CXB component i.e. the Galaxy foreground or obscured AGN. Infrared cirrus emission in the Galaxy should absorb X-rays and exhibit a *negative* cross-power contrary to the measurements of C13. In the case of obscured AGN, they make up a greater fraction of the hard CXB and are less significant in soft X-rays. This is not consistent with the fact that C13 detect CIB \times CXB cross-correlation in the $0.5\text{-}2$ keV band but not in the harder bands. Furthermore, the cross-correlation between the $[0.5\text{-}2]$ keV band and both $[2\text{-}4.5]$ and $[4.5\text{-}7]$ keV are small. There is a hint of clustering in the CXB power spectrum at $>100''$ which may or may not be the source of coherence with the CIB. However, the component producing the large scale CIB \times CXB cannot constitute less than $\sim 15\text{-}20\%$ of the CXB clustering.

The possibility that the CIB \times CXB signal is contributed by high- z miniquasars is discussed in C13. Such objects are expected to form early and grow rapidly in order to explain the population of bright quasars already in place at $z \sim 6$. Ref. (79) have constructed a population model of highly obscured direct collapse black holes that is able to account for 1) net CIB measurements and γ -ray absorption

constraints, 2) the shape and amplitude of the source-subtracted CIB fluctuations, 3) the unresolved soft CXB level, and 4) the shape and amplitude of the spatial coherence in the unresolved CIB \times CXB. The inclusion of such a component improves the CIB \times CXB best-fit considerably (see Fig 4.11). Whether these requirements can be realistically satisfied physically by other types high- z miniquasars and at the same time stay within limits imposed by reionization and black hole mass growth, will be investigated in future work.

Chapter 5: Summary and Conclusions

In this dissertation I have sought to understand current CIB measurements in terms of all sources emitting since the era of the first stars. First, I did so by modeling the CIB arising from known galaxy populations using 233 measured UV, optical and NIR luminosity functions from a variety of surveys spanning a wide range of redshifts. I found that fluctuations from known galaxy populations are unable to account for the large scale CIB clustering signal seen by current space observatories, and continue to diverge out to larger angular scales. This suggests that known galaxy populations are not responsible for the bulk of the observed fluctuation signal and favors a new population of faint and highly clustered sources. I also empirically reconstructed the evolving extragalactic background light from galaxies, deriving the associated opacity of the universe to high energy photons out to $z \sim 4$. In the absence of significant contributions to the cosmic diffuse background from unknown populations, I found that the universe appears to be largely transparent to γ -rays at all *Fermi*/LAT energies out to $z \sim 2$ whereas becoming opaque to TeV photons already at $z \lesssim 0.2$. Finally, I studied contributions from extragalactic populations to the positive cross-correlation signal of the CIB fluctuations with the CXB. I modeled the X-ray emission from AGN, normal galaxies and hot gas, calculating their

CXB contribution and spatial coherence with all infrared emitting counterparts. At small angular scales, I found the coherence between the CIB and the CXB to be consistent with galaxies and AGN whereas at large scales the net contribution could only account for a fraction of the signal. The discrepancy suggests that the signal originates from the same unknown source population producing the CIB clustering signal out to ~ 1 deg.

5.1 Future Outlook

There exist several avenues along which CIB studies can be advanced, both in the near future and in the long term. In the short term, we will rely on more measurements from ongoing missions and better theoretical modeling of both the signal and foregrounds. New fluctuation measurements will soon be emerging from *HST*/WFC3, *CIBER* and *AKARI*/IRC, *Spitzer*/IRAC, *Chandra*, and *XMM-Newton*, all of which will provide additional insights. However, there are several future observatories on the horizon that promise to deliver unprecedented measurements of CIB fluctuations, both in terms of depth and angular scales. Most notably, the James Webb Space Telescope (JWST), currently scheduled to launch in 2018, will probe deeper than any other instrument enabling the removal of very faint sources while leaving plenty of background pixels due to its superb resolution. The set of filters for its Near Infrared Camera covers the entire near-IR range $0.6\text{-}5\mu\text{m}$ including $1\text{-}3\mu\text{m}$ where little CIB data currently exists. NIRCAM will allow for a targeted search for a Lyman-break in the CIB via cross-correlations between individual filters, thereby

uniquely determining the epoch of the signal.

The Euclid telescope is scheduled to launch in 2018/19 with major science goals focused on dark energy, dark matter, primordial initial conditions, and modified gravity. With a target survey area of 20,000 deg² in several bands covering 0.5–2 μ m the observatory will enable CIB fluctuations measurements of unprecedented accuracy. Our ESA selected science program, *Looking at the Infrared Background Radiation Anisotropies with Euclid* (LIBRAE) led by NASA/GSFC, will use Euclid’s wavelength and area coverage to conclusively identify the origin of the CIB fluctuations in two ways: First, a fluctuation signal originating somewhere in the $z=10\text{--}20$ range should vanish shortwards of the Lyman break where radiation is absorbed by neutral hydrogen i.e. in the $(1+z)\lambda_{\text{Ly}} = 1 - 2\mu\text{m}$ range. Second, the power spectrum of the fluctuations should start turning over at scales close to the first baryonic acoustic peak ($\gtrsim 1^\circ$) as predicted by the Λ CDM power spectrum. The precise angular scale at which this occurs depends on the angular diameter distance to the epoch where the unresolved CIB was produced.

WFIRST is a NASA-led mission that shares many of the primary science goals with Euclid. WFIRST however, with its larger mirror size, will concentrate on a smaller area 2000 deg² but reaching much deeper, ~ 27 mag. WFIRST will be well suited for measuring the CIB and will bridge the gap between JWST and Euclid in terms of depth and area.

In order to establish a clustering signal from the high- z universe from future data, one must have a good understanding of unresolved foreground galaxies at the depths and angular scales reached by each of the upcoming missions. Since the

appearance work of Helgason et al. 2012, more deep survey data has been published that provide better constraints on faint galaxy counts. In light of better constraints, CIB measurements with upcoming missions would greatly benefit from a reduction of the systematic uncertainties in the abundance of faint galaxies of Helgason et al. 2012 (HFE/LFE); i.e. better constraints of the slope for extrapolation to still fainter levels. The methodology of Helgason et al 2012 can be used to develop a reliable halo matching algorithm that populates dark matter halos in N-body simulations with observed galaxy abundances. This can be used to generate realistic mock images adapted to the instrument specifications of JWST, Euclid and WFIRST, allowing one to better understand various effects associated with CIB source subtraction. Examples of such effects include, i) the extent satellite galaxies are masked along with their parent halo, ii) to what extent the removal of the brightest, and most biased galaxies modifies the unresolved density field seen in the remaining pixels, and iii) whether any form of missing light in extended halos between masked galaxies can affect measurements.

The *Fermi*/LAT instrument is likely to yield important insights into the CIB. The growing LAT database is now reaching sufficient photon statistics at its highest energy bins enabling it to probe the CIB excess from early sources. This is because the onset of γ -ray absorption occurs at lower energies for sources at higher z , bringing it into the sensitivity range of the LAT; and because the $\gamma\gamma$ -optical depth is fixed by the proper photon number density, $\propto (1+z)^3$, which at high- z becomes large even for low CIB levels. Because searching for CIB emissions from early epochs is optimally probed with $\gtrsim 10$ GeV photons, the recent release of *The First LAT Catalog of*

High Energy Sources (1FHL) would make such a search an interesting extension of Helgason & Kashlinsky 2012 (246). The 1FHL contains 47 blazars with measured redshifts above $z = 1$ (39 FSRQs, 8 BL Lacs) out of which 35 are significantly detected above 30 GeV (202). Additionally, the LAT team is currently working on a complete reconstruction of the data called Pass 8 (247) which will provide 25% more acceptance above 1 GeV, greatly increasing the high energy statistics needed for such a study.

Chapter A: Appendix

A.1 LF Binning and Interpolations

Because of degeneracy in (α, M^*, ϕ^*) , different sets of Schechter parameters can represent LFs of very similar shapes. The method used in Section 2.3 disentangles the Schechter parameters to fit their evolution individually. In addition to this, we used an alternative approach in which the shape of each measured LF is kept intact. We took each LF in its rest-frame and redshift the associated emission to the observed wavelength, $\lambda^{obs} = \lambda^{rest}(1 + z)$. We examine the all LFs that meet the criterion $\lambda_0 - \Delta\lambda < \lambda^{obs} < \lambda_0 + \Delta\lambda$ where λ_0 is the center of the NIR band and $\Delta\lambda$ is roughly the FWHM of the filter. The inserts in Figure 10 show the redshift distribution of available LFs which can be observed through JHKL. In a given band, we place each LF in redshift bins and take the functional average of $\Phi(M)$ in common bins so that we have a unique LF at each redshift. We thus have template LFs, $\Phi_i(M|z_i)$, in each of the observed NIR bands and the rest of the analysis is identical to that in Section 2.3 following from Equation (2.5) (we interpolate the evolution and project the populations onto the sky). The major shortcoming of this method is the redshift information. Averaging over several LF in a common redshift bins is immune to the effects of Schechter parametrization but comes at the cost of crude

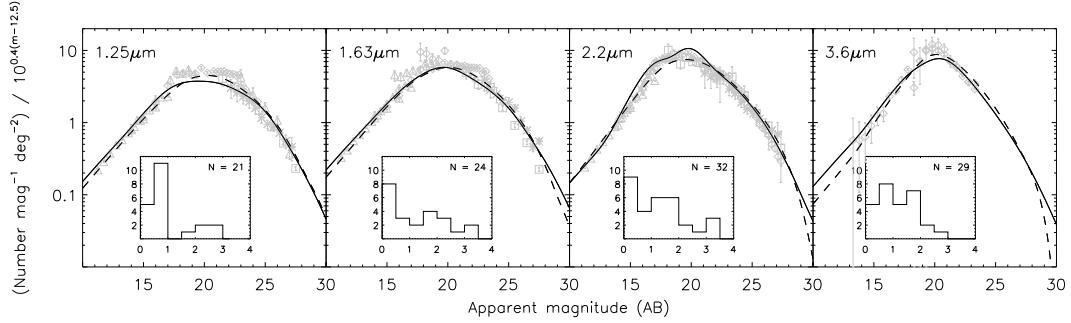


Figure A.1 Comparison between our default method (dashed) and the alternative method presented here (solid). The two curves agree to within 20% in the range shown. The data shown in the background is the same as in Figure 2.5. The insets show the redshift distribution of LFs available in for the calculation in each band (i.e. $\lambda_0 - \Delta\lambda < \lambda^{obs} < \lambda_0 + \Delta\lambda$).

evolution i.e. the sampling of z is determined by the number of z -bins. As seen in Figure A.1 there is no guarantee that there exists a LF measurement falling into $\lambda_0 - \Delta\lambda < \lambda^{obs} < \lambda_0 + \Delta\lambda$ in each redshift bin. In this case we borrow LFs from neighboring wavelengths scaling them according to synthetic spectra. Figure 10 shows that despite these limitations, we obtain very comparable number counts to the ones in Section 2.4, agreeing to within 20% in the relevant magnitude range.

A.2 Consistency notes

A.2.0.1 K-correction

Calculating the absolute magnitudes of a galaxy sample requires a k-correction to account for the offset in the rest-frame and the observed SED due to the cosmological redshift (e.g. 130; 248)

$$M_X = m_X - DM(z) - K(\lambda_X, \lambda_{X'}) \quad (\text{A.1})$$

where X refers the band of interest. The k-correction can be written (in AB magnitudes)

$$K(z) = (m_{X'} - m_X) - 2.5 \log_{10}(1 + z) \quad (\text{A.2})$$

where m_X is the observed brightness of a galaxy at redshift z and m'_X is its rest-frame brightness in X -band. The exact value of the k-correction requires knowledge of the spectral energy distribution (SED) of the source and is commonly evaluated by assuming a template SEDs based on the galaxy type/color. This treatment is fairly reliable for low- z galaxies but the correction can become large for high- z galaxies and dominate the uncertainty in the derived LF, especially in the blue bands. Recent multiband photometric surveys offer a robust way of reducing this SED dependency by utilizing magnitudes in multiple bands to constrain the best-fit SED. Not only does multiband coverage indicate SED shape but when probing the LF in the rest-frame band Y centered at λ_Y , the galaxy flux can be sampled in the band X which is closest to $\lambda_Y(1 + z)$. In other words, the observed filter (X) that best matches the redshifted rest-frame band of interest is the one that minimizes $|\lambda_X - \lambda_Y(1 + z)|$. The k-correction needed then becomes the matter of setting this quantity to exactly zero which is typically a small correction. We can rewrite Equation (A.1) in this framework

$$M_Y = m_X - DM(z) - K(\lambda_X, \lambda_Y(1 + z)) \quad (\text{A.3})$$

where the SED dependence of the k-correction is now small even at high redshifts. Backtracking the original procedure to apparent magnitudes now requires simply $K(z) = -2.5 \log_{10}(1 + z)$ which we use in Equation 2.6.

A.2.0.2 Photometric Systems

Unfortunately, there is no photometric system which is universally accepted and the different ways used to evaluate the apparent magnitude of galaxies in the survey can introduce biases affecting the derived luminosity functions (see ref. (249) for a review of photometric systems). As the flux from a galaxy diminishes from the center it will eventually drop below the background noise to be missed by the aperture. Photometric systems based on total magnitudes, such as Sérsic, are usually preferred since they directly quantify the physical flux while apertures such as Kron and Petrosian will always suffer from missed light to some extent. However, total magnitudes typically assume an extrapolated profile which is model-dependent and has larger measurement errors (118). The Petrosian system can be advantageous since it compensates for the effects of seeing by increasing the fraction of the light recovered from a galaxy when its angular size is small (250). Despite this, Petrosian magnitudes are found to underestimate Sérsic by 0.2 mag (251; 250). Likewise, 2MASS Kron and isophotal magnitudes may account for only 50-80% of the total flux in the most extreme cases (252)). For example, ref. (119) show that their UKIDSS Petrosian magnitudes can be up to 0.5 mag fainter than 2MASS Kron magnitudes. The fraction of the lost flux increases towards fainter galaxies and may cause a systematic underestimation of the faint-end luminosities as well as the luminosity density. ref. (253) provide a good analysis of the effects of different photometric systems used in surveys. They find an overdensity of faint galaxies when compared with the best-fit Schechter function irrespective of the aperture system

used and show that a Schechter function parametrization does not provide a good fit at the faint-end. They also show that the use of a photometric systems based on total magnitudes (e.g. Sérsic extrapolated) have a systematically steeper faint-end slope than photometric systems based on Kron or Petrosian magnitudes. They further show that the r-band Kron & Petrosian photometry underestimates the luminosity density by at least $\sim 15\%$ as they do not account for missing light. ref. (87) show that the difference of the luminosity density resulting from Petrosian and Sérsic magnitudes should be within <0.1 mag in the SDSS bands and not worth correcting for given the limitations of both systems. Still many authors apply a correction to estimate the total magnitudes in order to derive quantities such as the luminosity density in physical units (e.g. (121; 112; 117)). These can be as high as 0.3 mag in the K-band. It seems that uncertainties in the LF may be dominated by the aperture governing the fraction of flux recovered, especially at the faint end.

A.2.0.3 Luminosity Function Estimators

In this paper we use LFs derived from a variety of different LF estimators. The choice of LF estimator is unlikely to be a major source of discrepancy between the LFs derived by different authors although it can lead to different combinations of the Schechter parameters. The most commonly used methods are i) the $1/V_{max}$ method (254), ii) the Sandage-Tammann-Yahil maximum likelihood method (STY) (255) and iii) the StepWise maximum Likelihood Method (SWLM) (256). The $1/V_{max}$ method is reliable in the sense that it simultaneously gives the shape and

normalization of the LF requiring no assumption on the parametric form for the LF. However, it suffers from systematic biases in the presence of density inhomogeneities in the observed field. The STY method is typically preferred when estimating the LF over multiple fields since it has been shown to be unbiased to large scale structure and does not require binning of the data (256). It does however require an assumption of a functional form of the luminosity function. The SWML method is widely used since it makes no assumption of the LF shape while still being insensitive to large scale structure. ref. (257) compare the properties of each LF estimator and show how different LF estimators tend to be biased towards the faint-end either overestimating or underestimating the slope, depending on the estimator and the underlying catalog. In order to minimize such effects one routinely compares the outputs of more than one method (e.g. 100; 107; 124).

Bibliography

- [1] R. B. Partridge and P. J. E. Peebles. Are Young Galaxies Visible? II. The Integrated Background. *ApJ*, 148:377–+, May 1967.
- [2] G. Lemaître. Un Univers homogène de masse constante et de rayon croissant rendant compte de la vitesse radiale des nébuleuses extra-galactiques. *Annales de la Societe Scietifique de Bruxelles*, 47:49–59, 1927.
- [3] E. Hubble. A Relation between Distance and Radial Velocity among Extra-Galactic Nebulae. *Proceedings of the National Academy of Science*, 15:168–173, March 1929.
- [4] G. Lemaître. Expansion of the universe, A homogeneous universe of constant mass and increasing radius accounting for the radial velocity of extra-galactic nebulae. *MNRAS*, 91:483–490, March 1931.
- [5] S. Weinberg. *Gravitation and Cosmology: Principles and Applications of the General Theory of Relativity*. July 1972.
- [6] P. J. E. Peebles. *Principles of Physical Cosmology*. 1993.
- [7] J. A. Peacock. *Cosmological Physics*. January 1999.
- [8] J. M. Bardeen, J. R. Bond, N. Kaiser, and A. S. Szalay. The statistics of peaks of Gaussian random fields. *ApJ*, 304:15–61, May 1986.
- [9] J. A. Peacock and S. J. Dodds. Non-linear evolution of cosmological power spectra. *MNRAS*, 280:L19–L26, June 1996.
- [10] W. H. Press and P. Schechter. Formation of Galaxies and Clusters of Galaxies by Self-Similar Gravitational Condensation. *ApJ*, 187:425–438, February 1974.
- [11] G. B. Rybicki and A. P. Lightman. *Radiative processes in astrophysics*. 1979.
- [12] J. B. Oke and J. E. Gunn. Secondary standard stars for absolute spectrophotometry. *ApJ*, 266:713–717, March 1983.
- [13] A. Kashlinsky. Cosmic infrared background and early galaxy evolution [review article]. *Phys. Rep.*, 409:361–438, April 2005.

- [14] D. T. Hill, S. P. Driver, E. Cameron, N. Cross, J. Liske, and A. Robotham. The ugrizYJHK luminosity distributions and densities from the combined MGC, SDSS and UKIDSS LAS data sets. *MNRAS*, 404:1215–1230, May 2010.
- [15] D. N. Limber. The Analysis of Counts of the Extragalactic Nebulae in Terms of a Fluctuating Density Field. *ApJ*, 117:134, January 1953.
- [16] M. G. Hauser, R. G. Arendt, T. Kelsall, E. Dwek, N. Odegard, J. L. Weiland, H. T. Freudenreich, W. T. Reach, R. F. Silverberg, S. H. Moseley, Y. C. Pei, P. Lubin, J. C. Mather, R. A. Shafer, G. F. Smoot, R. Weiss, D. T. Wilkinson, and E. L. Wright. The COBE Diffuse Infrared Background Experiment Search for the Cosmic Infrared Background. I. Limits and Detections. *ApJ*, 508:25–43, November 1998.
- [17] T. Kelsall, J. L. Weiland, B. A. Franz, W. T. Reach, R. G. Arendt, E. Dwek, H. T. Freudenreich, M. G. Hauser, S. H. Moseley, N. P. Odegard, R. F. Silverberg, and E. L. Wright. The COBE Diffuse Infrared Background Experiment Search for the Cosmic Infrared Background. II. Model of the Interplanetary Dust Cloud. *ApJ*, 508:44–73, November 1998.
- [18] R. G. Arendt, N. Odegard, J. L. Weiland, T. J. Sodroski, M. G. Hauser, E. Dwek, T. Kelsall, S. H. Moseley, R. F. Silverberg, D. Leisawitz, K. Mitchell, W. T. Reach, and E. L. Wright. The COBE Diffuse Infrared Background Experiment Search for the Cosmic Infrared Background. III. Separation of Galactic Emission from the Infrared Sky Brightness. *ApJ*, 508:74–105, November 1998.
- [19] E. Dwek, R. G. Arendt, M. G. Hauser, D. Fixsen, T. Kelsall, D. Leisawitz, Y. C. Pei, E. L. Wright, J. C. Mather, S. H. Moseley, N. Odegard, R. Shafer, R. F. Silverberg, and J. L. Weiland. The COBE Diffuse Infrared Background Experiment Search for the Cosmic Infrared Background. IV. Cosmological Implications. *ApJ*, 508:106–122, November 1998.
- [20] E. Dwek and R. G. Arendt. A Tentative Detection of the Cosmic Infrared Background at 3.5 μm from COBE/DIRBE Observations. *ApJ*, 508:L9–L12, November 1998.
- [21] V. Gorjian, E. L. Wright, and R. R. Chary. Tentative Detection of the Cosmic Infrared Background at 2.2 and 3.5 Microns Using Ground-based and Space-based Observations. *ApJ*, 536:550–560, June 2000.
- [22] E. L. Wright and E. D. Reese. Detection of the Cosmic Infrared Background at 2.2 and 3.5 Microns Using DIRBE Observations. *ApJ*, 545:43–55, December 2000.
- [23] L. Cambr esy, W. T. Reach, C. A. Beichman, and T. H. Jarrett. The Cosmic Infrared Background at 1.25 and 2.2 Microns Using DIRBE and 2MASS: A Contribution Not Due to Galaxies? *ApJ*, 555:563–571, July 2001.

- [24] T. Matsumoto, S. Matsuura, H. Murakami, M. Tanaka, M. Freund, M. Lim, M. Cohen, M. Kawada, and M. Noda. Infrared Telescope in Space Observations of the Near-Infrared Extragalactic Background Light. *ApJ*, 626:31–43, June 2005.
- [25] K. Tsumura, T. Matsumoto, S. Matsuura, I. Sakon, and T. Wada. Low-Resolution Spectrum of the Extragalactic Background Light with AKARI Infrared Camera. *ArXiv e-prints*, July 2013.
- [26] T. Totani, Y. Yoshii, F. Iwamuro, T. Maihara, and K. Motohara. Diffuse Extragalactic Background Light versus Deep Galaxy Counts in the Subaru Deep Field: Missing Light in the Universe? *ApJ*, 550:L137–L141, April 2001.
- [27] M. R. Santos, V. Bromm, and M. Kamionkowski. The contribution of the first stars to the cosmic infrared background. *MNRAS*, 336:1082–1092, November 2002.
- [28] R. Salvaterra and A. Ferrara. The imprint of the cosmic dark ages on the near-infrared background. *MNRAS*, 339:973–982, March 2003.
- [29] E. Dwek, R. G. Arendt, and F. Krennrich. The Near-Infrared Background: Interplanetary Dust or Primordial Stars? *ApJ*, 635:784–794, December 2005.
- [30] P. Madau and J. Silk. Population III and the near-infrared background excess. *MNRAS*, 359:L37–L41, May 2005.
- [31] K. Mattila. The 1- μm discontinuity in the extragalactic background light spectrum: an artefact of foreground subtraction. *MNRAS*, 372:1253–1258, November 2006.
- [32] R. C. Keenan, A. J. Barger, L. L. Cowie, and W.-H. Wang. The Resolved Near-infrared Extragalactic Background. *ApJ*, 723:40–46, November 2010.
- [33] P. Madau and L. Pozzetti. Deep galaxy counts, extragalactic background light and the stellar baryon budget. *MNRAS*, 312:L9–L15, February 2000.
- [34] G. G. Fazio, M. L. N. Ashby, P. Barmby, J. L. Hora, J.-S. Huang, M. A. Pahre, Z. Wang, S. P. Willner, R. G. Arendt, S. H. Moseley, M. Brodwin, P. Eisenhardt, D. Stern, E. V. Tollestrup, and E. L. Wright. Number Counts at $3 \mu\text{m} < \lambda < 10 \mu\text{m}$ from the Spitzer Space Telescope. *ApJS*, 154:39–43, September 2004.
- [35] M. L. N. Ashby, S. P. Willner, G. G. Fazio, J.-S. Huang, R. Arendt, P. Barmby, G. Barro, E. F. Bell, R. Bouwens, A. Cattaneo, D. Croton, R. Davé, J. S. Dunlop, E. Egami, S. Faber, K. Finlator, N. A. Grogin, P. Guhathakurta, L. Hernquist, J. L. Hora, G. Illingworth, A. Kashlinsky, A. M. Koekemoer, D. C. Koo, I. Labbé, Y. Li, L. Lin, H. Moseley, K. Nandra, J. Newman, K. Noeske, M. Ouchi, M. Peth, D. Rigopoulou, B. Robertson, V. Sarajedini, L. Simard,

- H. A. Smith, Z. Wang, R. Wechsler, B. Weiner, G. Wilson, S. Wuyts, T. Yamada, and H. Yan. SEDS: The Spitzer Extended Deep Survey. Survey Design, Photometry, and Deep IRAC Source Counts. *ApJ*, 769:80, May 2013.
- [36] AI. Nikishov. . *JETP*, 14:393–94, January 1962.
- [37] F. W. Stecker. Cosmic gamma rays. *NASA Special Publication*, 249, 1971.
- [38] F. W. Stecker, M. A. Malkan, and S. T. Scully. Intergalactic Photon Spectra from the Far-IR to the UV Lyman Limit for $0 < z < 6$ and the Optical Depth of the Universe to High-Energy Gamma Rays. *ApJ*, 648:774–783, September 2006.
- [39] A. Franceschini, G. Rodighiero, and M. Vaccari. Extragalactic optical-infrared background radiation, its time evolution and the cosmic photon-photon opacity. *A&A*, 487:837–852, September 2008.
- [40] T. M. Kneiske and H. Dole. A lower-limit flux for the extragalactic background light. *A&A*, 515:A19, June 2010.
- [41] A. Domínguez, J. R. Primack, D. J. Rosario, F. Prada, R. C. Gilmore, S. M. Faber, D. C. Koo, R. S. Somerville, M. A. Pérez-Torres, P. Pérez-González, J.-S. Huang, M. Davis, P. Guhathakurta, P. Barmby, C. J. Conselice, M. Lozano, J. A. Newman, and M. C. Cooper. Extragalactic background light inferred from AEGIS galaxy-SED-type fractions. *MNRAS*, 410:2556–2578, February 2011.
- [42] F. Aharonian, A. G. Akhperjanian, A. R. Bazer-Bachi, M. Beilicke, W. Benbow, D. Berge, K. Bernlöhr, C. Boisson, O. Bolz, V. Borrel, I. Braun, F. Breitling, A. M. Brown, P. M. Chadwick, L.-M. Chounet, R. Cornils, L. Costamante, B. Degrange, H. J. Dickinson, A. Djannati-Ataï, L. O. Drury, G. Dubus, D. Emmanoulopoulos, P. Espigat, F. Feinstein, G. Fontaine, Y. Fuchs, S. Funk, Y. A. Gallant, B. Giebels, S. Gillessen, J. F. Glicenstein, P. Goret, C. Hadjichristidis, D. Hauser, M. Hauser, G. Heinzlmann, G. Henri, G. Hermann, J. A. Hinton, W. Hofmann, M. Holleran, D. Horns, A. Jacholkowska, O. C. de Jager, B. Khélifi, S. Klages, N. Komin, A. Konopelko, I. J. Latham, R. Le Gallou, A. Lemièrre, M. Lemoine-Goumard, N. Leroy, T. Lohse, J. M. Martin, O. Martineau-Huynh, A. Marcowith, C. Masterson, T. J. L. McComb, M. de Naurois, S. J. Nolan, A. Noutsos, K. J. Orford, J. L. Osborne, M. Ouchrif, M. Panter, G. Pelletier, S. Pita, G. Pühlhofer, M. Punch, B. C. Raubenheimer, M. Raue, J. Raux, S. M. Rayner, A. Reimer, O. Reimer, J. Ripken, L. Rob, L. Rolland, G. Rowell, V. Sahakian, L. Saugé, S. Schlenker, R. Schlickeiser, C. Schuster, U. Schwanke, M. Siewert, H. Sol, D. Spangler, R. Steenkamp, C. Stegmann, J.-P. Tavernet, R. Terrier, C. G. Théoret, M. Tluczykont, C. van Eldik, G. Vasileiadis, C. Venter, P. Vincent, H. J. Völk, and S. J. Wagner. A low level of extragalactic background light as revealed by γ -rays from blazars. *Nature*, 440:1018–1021, April 2006.

- [43] D. Mazin and M. Raue. New limits on the density of the extragalactic background light in the optical to the far infrared from the spectra of all known TeV blazars. *A&A*, 471:439–452, August 2007.
- [44] M. Meyer, M. Raue, D. Mazin, and D. Horns. Limits on the extragalactic background light in the Fermi era. *A&A*, 542:A59, June 2012.
- [45] M. R. Orr, F. Krennrich, and E. Dwek. Strong New Constraints on the Extragalactic Background Light in the Near- to Mid-infrared. *ApJ*, 733:77, June 2011.
- [46] Y. Inoue, S. Inoue, M. A. R. Kobayashi, R. Makiya, Y. Niino, and T. Totani. Extragalactic Background Light from Hierarchical Galaxy Formation: Gamma-Ray Attenuation up to the Epoch of Cosmic Reionization and the First Stars. *ApJ*, 768:197, May 2013.
- [47] Ackermann et al. The Imprint of the Extragalactic Background Light in the Gamma-Ray Spectra of Blazars. *Science*, 338:1190–, November 2012.
- [48] H.E.S.S. Collaboration. Measurement of the extragalactic background light imprint on the spectra of the brightest blazars observed with H.E.S.S. *A&A*, 550:A4, February 2013.
- [49] A. Domínguez, J. D. Finke, F. Prada, J. R. Primack, F. S. Kitaura, B. Siana, and D. Paneque. Detection of the Cosmic γ -Ray Horizon from Multiwavelength Observations of Blazars. *ApJ*, 770:77, June 2013.
- [50] W. Essey and A. Kusenko. A new interpretation of the gamma-ray observations of distant active galactic nuclei. *Astroparticle Physics*, 33:81–85, March 2010.
- [51] Y. Inoue, O. E. Kalashev, and A. Kusenko. Prospects for future very high-energy gamma-ray sky survey: Impact of secondary gamma rays. *Astroparticle Physics*, 54:118–124, February 2014.
- [52] A. Kashlinsky, J. C. Mather, S. Odenwald, and M. G. Hauser. Clustering of the Diffuse Infrared Light from the COBE DIRBE Maps. I. C(0) and Limits on the Near-Infrared Background. *ApJ*, 470:681–+, October 1996.
- [53] J. Pyo, T. Matsumoto, W.-S. Jeong, and S. Matsuura. Brightness and Fluctuation of the Mid-infrared Sky from AKARI Observations toward the North Ecliptic Pole. *ApJ*, 760:102, December 2012.
- [54] A. Kashlinsky, R. G. Arendt, J. Mather, and S. H. Moseley. Tracing the first stars with fluctuations of the cosmic infrared background. *Nature*, 438:45–50, November 2005.
- [55] T. N. Gautier, III, F. Boulanger, M. Perault, and J. L. Puget. A calculation of confusion noise due to infrared cirrus. *AJ*, 103:1313–1324, April 1992.

- [56] J. G. Ingalls, M.-A. Miville-Deschênes, W. T. Reach, A. Noriega-Crespo, S. J. Carey, F. Boulanger, S. R. Stolovy, D. L. Padgett, M. J. Burgdorf, S. B. Fajardo-Acosta, W. J. Glaccum, G. Helou, D. W. Hoard, J. Karr, J. O’Linger, L. M. Rebull, J. Rho, J. R. Stauffer, and S. Wachter. Structure and Colors of Diffuse Emission in the Spitzer Galactic First Look Survey. *ApJS*, 154:281–285, September 2004.
- [57] M.-A. Miville-Deschênes, G. Lagache, F. Boulanger, and J.-L. Puget. Statistical properties of dust far-infrared emission. *A&A*, 469:595–605, July 2007.
- [58] F. J. Lockman, K. Jahoda, and D. McCammon. The structure of galactic HI in directions of low total column density. *ApJ*, 302:432–449, March 1986.
- [59] A. Kashlinsky and S. Odenwald. Clustering of the Diffuse Infrared Light from the COBE DIRBE Maps. III. Power Spectrum Analysis and Excess Isotropic Component of Fluctuations. *ApJ*, 528:74–95, January 2000.
- [60] A. Kashlinsky, S. Odenwald, J. Mather, M. F. Skrutskie, and R. M. Cutri. Detection of Small-Scale Fluctuations in the Near-Infrared Cosmic Infrared Background from Long-Exposure 2MASS Fields. *ApJ*, 579:L53–L57, November 2002.
- [61] S. Odenwald, A. Kashlinsky, J. C. Mather, M. F. Skrutskie, and R. M. Cutri. Analysis of the Diffuse Near-Infrared Emission from Two-Micron All-Sky Survey Deep Integration Data: Foregrounds versus the Cosmic Infrared Background. *ApJ*, 583:535–550, February 2003.
- [62] A. Kashlinsky, R. G. Arendt, J. Mather, and S. H. Moseley. New Measurements of Cosmic Infrared Background Fluctuations from Early Epochs. *ApJ*, 654:L5–L8, January 2007.
- [63] R. I. Thompson, D. Eisenstein, X. Fan, M. Rieke, and R. C. Kennicutt. Constraints on the Cosmic Near-Infrared Background Excess from NICMOS Deep Field Observations. *ApJ*, 657:669–680, March 2007.
- [64] R. I. Thompson, D. Eisenstein, X. Fan, M. Rieke, and R. C. Kennicutt. Evidence for a $z < 8$ Origin of the Source-subtracted Near-Infrared Background. *ApJ*, 666:658–662, September 2007.
- [65] T. Matsumoto, H. J. Seo, W.-S. Jeong, H. M. Lee, S. Matsuura, H. Matsuhara, S. Oyabu, J. Pyo, and T. Wada. AKARI Observation of the Fluctuation of the Near-infrared Background. *ApJ*, 742:124, December 2011.
- [66] A. Kashlinsky, R. G. Arendt, M. L. N. Ashby, G. G. Fazio, J. Mather, and S. H. Moseley. New Measurements of the Cosmic Infrared Background Fluctuations in Deep Spitzer/IRAC Survey Data and Their Cosmological Implications. *ApJ*, 753:63, July 2012.

- [67] A. Cooray, J. Smidt, F. de Bernardis, Y. Gong, D. Stern, M. L. N. Ashby, P. Eisenhardt, C. C. Frazer, A. H. Gonzalez, C. S. Kochanek, S. Kozlowski, and E. L. Wright. Near-infrared background anisotropies from diffuse intrahalo light of galaxies. *Nature*, 490:514–516, October 2012.
- [68] R. Salvaterra, M. Magliocchetti, A. Ferrara, and R. Schneider. The infrared glow of the first stars. *MNRAS*, 368:L6–L9, May 2006.
- [69] A. Kashlinsky, R. G. Arendt, J. Mather, and S. H. Moseley. On the Nature of the Sources of the Cosmic Infrared Background. *ApJ*, 654:L1–L4, February 2007.
- [70] E. R. Fernandez, E. Komatsu, I. T. Iliev, and P. R. Shapiro. The Cosmic Near-Infrared Background. II. Fluctuations. *ApJ*, 710:1089–1110, February 2010.
- [71] A. Cooray, Y. Gong, J. Smidt, and M. G. Santos. The Near-infrared Background Intensity and Anisotropies during the Epoch of Reionization. *ApJ*, 756:92, September 2012.
- [72] B. Yue, A. Ferrara, R. Salvaterra, and X. Chen. The contribution of high-redshift galaxies to the near-infrared background. *MNRAS*, 431:383–393, May 2013.
- [73] K. Helgason, M. Ricotti, and A. Kashlinsky. Reconstructing the Near-infrared Background Fluctuations from Known Galaxy Populations Using Multiband Measurements of Luminosity Functions. *ApJ*, 752:113, June 2012.
- [74] A. Kashlinsky, R. Arendt, J. P. Gardner, J. C. Mather, and S. H. Moseley. Detecting Population III Stars through Observations of Near-Infrared Cosmic Infrared Background Anisotropies. *ApJ*, 608:1–9, June 2004.
- [75] A. Cooray, J. J. Bock, B. Keatin, A. E. Lange, and T. Matsumoto. First Star Signature in Infrared Background Anisotropies. *ApJ*, 606:611–624, May 2004.
- [76] A. Kashlinsky, R. G. Arendt, J. Mather, and S. H. Moseley. Demonstrating the Negligible Contribution of Optical HST ACS Galaxies to Source-subtracted Cosmic Infrared Background Fluctuations in Deep Spitzer IRAC Images. *ApJ*, 666:L1–L4, September 2007.
- [77] N. Cappelluti, A. Kashlinsky, R. G. Arendt, A. Comastri, G. G. Fazio, A. Finoguenov, G. Hasinger, J. C. Mather, T. Miyaji, and S. H. Moseley. Cross-correlating Cosmic Infrared and X-Ray Background Fluctuations: Evidence of Significant Black Hole Populations among the CIB Sources. *ApJ*, 769:68, May 2013.
- [78] R. G. Arendt, A. Kashlinsky, S. H. Moseley, and J. Mather. Cosmic Infrared Background Fluctuations in Deep Spitzer Infrared Array Camera Images: Data Processing and Analysis. *ApJS*, 186:10–47, January 2010.

- [79] B. Yue, A. Ferrara, R. Salvaterra, Y. Xu, and X. Chen. Infrared background signatures of the first black holes. *MNRAS*, 433:1556–1566, August 2013.
- [80] R. Jimenez and A. Kashlinsky. Galaxy Evolution, Deep Galaxy Counts, and the Near-Infrared Cosmic Infrared Background. *ApJ*, 511:16–33, January 1999.
- [81] R. C. Gilmore, F. Prada, and J. Primack. Modelling gamma-ray burst observations by Fermi and MAGIC including attenuation due to diffuse background light. *MNRAS*, 402:565–574, February 2010.
- [82] Q. Guo, S. White, M. Boylan-Kolchin, G. De Lucia, G. Kauffmann, G. Lemson, C. Li, V. Springel, and S. Weinmann. From dwarf spheroidals to cD galaxies: simulating the galaxy population in a Λ CDM cosmology. *MNRAS*, 413:101–131, May 2011.
- [83] P. Schechter. An analytic expression for the luminosity function for galaxies. *ApJ*, 203:297–306, January 1976.
- [84] R. Johnston. Shedding light on the galaxy luminosity function. *A&A Rev.*, 19:41, August 2011.
- [85] G. Bruzual and S. Charlot. Stellar population synthesis at the resolution of 2003. *MNRAS*, 344:1000–1028, October 2003.
- [86] D. H. Jones, B. A. Peterson, M. Colless, and W. Saunders. Near-infrared and optical luminosity functions from the 6dF Galaxy Survey. *MNRAS*, 369:25–42, June 2006.
- [87] M. R. Blanton, D. W. Hogg, N. A. Bahcall, J. Brinkmann, M. Britton, A. J. Connolly, I. Csabai, M. Fukugita, J. Loveday, A. Meiksin, J. A. Munn, R. C. Nichol, S. Okamura, T. Quinn, D. P. Schneider, K. Shimasaku, M. A. Strauss, M. Tegmark, M. S. Vogeley, and D. H. Weinberg. The Galaxy Luminosity Function and Luminosity Density at Redshift $z = 0.1$. *ApJ*, 592:819–838, August 2003.
- [88] A. D. Montero-Dorta and F. Prada. The SDSS DR6 luminosity functions of galaxies. *MNRAS*, 399:1106–1118, November 2009.
- [89] M. R. Blanton, D. Eisenstein, D. W. Hogg, D. J. Schlegel, and J. Brinkmann. Relationship between Environment and the Broadband Optical Properties of Galaxies in the Sloan Digital Sky Survey. *ApJ*, 629:143–157, August 2005.
- [90] T. S. R. Babbedge, M. Rowan-Robinson, M. Vaccari, J. A. Surace, C. J. Lonsdale, D. L. Clements, F. Fang, D. Farrah, A. Franceschini, E. Gonzalez-Solares, E. Hatziminaoglou, C. G. Lacey, S. Oliver, N. Onyett, I. Pérez-Fournon, M. Polletta, F. Pozzi, G. Rodighiero, D. L. Shupe, B. Siana, and H. E. Smith. Luminosity functions for galaxies and quasars in the Spitzer

Wide-area Infrared Extragalactic Legacy Survey. MNRAS, 370:1159–1180, August 2006.

- [91] B. Magnelli, D. Elbaz, R. R. Chary, M. Dickinson, D. Le Borgne, D. T. Frayer, and C. N. A. Willmer. Evolution of the dusty infrared luminosity function from $z = 0$ to $z = 2.3$ using observations from Spitzer. A&A, 528:A35, April 2011.
- [92] S. Arnouts, D. Schiminovich, O. Ilbert, L. Tresse, B. Milliard, M. Treyer, S. Bardelli, T. Budavari, T. K. Wyder, E. Zucca, O. Le Fèvre, D. C. Martin, G. Vettolani, C. Adami, M. Arnaboldi, T. Barlow, L. Bianchi, M. Bolzonella, D. Bottini, Y.-I. Byun, A. Cappi, S. Charlot, T. Contini, J. Donas, K. Forster, S. Foucaud, P. Franzetti, P. G. Friedman, B. Garilli, I. Gavignaud, L. Guzzo, T. M. Heckman, C. Hoopes, A. Iovino, P. Jelinsky, V. Le Brun, Y.-W. Lee, D. Maccagni, B. F. Madore, R. Malina, B. Marano, C. Marinoni, H. J. McCracken, A. Mazure, B. Meneux, R. Merighi, P. Morrissey, S. Neff, S. Paltani, R. Pellò, J. P. Picat, A. Pollo, L. Pozzetti, M. Radovich, R. M. Rich, R. Scaramella, M. Scodreggio, M. Seibert, O. Siegmund, T. Small, A. S. Szalay, B. Welsh, C. K. Xu, G. Zamorani, and A. Zanichelli. The GALEX VIMOS-VLT Deep Survey Measurement of the Evolution of the 1500 Å Luminosity Function. ApJ, 619:L43–L46, January 2005.
- [93] T. K. Wyder, M. A. Treyer, B. Milliard, D. Schiminovich, S. Arnouts, T. Budavari, T. A. Barlow, L. Bianchi, Y.-I. Byun, J. Donas, K. Forster, P. G. Friedman, T. M. Heckman, P. N. Jelinsky, Y.-W. Lee, B. F. Madore, R. F. Malina, D. C. Martin, P. Morrissey, S. G. Neff, R. M. Rich, O. H. W. Siegmund, T. Small, A. S. Szalay, and B. Y. Welsh. The Ultraviolet Galaxy Luminosity Function in the Local Universe from GALEX Data. ApJ, 619:L15–L18, January 2005.
- [94] P. A. Oesch, R. J. Bouwens, C. M. Carollo, G. D. Illingworth, D. Magee, M. Trenti, M. Stiavelli, M. Franx, I. Labbé, and P. G. van Dokkum. The Evolution of the Ultraviolet Luminosity Function from $z \sim 0.75$ to $z \sim 2.5$ Using HST ERS WFC3/UVIS Observations. ApJ, 725:L150–L155, December 2010.
- [95] P. A. Oesch, R. J. Bouwens, G. D. Illingworth, V. Gonzalez, M. Trenti, P. G. van Dokkum, M. Franx, I. Labbe, C. M. Carollo, and D. Magee. The Bright End of the UV Luminosity Function at $z \sim 8$: New Constraints from CANDELS Data. *ArXiv e-prints*, January 2012.
- [96] N. A. Reddy, C. C. Steidel, M. Pettini, K. L. Adelberger, A. E. Shapley, D. K. Erb, and M. Dickinson. Multiwavelength Constraints on the Cosmic Star Formation History from Spectroscopy: the Rest-Frame Ultraviolet, H α , and Infrared Luminosity Functions at Redshifts $1.9 < z < 3.4$. ApJS, 175:48–85, March 2008.

- [97] M. Yoshida, K. Shimasaku, N. Kashikawa, M. Ouchi, S. Okamura, M. Ajiki, M. Akiyama, H. Ando, K. Aoki, M. Doi, H. Furusawa, T. Hayashino, F. Iwamuro, M. Iye, H. Karoji, N. Kobayashi, K. Kodaira, T. Kodama, Y. Komiyama, M. A. Malkan, Y. Matsuda, S. Miyazaki, Y. Mizumoto, T. Morokuma, K. Motohara, T. Murayama, T. Nagao, K. Nariai, K. Ohta, T. Sasaki, Y. Sato, K. Sekiguchi, Y. Shioya, H. Tamura, Y. Taniguchi, M. Umemura, T. Yamada, and N. Yasuda. Luminosity Functions of Lyman Break Galaxies at $z \sim 4$ and $z \sim 5$ in the Subaru Deep Field. *ApJ*, 653:988–1003, December 2006.
- [98] R. J. McLure, M. Cirasuolo, J. S. Dunlop, S. Foucaud, and O. Almaini. The luminosity function, halo masses and stellar masses of luminous Lyman-break galaxies at redshifts $5 < z < 6$. *MNRAS*, 395:2196–2209, June 2009.
- [99] M. Ouchi, B. Mobasher, K. Shimasaku, H. C. Ferguson, S. M. Fall, Y. Ono, N. Kashikawa, T. Morokuma, K. Nakajima, S. Okamura, M. Dickinson, M. Giavalisco, and K. Ohta. Large Area Survey for $z = 7$ Galaxies in SDF and GOODS-N: Implications for Galaxy Formation and Cosmic Reionization. *ApJ*, 706:1136–1151, December 2009.
- [100] R. J. Bouwens, G. D. Illingworth, M. Franx, and H. Ford. UV Luminosity Functions at $z \sim 4$, 5, and 6 from the Hubble Ultra Deep Field and Other Deep Hubble Space Telescope ACS Fields: Evolution and Star Formation History. *ApJ*, 670:928–958, December 2007.
- [101] R. J. Bouwens, G. D. Illingworth, P. A. Oesch, I. Labbé, M. Trenti, P. van Dokkum, M. Franx, M. Stiavelli, C. M. Carollo, D. Magee, and V. Gonzalez. Ultraviolet Luminosity Functions from $132 z \sim 7$ and $z \sim 8$ Lyman-break Galaxies in the Ultra-deep HUDF09 and Wide-area Early Release Science WFC3/IR Observations. *ApJ*, 737:90–+, August 2011.
- [102] A. Gabasch, R. Bender, S. Seitz, U. Hopp, R. P. Saglia, G. Feulner, J. Snigula, N. Drory, I. Appenzeller, J. Heidt, D. Mehlert, S. Noll, A. Böhm, K. Jäger, B. Ziegler, and K. J. Fricke. The evolution of the luminosity functions in the FORS Deep Field from low to high redshift. I. The blue bands. *A&A*, 421:41–58, July 2004.
- [103] I. K. Baldry, K. Glazebrook, T. Budavári, D. J. Eisenstein, J. Annis, N. A. Bahcall, M. R. Blanton, J. Brinkmann, I. Csabai, T. M. Heckman, H. Lin, J. Loveday, R. C. Nichol, and D. P. Schneider. The Sloan Digital Sky Survey u-band Galaxy Survey: luminosity functions and evolution. *MNRAS*, 358:441–456, April 2005.
- [104] S. M. Faber, C. N. A. Willmer, C. Wolf, D. C. Koo, B. J. Weiner, J. A. Newman, M. Im, A. L. Coil, C. Conroy, M. C. Cooper, M. Davis, D. P. Finkbeiner, B. F. Gerke, K. Gebhardt, E. J. Groth, P. Guhathakurta, J. Harker, N. Kaiser, S. Kassir, M. Kleinheinrich, N. P. Konidaris, R. G. Kron, L. Lin, G. Luppino,

- D. S. Madgwick, K. Meisenheimer, K. G. Noeske, A. C. Phillips, V. L. Sarajedini, R. P. Schiavon, L. Simard, A. S. Szalay, N. P. Vogt, and R. Yan. Galaxy Luminosity Functions to $z \sim 1$ from DEEP2 and COMBO-17: Implications for Red Galaxy Formation. *ApJ*, 665:265–294, August 2007.
- [105] P. Norberg, S. Cole, C. M. Baugh, C. S. Frenk, I. Baldry, J. Bland-Hawthorn, T. Bridges, R. Cannon, M. Colless, C. Collins, W. Couch, N. J. G. Cross, G. Dalton, R. De Propris, S. P. Driver, G. Efstathiou, R. S. Ellis, K. Glazebrook, C. Jackson, O. Lahav, I. Lewis, S. Lumsden, S. Maddox, D. Madgwick, J. A. Peacock, B. A. Peterson, W. Sutherland, and K. Taylor. The 2dF Galaxy Redshift Survey: the b_J -band galaxy luminosity function and survey selection function. *MNRAS*, 336:907–931, November 2002.
- [106] J. Loveday, P. Norberg, I. K. Baldry, S. P. Driver, A. M. Hopkins, J. A. Peacock, S. P. Bamford, J. Liske, J. Bland-Hawthorn, S. Brough, M. J. I. Brown, E. Cameron, C. J. Conselice, S. M. Croom, C. S. Frenk, M. Gunawardhana, D. T. Hill, D. H. Jones, L. S. Kelvin, K. Kuijken, R. C. Nichol, H. R. Parkinson, S. Phillipps, K. A. Pimbblet, C. C. Popescu, M. Prescott, A. S. G. Robotham, R. G. Sharp, W. J. Sutherland, E. N. Taylor, D. Thomas, R. J. Tuffs, E. van Kampen, and D. Wijesinghe. Galaxy and Mass Assembly (GAMA): ugriz galaxy luminosity functions. *MNRAS*, 420:1239–1262, February 2012.
- [107] O. Ilbert, L. Tresse, E. Zucca, S. Bardelli, S. Arnouts, G. Zamorani, L. Pozzetti, D. Bottini, B. Garilli, V. Le Brun, O. Le Fèvre, D. Maccagni, J.-P. Picat, R. Scaramella, M. Scodeggio, G. Vettolani, A. Zanicelli, C. Adami, M. Arnaboldi, M. Bolzonella, A. Cappi, S. Charlot, T. Contini, S. Foucaud, P. Franzetti, I. Gavignaud, L. Guzzo, A. Iovino, H. J. McCracken, B. Marano, C. Marinoni, G. Mathez, A. Mazure, B. Meneux, R. Merighi, S. Paltani, R. Pello, A. Pollo, M. Radovich, M. Bondi, A. Bongiorno, G. Busarello, P. Ciliegi, F. Lamareille, Y. Mellier, P. Merluzzi, V. Ripepi, and D. Rizzo. The VIMOS-VLT deep survey. Evolution of the galaxy luminosity function up to $z = 2$ in first epoch data. *A&A*, 439:863–876, September 2005.
- [108] A. Gabasch, U. Hopp, G. Feulner, R. Bender, S. Seitz, R. P. Saglia, J. Snigula, N. Drory, I. Appenzeller, J. Heidt, D. Mehlert, S. Noll, A. Böhm, K. Jäger, and B. Ziegler. The evolution of the luminosity functions in the FORS deep field from low to high redshift. II. The red bands. *A&A*, 448:101–121, March 2006.
- [109] D. Marchesini, P. van Dokkum, R. Quadri, G. Rudnick, M. Franx, P. Lira, S. Wuyts, E. Gawiser, D. Christlein, and S. Toft. The Rest-Frame Optical Luminosity Functions of Galaxies at $2 < z < 3.5$. *ApJ*, 656:42–65, February 2007.
- [110] D. Marchesini, M. Stefanon, G. B. Brammer, and K. E. Whitaker. The Evolution of the Rest-frame V-band Luminosity Function from $z = 4$: A Constant

- Faint-end Slope over the Last 12 Gyr of Cosmic History. *ApJ*, 748:126, April 2012.
- [111] T. Dahlen, B. Mobasher, R. S. Somerville, L. A. Moustakas, M. Dickinson, H. C. Ferguson, and M. Giavalisco. The Evolution of the Optical and Near-Infrared Galaxy Luminosity Functions and Luminosity Densities to $z \sim 2$. *ApJ*, 631:126–144, September 2005.
- [112] E. F. Bell, D. H. McIntosh, N. Katz, and M. D. Weinberg. The Optical and Near-Infrared Properties of Galaxies. I. Luminosity and Stellar Mass Functions. *ApJS*, 149:289–312, December 2003.
- [113] N. Kashikawa, T. Takata, Y. Ohya, M. Yoshida, T. Maihara, F. Iwamuro, K. Motohara, T. Totani, M. Nagashima, K. Shimasaku, H. Furusawa, M. Ouchi, M. Yagi, S. Okamura, M. Iye, T. Sasaki, G. Kosugi, K. Aoki, and F. Nakata. Subaru Deep Survey. III. Evolution of Rest-Frame Luminosity Functions Based on the Photometric Redshifts for a K'-Band-Selected Galaxy Sample. *AJ*, 125:53–65, January 2003.
- [114] M. Stefanon and D. Marchesini. The evolution of the rest-frame J- and H-band luminosity function of galaxies to $z=3.5$. *ArXiv e-prints*, November 2011.
- [115] L. Pozzetti, A. Cimatti, G. Zamorani, E. Daddi, N. Menci, A. Fontana, A. Renzini, M. Mignoli, F. Poli, P. Saracco, T. Broadhurst, S. Cristiani, S. D'Odorico, E. Giallongo, and R. Gilmozzi. The K20 survey. V. The evolution of the near-IR Luminosity Function. *A&A*, 402:837–848, May 2003.
- [116] G. Feulner, R. Bender, N. Drory, U. Hopp, J. Snigula, and G. J. Hill. The Munich Near-Infrared Cluster Survey - V. The evolution of the rest-frame K- and J-band galaxy luminosity functions to $z \sim 0.7$. *MNRAS*, 342:605–622, June 2003.
- [117] V. R. Eke, C. M. Baugh, S. Cole, C. S. Frenk, H. M. King, and J. A. Peacock. Where are the stars? *MNRAS*, 362:1233–1246, October 2005.
- [118] S. Cole, P. Norberg, C. M. Baugh, C. S. Frenk, J. Bland-Hawthorn, T. Bridges, R. Cannon, M. Colless, C. Collins, W. Couch, N. Cross, G. Dalton, R. De Propris, S. P. Driver, G. Efstathiou, R. S. Ellis, K. Glazebrook, C. Jackson, O. Lahav, I. Lewis, S. Lumsden, S. Maddox, D. Madgwick, J. A. Peacock, B. A. Peterson, W. Sutherland, and K. Taylor. The 2dF galaxy redshift survey: near-infrared galaxy luminosity functions. *MNRAS*, 326:255–273, September 2001.
- [119] A. J. Smith, J. Loveday, and N. J. G. Cross. Luminosity and surface brightness distribution of K-band galaxies from the UKIDSS Large Area Survey. *MNRAS*, 397:868–882, August 2009.

- [120] P. Saracco, A. Fiano, G. Chincarini, E. Vanzella, M. Longhetti, S. Cristiani, A. Fontana, E. Giallongo, and M. Nonino. Probing the evolution of the near-infrared luminosity function of galaxies to $z \sim 3$ in the Hubble Deep Field-South. *MNRAS*, 367:349–365, March 2006.
- [121] C. S. Kochanek, M. A. Pahre, E. E. Falco, J. P. Huchra, J. Mader, T. H. Jarrett, T. Chester, R. Cutri, and S. E. Schneider. The K-Band Galaxy Luminosity Function. *ApJ*, 560:566–579, October 2001.
- [122] J.-S. Huang, K. Glazebrook, L. L. Cowie, and C. Tinney. The Hawaii+Anglo-Australian Observatory K-Band Galaxy Redshift Survey. I. The Local K-Band Luminosity Function. *ApJ*, 584:203–209, February 2003.
- [123] S. Arnouts, C. J. Walcher, O. Le Fèvre, G. Zamorani, O. Ilbert, V. Le Brun, L. Pozzetti, S. Bardelli, L. Tresse, E. Zucca, S. Charlot, F. Lamareille, H. J. McCracken, M. Bolzonella, A. Iovino, C. Lonsdale, M. Polletta, J. Surace, D. Bottini, B. Garilli, D. Maccagni, J. P. Picat, R. Scaramella, M. Scodeggio, G. Vettolani, A. Zanichelli, C. Adami, A. Cappi, P. Ciliegi, T. Contini, S. de la Torre, S. Foucaud, P. Franzetti, I. Gavignaud, L. Guzzo, B. Marano, C. Marinoni, A. Mazure, B. Meneux, R. Merighi, S. Paltani, R. Pellò, A. Pollo, M. Radovich, S. Temporin, and D. Vergani. The SWIRE-VVDS-CFHTLS surveys: stellar mass assembly over the last 10 Gyr. Evidence for a major build up of the red sequence between $z = 2$ and $z = 1$. *A&A*, 476:137–150, December 2007.
- [124] M. Cirasuolo, R. J. McLure, J. S. Dunlop, O. Almaini, S. Foucaud, and C. Simpson. A new measurement of the evolving near-infrared galaxy luminosity function out to $z \sim 4$: a continuing challenge to theoretical models of galaxy formation. *MNRAS*, 401:1166–1176, January 2010.
- [125] X. Dai, R. J. Assef, C. S. Kochanek, M. Brodwin, M. J. I. Brown, N. Caldwell, R. J. Cool, A. Dey, P. Eisenhardt, D. Eisenstein, A. H. Gonzalez, B. T. Januzzi, C. Jones, S. S. Murray, and D. Stern. Mid-Infrared Galaxy Luminosity Functions from the AGN and Galaxy Evolution Survey. *ApJ*, 697:506–521, May 2009.
- [126] H. Lin, H. K. C. Yee, R. G. Carlberg, S. L. Morris, M. Sawicki, D. R. Patton, G. Wirth, and C. W. Shepherd. The CNOC2 Field Galaxy Luminosity Function. I. A Description of Luminosity Function Evolution. *ApJ*, 518:533–561, June 1999.
- [127] D. J. Schlegel, D. P. Finkbeiner, and M. Davis. Maps of Dust Infrared Emission for Use in Estimation of Reddening and Cosmic Microwave Background Radiation Foregrounds. *ApJ*, 500:525, June 1998.
- [128] J. A. Cardelli, G. C. Clayton, and J. S. Mathis. The relationship between infrared, optical, and ultraviolet extinction. *ApJ*, 345:245–256, October 1989.

- [129] R. Indebetouw, J. S. Mathis, B. L. Babler, M. R. Meade, C. Watson, B. A. Whitney, M. J. Wolff, M. G. Wolfire, M. Cohen, T. M. Bania, R. A. Benjamin, D. P. Clemens, J. M. Dickey, J. M. Jackson, H. A. Kobulnicky, A. P. Marston, E. P. Mercer, J. R. Stauffer, S. R. Stolovy, and E. Churchwell. The Wavelength Dependence of Interstellar Extinction from 1.25 to 8.0 μm Using GLIMPSE Data. *ApJ*, 619:931–938, February 2005.
- [130] D. W. Hogg, I. K. Baldry, M. R. Blanton, and D. J. Eisenstein. The K correction. *ArXiv Astrophysics e-prints*, October 2002.
- [131] M. Cirasuolo, R. J. McLure, J. S. Dunlop, O. Almaini, S. Foucaud, I. Smail, K. Sekiguchi, C. Simpson, S. Eales, S. Dye, M. G. Watson, M. J. Page, and P. Hirst. The evolution of the near-infrared galaxy luminosity function and colour bimodality up to $z \sim 2$ from the UKIDSS Ultra Deep Survey Early Data Release. *MNRAS*, 380:585–595, September 2007.
- [132] M. Ricotti, N. Y. Gnedin, and J. M. Shull. The Fate of the First Galaxies. I. Self-consistent Cosmological Simulations with Radiative Transfer. *ApJ*, 575:33–48, August 2002.
- [133] M. Ricotti, N. Y. Gnedin, and J. M. Shull. The Fate of the First Galaxies. II. Effects of Radiative Feedback. *ApJ*, 575:49–67, August 2002.
- [134] M. Ricotti, N. Y. Gnedin, and J. M. Shull. The Fate of the First Galaxies. III. Properties of Primordial Dwarf Galaxies and Their Impact on the Intergalactic Medium. *ApJ*, 685:21–39, September 2008.
- [135] M. S. Bovill and M. Ricotti. Pre-Reionization Fossils, Ultra-Faint Dwarfs, and the Missing Galactic Satellite Problem. *ApJ*, 693:1859–1870, March 2009.
- [136] M. S. Bovill and M. Ricotti. Where are the Fossils of the First Galaxies? I. Local Volume Maps and Properties of the Undetected Dwarfs. *ApJ*, 741:17, November 2011.
- [137] M. S. Bovill and M. Ricotti. Where are the Fossils of the First Galaxies? II. True Fossils, Ghost Halos, and the Missing Bright Satellites. *ApJ*, 741:18, November 2011.
- [138] P. Capak, L. L. Cowie, E. M. Hu, A. J. Barger, M. Dickinson, E. Fernandez, M. Giavalisco, Y. Komiyama, C. Kretchmer, C. McNally, S. Miyazaki, S. Okamura, and D. Stern. A Deep Wide-Field, Optical, and Near-Infrared Catalog of a Large Area around the Hubble Deep Field North. *AJ*, 127:180–198, January 2004.
- [139] P. Capak, H. Aussel, M. Ajiki, H. J. McCracken, B. Mobasher, N. Scoville, P. Shopbell, Y. Taniguchi, D. Thompson, S. Tribiano, S. Sasaki, A. W. Blain, M. Brusa, C. Carilli, A. Comastri, C. M. Carollo, P. Cassata, J. Colbert, R. S. Ellis, M. Elvis, M. Giavalisco, W. Green, L. Guzzo, G. Hasinger,

- O. Ilbert, C. Impey, K. Jahnke, J. Kartaltepe, J.-P. Kneib, J. Koda, A. Koeke-
moer, Y. Komiyama, A. Leauthaud, O. Le Fevre, S. Lilly, C. Liu, R. Massey,
S. Miyazaki, T. Murayama, T. Nagao, J. A. Peacock, A. Pickles, C. Por-
ciani, A. Renzini, J. Rhodes, M. Rich, M. Salvato, D. B. Sanders, C. Scarlata,
D. Schiminovich, E. Schinnerer, M. Scodeggio, K. Sheth, Y. Shioya, L. A. M.
Tasca, J. E. Taylor, L. Yan, and G. Zamorani. The First Release COSMOS
Optical and Near-IR Data and Catalog. *ApJS*, 172:99–116, September 2007.
- [140] H. J. McCracken, M. Radovich, E. Bertin, Y. Mellier, M. Dantel-Fort, O. Le
Fèvre, J. C. Cuillandre, S. Gwyn, S. Foucaud, and G. Zamorani. The VIRMOS
deep imaging survey. II: CFH12K BVRI optical data for the 0226-04 deep field.
A&A, 410:17–32, October 2003.
- [141] N. Yasuda, M. Fukugita, V. K. Narayanan, R. H. Lupton, I. Strateva, M. A.
Strauss, Ž. Ivezić, R. S. J. Kim, D. W. Hogg, D. H. Weinberg, K. Shimasaku,
J. Loveday, J. Annis, N. A. Bahcall, M. Blanton, J. Brinkmann, R. J. Brunner,
A. J. Connolly, I. Csabai, M. Doi, M. Hamabe, S.-I. Ichikawa, T. Ichikawa,
D. E. Johnston, G. R. Knapp, P. Z. Kunszt, D. Q. Lamb, T. A. McKay,
J. A. Munn, R. C. Nichol, S. Okamura, D. P. Schneider, G. P. Szokoly, M. S.
Vogeley, M. Watanabe, and D. G. York. Galaxy Number Counts from the
Sloan Digital Sky Survey Commissioning Data. *AJ*, 122:1104–1124, September
2001.
- [142] N. Kashikawa, K. Shimasaku, N. Yasuda, M. Ajiki, M. Akiyama, H. Ando,
K. Aoki, M. Doi, S. S. Fujita, H. Furusawa, T. Hayashino, F. Iwamuro, M. Iye,
H. Karoji, N. Kobayashi, K. Kodaira, T. Kodama, Y. Komiyama, Y. Mat-
suda, S. Miyazaki, Y. Mizumoto, T. Morokuma, K. Motohara, T. Murayama,
T. Nagao, K. Nariai, K. Ohta, S. Okamura, M. Ouchi, T. Sasaki, Y. Sato,
K. Sekiguchi, Y. Shioya, H. Tamura, Y. Taniguchi, M. Umemura, T. Yamada,
and M. Yoshida. The Subaru Deep Field: The Optical Imaging Data. *PASJ*,
56:1011–1023, December 2004.
- [143] P. Väisänen, E. V. Tollestrup, S. P. Willner, and M. Cohen. Wide-Field
J- and K-Band Galaxy Counts in the European Large-Area Infrared Space
Observatory Survey Fields. *ApJ*, 540:593–604, September 2000.
- [144] M. Dickinson. A complete NICMOS map of the Hubble Deep Field North.
In S. Holt and E. Smith, editors, *After the Dark Ages: When Galaxies were
Young (the Universe at $2 < Z < 5$)*, volume 470 of *American Institute of
Physics Conference Series*, pages 122–132, April 1999.
- [145] T. Maihara, F. Iwamuro, H. Tanabe, T. Taguchi, R. Hata, S. Oya,
N. Kashikawa, M. Iye, S. Miyazaki, H. Karoji, M. Yoshida, T. Totani,
Y. Yoshii, S. Okamura, K. Shimasaku, Y. Saito, H. Ando, M. Goto,
M. Hayashi, N. Kaifu, N. Kobayashi, G. Kosugi, K. Motohara, T. Nishimura,
J. Noumaru, R. Ogasawara, T. Sasaki, K. Sekiguchi, T. Takata, H. Terada,

- T. Yamashita, T. Usuda, and A. T. Tokunaga. Subaru Deep Survey I. Near-Infrared Observations. *PASJ*, 53:25–36, February 2001.
- [146] R. C. Keenan, L. Trouille, A. J. Barger, L. L. Cowie, and W.-H. Wang. An Extremely Deep, Wide-Field Near-Infrared Survey: Bright Galaxy Counts and Local Large Scale Structure. *ApJS*, 186:94–110, January 2010.
- [147] W. J. Frith, N. Metcalfe, and T. Shanks. New H-band galaxy number counts: a large local hole in the galaxy distribution. *MNRAS*, 371:1601–1609, October 2006.
- [148] R. I. Thompson, G. Illingworth, R. Bouwens, M. Dickinson, D. Eisenstein, X. Fan, M. Franx, A. Riess, M. J. Rieke, G. Schneider, E. Stobie, S. Toft, and P. van Dokkum. The Near-Infrared Camera and Multi-Object Spectrometer Ultra Deep Field: Observations, Data Reduction, and Galaxy Photometry. *AJ*, 130:1–12, July 2005.
- [149] N. Metcalfe, T. Shanks, P. M. Weilbacher, H. J. McCracken, R. Fong, and D. Thompson. Galaxy number counts - VI. An H-band survey of the Herschel Deep Field. *MNRAS*, 370:1257–1273, August 2006.
- [150] R. Quadri, D. Marchesini, P. van Dokkum, E. Gawiser, M. Franx, P. Lira, G. Rudnick, C. M. Urry, J. Maza, M. Kriek, L. F. Barrientos, G. A. Blanc, F. J. Castander, D. Christlein, P. S. Coppi, P. B. Hall, D. Herrera, L. Infante, E. N. Taylor, E. Treister, and J. P. Willis. The Multiwavelength Survey by Yale-Chile (MUSYC): Deep Near-Infrared Imaging and the Selection of Distant Galaxies. *AJ*, 134:1103–1117, September 2007.
- [151] A. J. Baker, R. I. Davies, M. D. Lehnert, N. A. Thatte, W. D. Vacca, O. R. Hainaut, M. J. Jarvis, G. K. Miley, and H. J. A. Röttgering. Galaxies in southern bright star fields. I. Near-infrared imaging. *A&A*, 406:593–601, August 2003.
- [152] Y. Minowa, N. Kobayashi, Y. Yoshii, T. Totani, T. Maihara, F. Iwamuro, H. Takami, N. Takato, Y. Hayano, H. Terada, S. Oya, M. Iye, and A. T. Tokunaga. Subaru Super Deep Field with Adaptive Optics. I. Observations and First Implications. *ApJ*, 629:29–44, August 2005.
- [153] J.-S. Huang, L. L. Cowie, J. P. Gardner, E. M. Hu, A. Songaila, and R. J. Wainscoat. The Hawaii K-Band Galaxy Survey. II. Bright K-Band Imaging. *ApJ*, 476:12, February 1997.
- [154] C.-P. Ma and J. N. Fry. Deriving the Nonlinear Cosmological Power Spectrum and Bispectrum from Analytic Dark Matter Halo Profiles and Mass Functions. *ApJ*, 543:503–513, November 2000.
- [155] A. Cooray and R. Sheth. Halo models of large scale structure. *Phys. Rep.*, 372:1–129, December 2002.

- [156] R. K. Sheth, H. J. Mo, and G. Tormen. Ellipsoidal collapse and an improved model for the number and spatial distribution of dark matter haloes. *MNRAS*, 323:1–12, May 2001.
- [157] D. J. Eisenstein and W. Hu. Baryonic Features in the Matter Transfer Function. *ApJ*, 496:605, March 1998.
- [158] J. F. Navarro, C. S. Frenk, and S. D. M. White. The Structure of Cold Dark Matter Halos. *ApJ*, 462:563, May 1996.
- [159] Z. Zheng, A. A. Berlind, D. H. Weinberg, A. J. Benson, C. M. Baugh, S. Cole, R. Davé, C. S. Frenk, N. Katz, and C. G. Lacey. Theoretical Models of the Halo Occupation Distribution: Separating Central and Satellite Galaxies. *ApJ*, 633:791–809, November 2005.
- [160] I. Zehavi, Z. Zheng, D. H. Weinberg, M. R. Blanton, N. A. Bahcall, A. A. Berlind, J. Brinkmann, J. A. Frieman, J. E. Gunn, R. H. Lupton, R. C. Nichol, W. J. Percival, D. P. Schneider, R. A. Skibba, M. A. Strauss, M. Tegmark, and D. G. York. Galaxy Clustering in the Completed SDSS Redshift Survey: The Dependence on Color and Luminosity. *ApJ*, 736:59, July 2011.
- [161] B. R. Granett, L. Guzzo, J. Coupon, S. Arnouts, P. Hudelot, O. Ilbert, H. J. McCracken, Y. Mellier, C. Adami, J. Bel, M. Bolzonella, D. Bottini, A. Cappi, O. Cucciati, S. de la Torre, P. Franzetti, A. Fritz, B. Garilli, A. Iovino, J. Krywult, V. Le Brun, O. Le Fevre, D. Maccagni, K. Malek, F. Marulli, B. Meneux, L. Paioro, M. Polletta, A. Pollo, M. Scodreggio, H. Schlegelhauser, L. Tasca, R. Tojeiro, D. Vergani, and A. Zanichelli. The power spectrum from the angular distribution of galaxies in the CFHTLS-Wide fields at redshift ~ 0.7 . *MNRAS*, 421:251–261, March 2012.
- [162] G. Lagache, N. Bavouzet, N. Fernandez-Conde, N. Ponthieu, T. Rodet, H. Dole, M.-A. Miville-Deschênes, and J.-L. Puget. Correlated Anisotropies in the Cosmic Far-Infrared Background Detected by the Multiband Imaging Photometer for Spitzer: Constraint on the Bias. *ApJ*, 665:L89–L92, August 2007.
- [163] M. P. Viero, P. A. R. Ade, J. J. Bock, E. L. Chapin, M. J. Devlin, M. Griffin, J. O. Gundersen, M. Halpern, P. C. Hargrave, D. H. Hughes, J. Klein, C. J. MacTavish, G. Marsden, P. G. Martin, P. Mauskopf, L. Moncelsi, M. Negrello, C. B. Netterfield, L. Olmi, E. Pascale, G. Patanchon, M. Rex, D. Scott, C. Semisch, N. Thomas, M. D. P. Truch, C. Tucker, G. S. Tucker, and D. V. Wiebe. BLAST: Correlations in the Cosmic Far-Infrared Background at 250, 350, and 500 μm Reveal Clustering of Star-forming Galaxies. *ApJ*, 707:1766–1778, December 2009.
- [164] R. E. Smith, J. A. Peacock, A. Jenkins, S. D. M. White, C. S. Frenk, F. R. Pearce, P. A. Thomas, G. Efstathiou, and H. M. P. Couchman. Stable clus-

- tering, the halo model and non-linear cosmological power spectra. *MNRAS*, 341:1311–1332, June 2003.
- [165] B. M. B. Henriques, S. D. M. White, G. Lemson, P. A. Thomas, Q. Guo, G.-D. Marleau, and R. A. Overzier. Confronting theoretical models with the observed evolution of the galaxy population out to $z=4$. *MNRAS*, page 2442, February 2012.
- [166] V. Springel, S. D. M. White, A. Jenkins, C. S. Frenk, N. Yoshida, L. Gao, J. Navarro, R. Thacker, D. Croton, J. Helly, J. A. Peacock, S. Cole, P. Thomas, H. Couchman, A. Evrard, J. Colberg, and F. Pearce. Simulations of the formation, evolution and clustering of galaxies and quasars. *Nature*, 435:629–636, June 2005.
- [167] M. Boylan-Kolchin, V. Springel, S. D. M. White, A. Jenkins, and G. Lemson. Resolving cosmic structure formation with the Millennium-II Simulation. *MNRAS*, 398:1150–1164, September 2009.
- [168] D. N. Spergel, L. Verde, H. V. Peiris, E. Komatsu, M. R.olta, C. L. Bennett, M. Halpern, G. Hinshaw, N. Jarosik, A. Kogut, M. Limon, S. S. Meyer, L. Page, G. S. Tucker, J. L. Weiland, E. Wollack, and E. L. Wright. First-Year Wilkinson Microwave Anisotropy Probe (WMAP) Observations: Determination of Cosmological Parameters. *ApJS*, 148:175–194, September 2003.
- [169] I. Sullivan, A. Cooray, R.-R. Chary, J. J. Bock, M. Brodwin, M. J. I. Brown, A. Dey, M. Dickinson, P. Eisenhardt, H. C. Ferguson, M. Giavalisco, B. Keating, A. Lange, B. Mobasher, W. T. Reach, D. Stern, and E. L. Wright. Clustering of the IR Background Light with Spitzer: Contribution from Resolved Sources. *ApJ*, 657:37–50, March 2007.
- [170] R.-R. Chary, A. Cooray, and I. Sullivan. Contribution to Unresolved Infrared Fluctuations from Dwarf Galaxies at Redshifts of 2-3. *ApJ*, 681:53–57, July 2008.
- [171] A. Kashlinsky. Cosmic Infrared Background from Population III Stars and Its Effect on Spectra of High- z Gamma-Ray Bursts. *ApJ*, 633:L5–L8, November 2005.
- [172] R. C. Gilmore. Constraining the near-infrared background light from Population III stars using high-redshift gamma-ray sources. *MNRAS*, 420:800–809, February 2012.
- [173] A. Kashlinsky and D. Band. Exploring First Stars Era with GLAST. In S. Ritz, P. Michelson, & C. A. Meegan, editor, *The First GLAST Symposium*, volume 921 of *American Institute of Physics Conference Series*, pages 243–245, July 2007.

- [174] R. C. Gilmore. Constraining the near-infrared background light from Population III stars using high-redshift gamma-ray sources. *MNRAS*, 420:800–809, February 2012.
- [175] C. C. Steidel, K. L. Adelberger, M. Giavalisco, M. Dickinson, and M. Pettini. Lyman-Break Galaxies at $z \gtrsim 4$ and the Evolution of the Ultraviolet Luminosity Density at High Redshift. *ApJ*, 519:1–17, July 1999.
- [176] M. Sullivan, M. A. Treyer, R. S. Ellis, T. J. Bridges, B. Milliard, and J. Donas. An ultraviolet-selected galaxy redshift survey - II. The physical nature of star formation in an enlarged sample. *MNRAS*, 312:442–464, February 2000.
- [177] M. Treyer, T. K. Wyder, D. Schiminovich, S. Arnouts, T. Budavári, B. Milliard, T. A. Barlow, L. Bianchi, Y.-I. Byun, J. Donas, K. Forster, P. G. Friedman, T. M. Heckman, P. N. Jelinsky, Y.-W. Lee, B. F. Madore, R. F. Malina, D. C. Martin, P. Morrissey, S. G. Neff, R. M. Rich, O. H. W. Siegmund, T. Small, A. S. Szalay, and B. Y. Welsh. The Ultraviolet Galaxy Luminosity Function from GALEX Data: Color-Dependent Evolution at Low Redshift. *ApJ*, 619:L19–L22, January 2005.
- [178] D. Schiminovich, O. Ilbert, S. Arnouts, B. Milliard, L. Tresse, O. Le Fèvre, M. Treyer, T. K. Wyder, T. Budavári, E. Zucca, G. Zamorani, D. C. Martin, C. Adami, M. Arnaboldi, S. Bardelli, T. Barlow, L. Bianchi, M. Bolzonella, D. Bottini, Y.-I. Byun, A. Cappi, T. Contini, S. Charlot, J. Donas, K. Forster, S. Foucaud, P. Franzetti, P. G. Friedman, B. Garilli, I. Gavignaud, L. Guzzo, T. M. Heckman, C. Hoopes, A. Iovino, P. Jelinsky, V. Le Brun, Y.-W. Lee, D. Maccagni, B. F. Madore, R. Malina, B. Marano, C. Marinoni, H. J. McCracken, A. Mazure, B. Meneux, P. Morrissey, S. Neff, S. Paltani, R. Pellò, J. P. Picat, A. Pollo, L. Pozzetti, M. Radovich, R. M. Rich, R. Scaramella, M. Scodreggio, M. Seibert, O. Siegmund, T. Small, A. S. Szalay, G. Vettolani, B. Welsh, C. K. Xu, and A. Zanichelli. The GALEX-VVDS Measurement of the Evolution of the Far-Ultraviolet Luminosity Density and the Cosmic Star Formation Rate. *ApJ*, 619:L47–L50, January 2005.
- [179] T. Budavári, A. S. Szalay, S. Charlot, M. Seibert, T. K. Wyder, S. Arnouts, T. A. Barlow, L. Bianchi, Y.-I. Byun, J. Donas, K. Forster, P. G. Friedman, T. M. Heckman, P. N. Jelinsky, Y.-W. Lee, B. F. Madore, R. F. Malina, D. C. Martin, B. Milliard, P. Morrissey, S. G. Neff, R. M. Rich, D. Schiminovich, O. H. W. Siegmund, T. Small, M. A. Treyer, and B. Welsh. The Ultraviolet Luminosity Function of GALEX Galaxies at Photometric Redshifts between 0.07 and 0.25. *ApJ*, 619:L31–L34, January 2005.
- [180] M. Sawicki and D. Thompson. Keck Deep Fields. III. Luminosity-dependent Evolution of the Ultraviolet Luminosity and Star Formation Rate Densities at $z \sim 4, 3$, and 2. *ApJ*, 648:299–309, September 2006.

- [181] S. L. Finkelstein, C. Papovich, B. Salmon, K. Finlator, M. Dickinson, H. C. Ferguson, M. Giavalisco, A. M. Koekemoer, N. A. Reddy, R. Bassett, C. J. Conselice, J. S. Dunlop, S. M. Faber, N. A. Grogin, N. P. Hathi, D. D. Kocevski, K. Lai, K.-S. Lee, R. J. McLure, B. Mobasher, and J. A. Newman. Candels: The Evolution of Galaxy Rest-frame Ultraviolet Colors from $z = 8$ to 4. *ApJ*, 756:164, September 2012.
- [182] D. L. Shupe, F. Fang, P. B. Hacking, and J. P. Huchra. The Local Luminosity Function at 25 Microns. *ApJ*, 501:597, July 1998.
- [183] C. Xu, P. B. Hacking, F. Fang, D. L. Shupe, C. J. Lonsdale, N. Y. Lu, G. Helou, G. J. Stacey, and M. L. N. Ashby. Emission Features and Source Counts of Galaxies in the Mid-Infrared. *ApJ*, 508:576–589, December 1998.
- [184] D. B. Sanders, J. M. Mazzarella, D.-C. Kim, J. A. Surace, and B. T. Soifer. The IRAS Revised Bright Galaxy Sample. *AJ*, 126:1607–1664, October 2003.
- [185] E. Le Floch, C. Papovich, H. Dole, E. F. Bell, G. Lagache, G. H. Rieke, E. Egami, P. G. Pérez-González, A. Alonso-Herrero, M. J. Rieke, M. Blaylock, C. W. Engelbracht, K. D. Gordon, D. C. Hines, K. A. Misselt, J. E. Morrison, and J. Mould. Infrared Luminosity Functions from the Chandra Deep Field-South: The Spitzer View on the History of Dusty Star Formation at $0 < z < 1$. *ApJ*, 632:169–190, October 2005.
- [186] P. G. Pérez-González, G. H. Rieke, E. Egami, A. Alonso-Herrero, H. Dole, C. Papovich, M. Blaylock, J. Jones, M. Rieke, J. Rigby, P. Barmby, G. G. Fazio, J. Huang, and C. Martin. Spitzer View on the Evolution of Star-forming Galaxies from $z = 0$ to $z \sim 3$. *ApJ*, 630:82–107, September 2005.
- [187] W. Rujopakarn, D. J. Eisenstein, G. H. Rieke, C. Papovich, R. J. Cool, J. Moustakas, B. T. Jannuzi, C. S. Kochanek, M. J. Rieke, A. Dey, P. Eisenhardt, S. S. Murray, M. J. I. Brown, and E. Le Floch. The Evolution of the Star Formation Rate of Galaxies at $0.0 \leq z \leq 1.2$. *ApJ*, 718:1171–1185, August 2010.
- [188] F. W. Stecker, M. A. Malkan, and S. T. Scully. A Determination of the Intergalactic Redshift Dependent UV-Optical-NIR Photon Density Using Deep Galaxy Survey Data and the Gamma-ray Opacity of the Universe. *ArXiv e-prints*, May 2012.
- [189] L. Tresse, O. Ilbert, E. Zucca, G. Zamorani, S. Bardelli, S. Arnouts, S. Paltani, L. Pozzetti, D. Bottini, B. Garilli, V. Le Brun, O. Le Fèvre, D. Maccagni, J.-P. Picat, R. Scaramella, M. Scodreggio, G. Vettolani, A. Zanichelli, C. Adami, M. Arnaboldi, M. Bolzonella, A. Cappi, S. Charlot, P. Ciliegi, T. Contini, S. Foucaud, P. Franzetti, I. Gavignaud, L. Guzzo, A. Iovino, H. J. McCracken, B. Marano, C. Marinoni, A. Mazure, B. Meneux, R. Merighi, R. Pellò, A. Pollo, M. Radovich, M. Bondi, A. Bongiorno, G. Busarello, O. Cucciati,

- F. Lamareille, G. Mathez, Y. Mellier, P. Merluzzi, and V. Ripepi. The cosmic star formation rate evolution from $z = 5$ to $z = 0$ from the VIMOS VLT deep survey. *A&A*, 472:403–419, September 2007.
- [190] J. P. Gardner, T. M. Brown, and H. C. Ferguson. Ultraviolet Galaxy Counts from Space Telescope Imaging Spectrograph Observations of the Hubble Deep Fields. *ApJ*, 542:L79–L82, October 2000.
- [191] C. K. Xu, J. Donas, S. Arnouts, T. K. Wyder, M. Seibert, J. Iglesias-Páramo, J. Blaizot, T. Small, B. Milliard, D. Schiminovich, D. C. Martin, T. A. Barlow, L. Bianchi, Y.-I. Byun, K. Forster, P. G. Friedman, T. M. Heckman, P. N. Jelinsky, Y.-W. Lee, B. F. Madore, R. F. Malina, P. Morrissey, S. G. Neff, R. M. Rich, O. H. W. Siegmund, A. S. Szalay, and B. Y. Welsh. Number Counts of GALEX Sources in Far-Ultraviolet (1530 Å) and Near-Ultraviolet (2310 Å) Bands. *ApJ*, 619:L11–L14, January 2005.
- [192] R. Hopwood, S. Serjeant, M. Negrello, C. Pearson, E. Egami, M. Im, J.-P. Kneib, J. Ko, H. M. Lee, M. G. Lee, H. Matsuhara, T. Nakagawa, I. Smail, and T. Takagi. Ultra Deep Akari Observations of Abell 2218: Resolving the 15 μm Extragalactic Background Light. *ApJ*, 716:L45–L50, June 2010.
- [193] L. Metcalfe, J.-P. Kneib, B. McBreen, B. Altieri, A. Biviano, M. Delaney, D. Elbaz, M. F. Kessler, K. Leech, K. Okumura, S. Ott, R. Perez-Martinez, C. Sanchez-Fernandez, and B. Schulz. An ISOCAM survey through gravitationally lensing galaxy clusters. I. Source lists and source counts for A370, A2218 and A2390. *A&A*, 407:791–822, September 2003.
- [194] C. Papovich, H. Dole, E. Egami, E. Le Floc’h, P. G. Pérez-González, A. Alonso-Herrero, L. Bai, C. A. Beichman, M. Blaylock, C. W. Engelbracht, K. D. Gordon, D. C. Hines, K. A. Misselt, J. E. Morrison, J. Mould, J. Muze-rolle, G. Neugebauer, P. L. Richards, G. H. Rieke, M. J. Rieke, J. R. Rigby, K. Y. L. Su, and E. T. Young. The 24 Micron Source Counts in Deep Spitzer Space Telescope Surveys. *ApJS*, 154:70–74, September 2004.
- [195] M. Béthermin, H. Dole, A. Beelen, and H. Aussel. Spitzer deep and wide legacy mid- and far-infrared number counts and lower limits of cosmic infrared background. *A&A*, 512:A78, March 2010.
- [196] R. Chary, S. Casertano, M. E. Dickinson, H. C. Ferguson, P. R. M. Eisenhardt, D. Elbaz, N. A. Grogin, L. A. Moustakas, W. T. Reach, and H. Yan. The Nature of Faint 24 Micron Sources Seen in Spitzer Space Telescope Observations of ELAIS-N1. *ApJS*, 154:80–86, September 2004.
- [197] R. S. Somerville, R. C. Gilmore, J. R. Primack, and A. Domínguez. Galaxy properties from the ultraviolet to the far-infrared: A cold dark matter models confront observations. *MNRAS*, 423:1992–2015, July 2012.

- [198] Abdo et al. Fermi Large Area Telescope Constraints on the Gamma-ray Opacity of the Universe. *ApJ*, 723:1082–1096, November 2010.
- [199] W. McConville, L. Ostorero, R. Moderski, Ł. Stawarz, C. C. Cheung, M. Ajello, A. Bouvier, J. Bregeon, D. Donato, J. Finke, A. Furniss, J. E. McEnery, M. E. Monzani, M. Orienti, L. C. Reyes, A. Rossetti, and D. A. Williams. Fermi Large Area Telescope Observations of the Active Galaxy 4C +55.17: Steady, Hard Gamma-Ray Emission and Its Implications. *ApJ*, 738:148, September 2011.
- [200] MAGIC Collaboration, J. Albert, E. Aliu, H. Anderhub, L. A. Antonelli, P. Antoranz, M. Backes, C. Baixeras, J. A. Barrio, H. Bartko, D. Bastieri, J. K. Becker, W. Bednarek, K. Berger, E. Bernardini, C. Bigongiari, A. Biland, R. K. Bock, G. Bonnoli, P. Bordas, V. Bosch-Ramon, T. Bretz, I. Britvitch, M. Camara, E. Carmona, A. Chilingarian, S. Commichau, J. L. Contreras, J. Cortina, M. T. Costado, S. Covino, V. Curtef, F. Dazzi, A. De Angelis, E. D. Cea del Pozo, R. de los Reyes, B. De Lotto, M. De Maria, F. De Sabata, C. D. Mendez, A. Dominguez, D. Dorner, M. Doro, M. Errando, M. Fagiolini, D. Ferenc, E. Fernández, R. Firpo, M. V. Fonseca, L. Font, N. Galante, R. J. García López, M. Garczarczyk, M. Gaug, F. Goebel, M. Hayashida, A. Herrero, D. Höhne, J. Hose, C. C. Hsu, S. Huber, T. Jogler, T. M. Kneiske, D. Kranich, A. La Barbera, A. Laille, E. Leonardo, E. Lindfors, S. Lombardi, F. Longo, M. López, E. Lorenz, P. Majumdar, G. Maneva, N. Mankuzhiyil, K. Mannheim, L. Maraschi, M. Mariotti, M. Martínez, D. Mazin, M. Meucci, M. Meyer, J. M. Miranda, R. Mirzoyan, S. Mizobuchi, M. Moles, A. Moralejo, D. Nieto, K. Nilsson, J. Ninkovic, N. Otte, I. Oya, M. Panniello, R. Paoletti, J. M. Paredes, M. Pasanen, D. Pascoli, F. Pauss, R. G. Pegna, M. A. Perez-Torres, M. Persic, L. Peruzzo, A. Piccioli, F. Prada, E. Prandini, N. Puchades, A. Raymers, W. Rhode, M. Ribó, J. Rico, M. Rissi, A. Robert, S. Rügamer, A. Saggion, T. Y. Saito, M. Salvati, M. Sanchez-Conde, P. Sartori, K. Satulecka, V. Scalzotto, V. Scapin, R. Schmitt, T. Schweizer, M. Shayduk, K. Shinozaki, S. N. Shore, N. Sidro, A. Sierpowska-Bartosik, A. Sillanpää, D. Sobczynska, F. Spanier, A. Stamerra, L. S. Stark, L. Takalo, F. Tavecchio, P. Temnikov, D. Tesaro, M. Teshima, M. Tluczykont, D. F. Torres, N. Turini, H. Vankov, A. Venturini, V. Vitale, R. M. Wagner, W. Wittek, V. Zabalza, F. Zandanel, R. Zanin, and J. Zapatero. Very-High-Energy gamma rays from a Distant Quasar: How Transparent Is the Universe? *Science*, 320:1752–, June 2008.
- [201] J. Aleksić, L. A. Antonelli, P. Antoranz, M. Backes, J. A. Barrio, D. Bastieri, J. Becerra González, W. Bednarek, A. Berdyugin, K. Berger, E. Bernardini, A. Biland, O. Blanch, R. K. Bock, A. Boller, G. Bonnoli, D. Borla Tridon, I. Braun, T. Bretz, A. Cañellas, E. Carmona, A. Carosi, P. Colin, E. Colombo, J. L. Contreras, J. Cortina, L. Cossio, S. Covino, F. Dazzi, A. de Angelis, E. de Cea Del Pozo, B. de Lotto, C. Delgado Mendez, A. Diago Ortega, M. Doert, A. Domínguez, D. Dominis Prester, D. Dorner, M. Doro, D. Elsaesser,

D. Ferenc, M. V. Fonseca, L. Font, C. Fruck, R. J. García López, M. Garzarczyk, D. Garrido, G. Giavitto, N. Godinović, D. Hadasch, D. Häfner, A. Herrero, D. Hildebrand, J. Hose, D. Hrupec, B. Huber, T. Jogler, S. Klepser, T. Krähenbühl, J. Krause, A. La Barbera, D. Lelas, E. Leonardo, E. Lindfors, S. Lombardi, M. López, E. Lorenz, P. Majumdar, M. Makariev, G. Maneva, N. Mankuzhiyil, K. Mannheim, L. Maraschi, M. Mariotti, M. Martínez, D. Mazin, M. Meucci, J. M. Miranda, R. Mirzoyan, H. Miyamoto, J. Moldón, A. Moralejo, D. Nieto, K. Nilsson, R. Orito, I. Oya, R. Paoletti, S. Pardo, J. M. Paredes, S. Partini, M. Pasanen, F. Pauss, M. A. Perez-Torres, M. Persic, L. Peruzzo, M. Pilia, J. Pochon, F. Prada, P. G. Prada Moroni, E. Prandini, I. Puljak, I. Reichardt, R. Reinthal, W. Rhode, M. Ribó, J. Rico, S. Rügamer, M. Rüger, A. Saggion, K. Saito, T. Y. Saito, M. Salvati, K. Satalecka, V. Scalzotto, V. Scapin, C. Schultz, T. Schweizer, M. Shayduk, S. N. Shore, A. Sillanpää, J. Sitarek, D. Sobczynska, F. Spanier, S. Spiro, A. Stamerra, B. Steinke, J. Storz, N. Strah, T. Surić, L. Takalo, F. Tavecchio, P. Temnikov, T. Terzić, D. Tescaro, M. Teshima, M. Thom, O. Tibolla, D. F. Torres, A. Treves, H. Vankov, P. Vogler, R. M. Wagner, Q. Weitzel, V. Zabalza, F. Zandanel, and R. Zanin. MAGIC Observations and multiwavelength properties of the quasar 3C 279 in 2007 and 2009. *A&A*, 530:A4, June 2011.

- [202] M. Ackermann, M. Ajello, A. Allafort, W. B. Atwood, L. Baldini, J. Ballet, G. Barbiellini, D. Bastieri, K. Bechtol, A. Belfiore, R. Bellazzini, E. Bernieri, E. Bissaldi, E. D. Bloom, E. Bonamente, T. J. Brandt, J. Bregeon, M. Brigida, P. Bruel, R. Buehler, T. H. Burnett, S. Buson, G. A. Caliandro, R. A. Cameron, R. Campana, P. A. Caraveo, J. M. Casandjian, E. Cavazzuti, C. Cecchi, E. Charles, R. C. G. Chaves, A. Chekhtman, C. C. Cheung, J. Chiang, G. Chiaro, S. Ciprini, R. Claus, J. Cohen-Tanugi, L. R. Cominsky, J. Conrad, S. Cutini, F. D’Ammando, A. de Angelis, F. de Palma, C. D. Dermer, R. Desiante, S. W. Digel, L. Di Venere, P. S. Drell, A. Drlica-Wagner, C. Favuzzi, S. J. Fegan, E. C. Ferrara, W. B. Focke, P. Fortin, A. Franckowiak, S. Funk, P. Fusco, F. Gargano, D. Gasparrini, N. Gehrels, S. Germani, N. Giglietto, P. Giommi, F. Giordano, M. Giroletti, G. Godfrey, G. A. Gomez-Vargas, I. A. Grenier, S. Guiriec, D. Hadasch, Y. Hanabata, A. K. Harding, M. Hayashida, E. Hays, J. Hewitt, A. B. Hill, D. Horan, R. E. Hughes, T. Jogler, G. Jóhannesson, A. S. Johnson, T. J. Johnson, W. N. Johnson, T. Kamae, J. Kataoka, T. Kawano, J. Knödseder, M. Kuss, J. Lande, S. Larsson, L. Latronico, M. Lemoine-Goumard, F. Longo, F. Loparco, B. Lott, M. N. Lovellette, P. Lubrano, E. Massaro, M. Mayer, M. N. Mazziotta, J. E. McEnery, J. Mehault, P. F. Michelson, T. Mizuno, A. A. Moiseev, M. E. Monzani, A. Morselli, I. V. Moskalenko, S. Murgia, R. Nemmen, E. Nuss, T. Ohsugi, A. Okumura, M. Orienti, J. F. Ormes, D. Paneque, J. S. Perkins, M. Pesce-Rollins, F. Piron, G. Pivato, T. A. Porter, S. Rainò, M. Razzano, A. Reimer, O. Reimer, T. Reposeur, S. Ritz, R. W. Romani, M. Roth, P. M. Saz Parkinson, A. Schulz, C. Sgrò, E. J. Siskind, D. A. Smith, G. Spandre, P. Spinelli, Ł. Stawarz, A. W. Strong, D. J. Suson, H. Takahashi, J. G.

- Thayer, J. B. Thayer, D. J. Thompson, L. Tibaldo, M. Tinivella, D. F. Torres, G. Tosti, E. Troja, Y. Uchiyama, T. L. Usher, J. Vandenbroucke, V. Vasileiou, G. Vianello, V. Vitale, M. Werner, B. L. Winer, K. S. Wood, and M. Wood. The First Fermi-LAT Catalog of Sources above 10 GeV. *ApJS*, 209:34, December 2013.
- [203] R. C. Hickox and M. Markevitch. Absolute Measurement of the Unresolved Cosmic X-Ray Background in the 0.5-8 keV Band with Chandra. *ApJ*, 645:95–114, July 2006.
- [204] B. D. Lehmer, Y. Q. Xue, W. N. Brandt, D. M. Alexander, F. E. Bauer, M. Brusa, A. Comastri, R. Gilli, A. E. Hornschemeier, B. Luo, M. Paolillo, A. Ptak, O. Shemmer, D. P. Schneider, P. Tozzi, and C. Vignali. The 4 Ms Chandra Deep Field-South Number Counts Apportioned by Source Class: Pervasive Active Galactic Nuclei and the Ascent of Normal Galaxies. *ApJ*, 752:46, June 2012.
- [205] P. Ranalli, A. Comastri, and G. Setti. The 2-10 keV luminosity as a Star Formation Rate indicator. *A&A*, 399:39–50, February 2003.
- [206] M. Persic and Y. Rephaeli. Galactic star formation rates gauged by stellar end-products. *A&A*, 463:481–492, February 2007.
- [207] B. D. Lehmer, D. M. Alexander, F. E. Bauer, W. N. Brandt, A. D. Goulding, L. P. Jenkins, A. Ptak, and T. P. Roberts. A Chandra Perspective on Galaxy-wide X-ray Binary Emission and its Correlation with Star Formation Rate and Stellar Mass: New Results from Luminous Infrared Galaxies. *ApJ*, 724:559–571, November 2010.
- [208] L. L. Cowie, A. J. Barger, and G. Hasinger. The Faintest X-Ray Sources from $z = 0$ TO 8. *ApJ*, 748:50, March 2012.
- [209] A. R. Basu-Zych, B. D. Lehmer, A. E. Hornschemeier, R. J. Bouwens, T. Fragos, P. A. Oesch, K. Belczynski, W. N. Brandt, V. Kalogera, B. Luo, N. Miller, J. R. Mullaney, P. Tzanavaris, Y. Xue, and A. Zezas. The X-Ray Star Formation Story as Told by Lyman Break Galaxies in the 4 Ms CDF-S. *ApJ*, 762:45, January 2013.
- [210] N. Cappelluti, P. Ranalli, M. Roncarelli, P. Arevalo, G. Zamorani, A. Comastri, R. Gilli, E. Rovilos, C. Vignali, V. Allevato, A. Finoguenov, T. Miyaji, F. Nicastro, I. Georgantopoulos, and A. Kashlinsky. The nature of the unresolved extragalactic cosmic soft X-ray background. *MNRAS*, 427:651–663, November 2012.
- [211] E. Treister, C. M. Urry, J. Van Duyne, M. Dickinson, R.-R. Chary, D. M. Alexander, F. Bauer, P. Natarajan, P. Lira, and N. A. Grogin. Spitzer Number Counts of Active Galactic Nuclei in the GOODS Fields. *ApJ*, 640:603–611, April 2006.

- [212] R. J. Assef, C. S. Kochanek, M. L. N. Ashby, M. Brodwin, M. J. I. Brown, R. Cool, W. Forman, A. H. Gonzalez, R. C. Hickox, B. T. Jannuzi, C. Jones, E. Le Floch, J. Moustakas, S. S. Murray, and D. Stern. The Mid-IR- and X-ray-Selected QSO Luminosity Function. *ApJ*, 728:56, February 2011.
- [213] R. J. Assef, C. S. Kochanek, M. Brodwin, R. Cool, W. Forman, A. H. Gonzalez, R. C. Hickox, C. Jones, E. Le Floch, J. Moustakas, S. S. Murray, and D. Stern. Low-Resolution Spectral Templates for Active Galactic Nuclei and Galaxies from 0.03 to 30 μm . *ApJ*, 713:970–985, April 2010.
- [214] G. T. Richards, M. Lacy, L. J. Storrie-Lombardi, P. B. Hall, S. C. Gallagher, D. C. Hines, X. Fan, C. Papovich, D. E. Vanden Berk, G. B. Trammell, D. P. Schneider, M. Vestergaard, D. G. York, S. Jester, S. F. Anderson, T. Budavári, and A. S. Szalay. Spectral Energy Distributions and Multiwavelength Selection of Type 1 Quasars. *ApJS*, 166:470–497, October 2006.
- [215] S. M. Croom, G. T. Richards, T. Shanks, B. J. Boyle, M. A. Strauss, A. D. Myers, R. C. Nichol, K. A. Pimbblet, N. P. Ross, D. P. Schneider, R. G. Sharp, and D. A. Wake. The 2dF-SDSS LRG and QSO survey: the QSO luminosity function at $0.4 < z < 2.6$. *MNRAS*, 399:1755–1772, November 2009.
- [216] E. Glikman, S. G. Djorgovski, D. Stern, A. Dey, B. T. Jannuzi, and K.-S. Lee. The Faint End of the Quasar Luminosity Function at $z \sim 4$: Implications for Ionization of the Intergalactic Medium and Cosmic Downsizing. *ApJ*, 728:L26, February 2011.
- [217] P. F. Hopkins, G. T. Richards, and L. Hernquist. An Observational Determination of the Bolometric Quasar Luminosity Function. *ApJ*, 654:731–753, January 2007.
- [218] F. Civano, M. Elvis, M. Brusa, A. Comastri, M. Salvato, G. Zamorani, T. Aldcroft, A. Bongiorno, P. Capak, N. Cappelluti, M. Cisternas, F. Fiore, A. Fruscione, H. Hao, J. Kartaltepe, A. Koekemoer, R. Gilli, C. D. Impey, G. Lanzuisi, E. Lusso, V. Mainieri, T. Miyaji, S. Lilly, D. Masters, S. Puccetti, K. Schawinski, N. Z. Scoville, J. Silverman, J. Trump, M. Urry, C. Vignali, and N. J. Wright. The Chandra COSMOS Survey. III. Optical and Infrared Identification of X-Ray Point Sources. *ApJS*, 201:30, August 2012.
- [219] A. J. Barger, L. L. Cowie, R. F. Mushotzky, Y. Yang, W.-H. Wang, A. T. Steffen, and P. Capak. The Cosmic Evolution of Hard X-Ray-selected Active Galactic Nuclei. *AJ*, 129:578–609, February 2005.
- [220] C. Leitherer, D. Schaerer, J. D. Goldader, R. M. González Delgado, C. Robert, D. F. Kune, D. F. de Mello, D. Devost, and T. M. Heckman. Starburst99: Synthesis Models for Galaxies with Active Star Formation. *ApJS*, 123:3–40, July 1999.

- [221] Y. Q. Xue, B. Luo, W. N. Brandt, F. E. Bauer, B. D. Lehmer, P. S. Broos, D. P. Schneider, D. M. Alexander, M. Brusa, A. Comastri, A. C. Fabian, R. Gilli, G. Hasinger, A. E. Hornschemeier, A. Koekemoer, T. Liu, V. Mainieri, M. Paolillo, D. A. Rafferty, P. Rosati, O. Shemmer, J. D. Silverman, I. Smail, P. Tozzi, and C. Vignali. The Chandra Deep Field-South Survey: 4 Ms Source Catalogs. *ApJS*, 195:10, July 2011.
- [222] C. Norman, A. Ptak, A. Hornschemeier, G. Hasinger, J. Bergeron, A. Comastri, R. Giacconi, R. Gilli, K. Glazebrook, T. Heckman, L. Kewley, P. Ranalli, P. Rosati, G. Szokoly, P. Tozzi, J. Wang, W. Zheng, and A. Zirm. The X-Ray-derived Cosmological Star Formation History and the Galaxy X-Ray Luminosity Functions in the Chandra Deep Fields North and South. *ApJ*, 607:721–738, June 2004.
- [223] P. Tzanavaris and I. Georgantopoulos. The galaxy luminosity function and its evolution with Chandra. *A&A*, 480:663–670, March 2008.
- [224] Y. Avni and H. Tananbaum. X-ray properties of optically selected QSOs. *ApJ*, 305:83–99, June 1986.
- [225] B. Boroson, D.-W. Kim, and G. Fabbiano. Revisiting with Chandra the Scaling Relations of the X-ray Emission Components (Binaries, Nuclei, and Hot Gas) of Early-type Galaxies. *ApJ*, 729:12, March 2011.
- [226] B. Magnelli, D. Elbaz, R. R. Chary, M. Dickinson, D. Le Borgne, D. T. Frayer, and C. N. A. Willmer. The $0.4 < z < 1.3$ star formation history of the Universe as viewed in the far-infrared. *A&A*, 496:57–75, March 2009.
- [227] T. T. Takeuchi, K. Yoshikawa, and T. T. Ishii. The Luminosity Function of IRAS Point Source Catalog Redshift Survey Galaxies. *ApJ*, 587:L89–L92, April 2003.
- [228] G. Rodighiero, M. Vaccari, A. Franceschini, L. Tresse, O. Le Fevre, V. Le Brun, C. Mancini, I. Matute, A. Cimatti, L. Marchetti, O. Ilbert, S. Arnouts, M. Bolzonella, E. Zucca, S. Bardelli, C. J. Lonsdale, D. Shupe, J. Surace, M. Rowan-Robinson, B. Garilli, G. Zamorani, L. Pozzetti, M. Bondi, S. de la Torre, D. Vergani, P. Santini, A. Grazian, and A. Fontana. Mid- and far-infrared luminosity functions and galaxy evolution from multiwavelength Spitzer observations up to $z \sim 2.5$. *A&A*, 515:A8, June 2010.
- [229] M. E. Anderson, J. N. Bregman, and X. Dai. Extended Hot Halos around Isolated Galaxies Observed in the ROSAT All-Sky Survey. *ApJ*, 762:106, January 2013.
- [230] A. D. Goulding, W. R. Forman, R. C. Hickox, C. Jones, R. Kraft, S. S. Murray, A. Vikhlinin, A. L. Coil, M. C. Cooper, M. Davis, and J. A. Newman. The Chandra X-Ray Point-source Catalog in the DEEP2 Galaxy Redshift Survey Fields. *ApJS*, 202:6, September 2012.

- [231] R. Gilli, A. Comastri, and G. Hasinger. The synthesis of the cosmic X-ray background in the Chandra and XMM-Newton era. *A&A*, 463:79–96, February 2007.
- [232] G. Hasinger, T. Miyaji, and M. Schmidt. Luminosity-dependent evolution of soft X-ray selected AGN. New Chandra and XMM-Newton surveys. *A&A*, 441:417–434, October 2005.
- [233] A. Finoguenov, L. Guzzo, G. Hasinger, N. Z. Scoville, H. Aussel, H. Böhringer, M. Brusa, P. Capak, N. Cappelluti, A. Comastri, S. Giodini, R. E. Griffiths, C. Impey, A. M. Koekemoer, J.-P. Kneib, A. Leauthaud, O. Le Fèvre, S. Lilly, V. Mainieri, R. Massey, H. J. McCracken, B. Mobasher, T. Murayama, J. A. Peacock, I. Sakelliou, E. Schinnerer, J. D. Silverman, V. Smolčić, Y. Taniguchi, L. Tasca, J. E. Taylor, J. R. Trump, and G. Zamorani. The XMM-Newton Wide-Field Survey in the COSMOS Field: Statistical Properties of Clusters of Galaxies. *ApJS*, 172:182–195, September 2007.
- [234] M. Roncarelli, N. Cappelluti, S. Borgani, E. Branchini, and L. Moscardini. The effect of feedback on the emission properties of the warm-hot intergalactic medium. *MNRAS*, 424:1012–1025, August 2012.
- [235] L. Tornatore, S. Borgani, M. Viel, and V. Springel. The impact of feedback on the low-redshift intergalactic medium. *MNRAS*, 402:1911–1926, March 2010.
- [236] G. Erfanianfar, A. Finoguenov, M. Tanaka, M. Lerchster, K. Nandra, E. Laird, J. L. Connelly, R. Bielby, M. Mirkazemi, S. M. Faber, D. Kocevski, M. Cooper, J. A. Newman, T. Jeltema, A. L. Coil, F. Brimiouille, M. Davis, H. J. McCracken, C. Willmer, B. Gerke, N. Cappelluti, and S. Gwyn. X-Ray Groups of Galaxies in the AEGIS Deep and Wide Fields. *ApJ*, 765:117, March 2013.
- [237] T. Miyaji, M. Krumpke, A. L. Coil, and H. Aceves. The Spatial Clustering of ROSAT All-sky Survey AGNs. II. Halo Occupation Distribution Modeling of the Cross-correlation Function. *ApJ*, 726:83, January 2011.
- [238] V. Allevato, A. Finoguenov, G. Hasinger, T. Miyaji, N. Cappelluti, M. Salvato, G. Zamorani, R. Gilli, M. R. George, M. Tanaka, M. Brusa, J. Silverman, F. Civano, M. Elvis, and F. Shankar. Occupation of X-Ray-selected Galaxy Groups by X-Ray Active Galactic Nuclei. *ApJ*, 758:47, October 2012.
- [239] J. Richardson, S. Chatterjee, Z. Zheng, A. D. Myers, and R. Hickox. The Halo Occupation Distribution of X-Ray-bright Active Galactic Nuclei: A Comparison with Luminous Quasars. *ApJ*, 774:143, September 2013.
- [240] Y. Shen, C. K. McBride, M. White, Z. Zheng, A. D. Myers, H. Guo, J. A. Kirkpatrick, N. Padmanabhan, J. K. Parejko, N. P. Ross, D. J. Schlegel, D. P. Schneider, A. Streblyanska, M. E. C. Swanson, I. Zehavi, K. Pan, D. Bizyaev, H. Brewington, G. Ebelke, V. Malanushenko, E. Malanushenko, D. Oravetz, A. Simmons, and S. Snedden. Cross-correlation of SDSS DR7 Quasars and

- DR10 BOSS Galaxies: The Weak Luminosity Dependence of Quasar Clustering at $z \sim 0.5$. *ApJ*, 778:98, December 2013.
- [241] J. Richardson, Z. Zheng, S. Chatterjee, D. Nagai, and Y. Shen. The Halo Occupation Distribution of SDSS Quasars. *ApJ*, 755:30, August 2012.
- [242] N. Cappelluti, V. Allevato, and A. Finoguenov. Clustering of X-Ray-Selected AGN. *Advances in Astronomy*, 2012, 2012.
- [243] S. Chatterjee, C. Degraf, J. Richardson, Z. Zheng, D. Nagai, and T. Di Matteo. The halo occupation distribution of active galactic nuclei. *MNRAS*, 419:2657–2669, January 2012.
- [244] A. Cooray. Halo model at its best: constraints on conditional luminosity functions from measured galaxy statistics. *MNRAS*, 365:842–866, January 2006.
- [245] M. Béthermin, L. Wang, O. Doré, G. Lagache, M. Sargent, E. Daddi, M. Cousin, and H. Aussel. The redshift evolution of the distribution of star formation among dark matter halos as seen in the infrared. *A&A*, 557:A66, September 2013.
- [246] K. Helgason and A. Kashlinsky. Reconstructing the γ -Ray Photon Optical Depth of the Universe to $z \sim 4$ from Multiwavelength Galaxy Survey Data. *ApJ*, 758:L13, October 2012.
- [247] J. E. Grove and on behalf of the Fermi LAT Collaboration. Pass 8: Transforming the Scientific Performance of the Fermi Large Area Telescope. In *American Astronomical Society Meeting Abstracts*, volume 223 of *American Astronomical Society Meeting Abstracts*, page 256.03, January 2014.
- [248] M. R. Blanton, J. Brinkmann, I. Csabai, M. Doi, D. Eisenstein, M. Fukugita, J. E. Gunn, D. W. Hogg, and D. J. Schlegel. Estimating Fixed-Frame Galaxy Magnitudes in the Sloan Digital Sky Survey. *AJ*, 125:2348–2360, May 2003.
- [249] M. S. Bessell. Standard Photometric Systems. *ARA&A*, 43:293–336, September 2005.
- [250] M. R. Blanton, J. Dalcanton, D. Eisenstein, J. Loveday, M. A. Strauss, M. SubbaRao, D. H. Weinberg, J. E. Anderson, Jr., J. Annis, N. A. Bahcall, M. Bernardi, J. Brinkmann, R. J. Brunner, S. Burles, L. Carey, F. J. Castander, A. J. Connolly, I. Csabai, M. Doi, D. Finkbeiner, S. Friedman, J. A. Frieman, M. Fukugita, J. E. Gunn, G. S. Hennessy, R. B. Hindsley, D. W. Hogg, T. Ichikawa, Ž. Ivezić, S. Kent, G. R. Knapp, D. Q. Lamb, R. F. Leger, D. C. Long, R. H. Lupton, T. A. McKay, A. Meiksin, A. Merelli, J. A. Munn, V. Narayanan, M. Newcomb, R. C. Nichol, S. Okamura, R. Owen, J. R. Pier, A. Pope, M. Postman, T. Quinn, C. M. Rockosi, D. J. Schlegel, D. P. Schneider, K. Shimasaku, W. A. Siegmund, S. Smee, Y. Snir, C. Stoughton,

- C. Stubbs, A. S. Szalay, G. P. Szokoly, A. R. Thakar, C. Tremonti, D. L. Tucker, A. Uomoto, D. Vanden Berk, M. S. Vogeley, P. Waddell, B. Yanny, N. Yasuda, and D. G. York. The Luminosity Function of Galaxies in SDSS Commissioning Data. *AJ*, 121:2358–2380, May 2001.
- [251] M. A. Strauss, D. H. Weinberg, R. H. Lupton, V. K. Narayanan, J. Annis, M. Bernardi, M. Blanton, S. Burles, A. J. Connolly, J. Dalcanton, M. Doi, D. Eisenstein, J. A. Frieman, M. Fukugita, J. E. Gunn, Ž. Ivezić, S. Kent, R. S. J. Kim, G. R. Knapp, R. G. Kron, J. A. Munn, H. J. Newberg, R. C. Nichol, S. Okamura, T. R. Quinn, M. W. Richmond, D. J. Schlegel, K. Shimasaku, M. SubbaRao, A. S. Szalay, D. Vanden Berk, M. S. Vogeley, B. Yanny, N. Yasuda, D. G. York, and I. Zehavi. Spectroscopic Target Selection in the Sloan Digital Sky Survey: The Main Galaxy Sample. *AJ*, 124:1810–1824, September 2002.
- [252] S. Andreon. Dim galaxies and outer halos of galaxies missed by 2MASS? The near-infrared luminosity function and density. *A&A*, 382:495–502, February 2002.
- [253] D. T. Hill, L. S. Kelvin, S. P. Driver, A. S. G. Robotham, E. Cameron, N. Cross, E. Andrae, I. K. Baldry, S. P. Bamford, J. Bland-Hawthorn, S. Brough, C. J. Conselice, S. Dye, A. M. Hopkins, J. Liske, J. Loveday, P. Norberg, J. A. Peacock, S. M. Croom, C. S. Frenk, A. W. Graham, D. H. Jones, K. Kuijken, B. F. Madore, R. C. Nichol, H. R. Parkinson, S. Phillipps, K. A. Pimblet, C. C. Popescu, M. Prescott, M. Seibert, R. G. Sharp, W. J. Sutherland, D. Thomas, R. J. Tuffs, and E. van Kampen. Galaxy and Mass Assembly: FUV, NUV, ugrizYJHK Petrosian, Kron and Sérsic photometry. *MNRAS*, 412:765–799, April 2011.
- [254] M. Schmidt. Space Distribution and Luminosity Functions of Quasi-Stellar Radio Sources. *ApJ*, 151:393, February 1968.
- [255] A. Sandage, G. A. Tammann, and A. Yahil. The velocity field of bright nearby galaxies. I - The variation of mean absolute magnitude with redshift for galaxies in a magnitude-limited sample. *ApJ*, 232:352–364, September 1979.
- [256] G. Efstathiou, R. S. Ellis, and B. A. Peterson. Analysis of a complete galaxy redshift survey. II - The field-galaxy luminosity function. *MNRAS*, 232:431–461, May 1988.
- [257] C. N. A. Willmer. Estimating galaxy luminosity functions. *AJ*, 114:898–912, September 1997.